University

Università degli studi di Napoli
Federico II

Doctoral Thesis

Hybrid superconducting InAs-nanowire based nanojunctions

by

Domenico Montemurro

Supervisors:

Prof. Arturo Tagliacozzo

Prof. Francesco Tafuri

31st March, 2016

Declaration of Authorship

I Domenico Montemurro, declare that this thesis titled, 'Superconductive Hybrid nano-Systems' and the work presented in it are my own. I confirm that:

- This work was done wholly or mainly while in candidature for a research degree at this University.
- Where any part of this thesis has previously been submitted for a degree or any other qualification at this University or any other institution, this has been clearly stated.
- Where I have consulted the published work of others, this is always clearly attributed.
- Where I have quoted from the work of others, the source is always given. With the exception of such quotations, this thesis is entirely my own work.
- I have acknowledged all main sources of help.
- Where the thesis is based on work done by myself jointly with others, I have made clear exactly what was done by others and what I have contributed myself.

Signed: _____

Date: _____

List of Pubblications

This thesis is based on the work contained in the following papers:

I:
Suspended InAs nanowire Josephson junctions assembled via dielectrophoresis
Domenico Montemurro, Daniela Stornaiuolo, Davide Massarotti, Daniele Ercolani, Lucia Sorba, Fabio Beltram, Francesco Tafuri and Stefano Roddaro;
Nanotechnology 26 (2015) 385302; http://www.ncbi.nlm.nih.gov/pubmed/26335273

II:
Towards a Hybrid High Critical Temperature Superconductor Junction With a Semiconducting InAs Nanowire Barrier
Domenico Montemurro, Davide Massarotti, Procolo Lucignano, Stefano Roddaro, Daniela Stornaiuolo, Daniele Ercolani, Lucia Sorba, Arturo Tagliacozzo, Fabio Beltram, Francesco Tafuri;
J Supercond Nov Magn (2015) 28:3429-3437; http://link.springer.com/article/10.1007/s10948-015-3174-7#/page-1

III:
Recent Achievements on the Physics of High-TC Superconductor Josephson Junctions: Background, Perspectives and Inspiration
Francesco Tafuri, Davide Massarotti, Luca Galletti, Daniela Stornaiuolo, Domenico Montemurro, Luigi Longobardi, Procolo Lucignano, Giacomo Rotoli, Giovanni Piero Pepe, Arturo Tagliacozzo, Floriana Lombardi

J Supercond Nov Magn (2013) 26:21-4; http://link.springer.com/article/10.1007/s10948-012-1773-0#/page-1

IV:

Escape dynamics in moderately damped Josephson junctions
Davide Massarottii, Luigi Longobardi, Luca Galletti, Daniela Stornaiuolo, Domenico Montemurro, Giampiero Pepe, Giacomo Rotoli, Antonio Barone, and Francesco Tafuri;
Low Temperature Physics 38, 263 (2012); http://scitation.aip.org/content/aip/journal/ltp/38/4/10.1063/1.3699625

V:

Energy scales in YBaCuO grain boundary biepitaxial Josephson junctions
Francesco Tafuri, Daniela Stornaiuolo, Procolo Lucignano, Luca Galletti, Luigi Longobardi, Davide Massarotti, Domenico Montemurro, Gianpaolo Papari, Antonio Barone and Arturo Tagliacozzo;
Physica C 479 (2012) 74-78 ; http://www.sciencedirect.com/science/article/pii/S0921453411005454

VI:

Coherent transport in extremely underdoped Nd1.2Ba1.8Cu3Oz nanostructures
Franco Carillo, G M De Luca, Domenico Montemurro, Gianpaolo Papari, Marco Salluzzo, Daniela Stornaiuolo, Francesco Tafuri and Fabio Beltram;
New Journal of Physics 14 (2012) 083025; http://iopscience.iop.org/article/10.1088/1367-2630/14/8/083025/meta;jsessionid=ADBFD3F60ACB23E47FD4625EF
ip-10-40-2-75

Physical Constants

Name	Symbol	Value	Unit
Number π	π	**3.14159265358979323846**	
Number e	**e**	**2.71828182845904523536**	
Euler's constant	$\gamma = \lim_{n\to\infty}\left(\sum_{k=1}^{n} 1/k - \ln(n)\right) = 0.5772156649$		
Elementary charge	e	$1.60217733 \cdot 10^{-19}$	**C**
Gravitational constant	G, κ	$6.67259 \cdot 10^{-11}$	$\mathbf{m^3kg^{-1}s^{-2}}$
Fine-structure constant	$\alpha = e^2/2hc\varepsilon_0$	$\approx 1/137$	
Speed of light in vacuum	c	$2.99792458 \cdot 10^{8}$	**m/s (def)**
Permittivity of the vacuum	ε_0	$8.854187 \cdot 10^{-12}$	**F/m**
Permeability of the vacuum	μ_0	$4\pi \cdot 10^{-7}$	**H/m**
$(4\pi\varepsilon_0)^{-1}$		$8.9876 \cdot 10^{9}$	$\mathbf{Nm^2C^{-2}}$
Planck's constant	h	$6.6260755 \cdot 10^{-34}$	**Js**
Dirac's constant	$\hbar = h/2\pi$	$1.0545727 \cdot 10^{-34}$	**Js**
Bohr magneton	$\mu_\mathrm{B} = e\hbar/2m_\mathrm{e}$	$9.2741 \cdot 10^{-24}$	$\mathbf{Am^2}$
Bohr radius	a_0	0.52918	**Å**
Rydberg's constant	Ry	**13.595**	**eV**
Electron Compton wavelength	$\lambda_\mathrm{Ce} = h/m_\mathrm{e}c$	$2.2463 \cdot 10^{-12}$	**m**
Proton Compton wavelength	$\lambda_\mathrm{Cp} = h/m_\mathrm{p}c$	$1.3214 \cdot 10^{-15}$	**m**
Reduced mass of the H-atom	μ_H	$9.1045755 \cdot 10^{-31}$	**kg**
Stefan-Boltzmann's constant	σ	$5.67032 \cdot 10^{-8}$	$\mathbf{Wm^{-2}K^{-4}}$
Wien's constant	k_W	$2.8978 \cdot 10^{-3}$	**mK**
Molar gasconstant	R	**8.31441**	$\mathbf{J{\cdot}mol^{-1}{\cdot}K^{-1}}$
Avogadro's constant	N_A	$6.0221367 \cdot 10^{23}$	$\mathbf{mol^{-1}}$
Boltzmann's constant	$k = R/N_\mathrm{A}$	$1.380658 \cdot 10^{-23}$	**J/K**
Electron mass	m_e	$9.1093897 \cdot 10^{-31}$	**kg**
Proton mass	m_p	$1.6726231 \cdot 10^{-27}$	**kg**
Neutron mass	m_n	$1.674954 \cdot 10^{-27}$	**kg**
Elementary mass unit	$m_\mathrm{u} = \frac{1}{12}m(^{12}_{6}\mathbf{C})$	$1.6605656 \cdot 10^{-27}$	**kg**
Nuclear magneton	μ_N	$5.0508 \cdot 10^{-27}$	**J/T**

Contents

List of Figures

List of Tables

Introduction

Semiconductor-superconductor hybrid devices have been investigated for many years[14–18]. In these devices the macroscopic quantum correlations typical of superconductors can be induced via proximity effect in a wide class of low-dimensional materials such as, topological insulator [19], ferromagnetic barriers [20], graphene [21, 22] and in particular semiconducting nanowires (NWs) [14, 17, 18, 23–26] which offer a unique freedom in the design and control of quantum states. Precise control of the geometry [27], composition and chemical properties [28–31] enabled the NWs to be a potential building block in fields, like nanoelectronics, photonics, mechanical and biological systems or sensors [32]. The most intriguing consequence of such a material combination is the possibility to give raise to novel excitations and properties that none of the single device components originally possesses. Recently, intense activity was aimed at artificially creating topologically protected Majorana fermion states [33–36]. Many proposals make use quasi-one-dimensional (quasi-1D) low critical temperature superconductors (LTS) in contact with topological insulators or quasi-one-dimensional materials with strong spin-orbit interactions (InAs & InSb NWs) [37, 38]. Efforts have been made to use unconventional barriers with LTS, which offer a much better compatibility and therefore nominal better interfaces, thus limiting, by low critical magnetic fields and low gap energy, for instance, the range parameters necessary to observe MBSs [39]. HTS are much harder to integrate with other systems, but present the advantage as higher critical temperature, gap energy and huge stability to the magnetic field. Device that combine semiconducting nanowires (InAs-NWs) with HTS exploit both superconducting properties available with ceramic HTS and the high-purity of InAs-NWs together with

the tunability of their transport. The NWs represent the conductive channel in a superconductor-semiconductor-superconductor field-effect transistor (SUFET) device architecture [33, 40–42] and provide an ideal mesoscopic system to study both quantum confinement and interference effects at low temperature, which is a promising platform to develop novel quantum devices, and the limits of quantum suppression of superconductivity. Nanoscale ordering and phase transition in complex oxides, where the electrons self-organize in ways qualitatively different from those of conventional metals and insulators, is one of the most outstanding problems in physics today, and studies of nanoscale devices may have a formidable impact on that.

Mixing bottom-up and top-down nanofabrication approaches have allowed building Josephson junctions in non-suspended and suspended design. Sophisticate EBL techniques have been developed and aim to align the InAs-NWs. Design device on which the InAs-NWs are positioned in random and guided (Dielectrophoresis (DEP) technique) way are fabricated. The InAs-NWs show external native oxide shell that hampers the current flux trough the interface, reason that procedures that allow to remove the oxide and get a good transparency between InAs-NWs and superconductor has been developed [24]. Current-voltage measurements as function of the temperature show, for both designs, a critical current amplitude that increases when the temperature decrease. Novel insights on macroscopic superconducting coupling in extreme conditions imposed by the nanostructures have been derived.

The nanotechnology platform developed for suspended LTS junctions has represented the starting point for the integration between YBCO, the most used HTS, and NWS. This is an extremely challenging, high risk but extremely rewarding activity. Many designs have been developed for this type of junction. Many nanofabrication problems due to the complex structure of YBCO unit cell have been solved. In order to minimize the YBCO damaging effects due to out-diffusion oxygen from unit cell the nanofabrication recipe developed includes two sessions of electron beam lithography (EBL), two e-resists (PMMA) baking steps at low temperature and for few minutes, one dry etching session performed at very low temperature and one fast wet etching

step. Special design of devices that allows verifying electric shorts before the InAs-NWs deposition have been developed. Innovative superconducting hybrid devices InAs-NWs/YBCO have been characterized with electric transport measurements as function of temperature and show as a current injected into YBCO banks can through the InAs-NWs that works as a weak link. I have demonstrated the feasibility of the fabrication procedure of YBCO/suspended InAs-NW/YBCO junctions. The first achievement of my work is that junctions YBCO/ suspended InAs-NW/YBCO of length $\sim 200nm$ are not insulating. Current passes through the InAs-NWS, demonstrating the feasibility of the whole fabrication process. The other encouraging result is that differently from InAs-NWs/Aluminium junctions resistance behavior observed for InAs-NW/YBCO devices depends on the normal length (L) of junction [43].

The work is structured in seven chapters.

The first chapter is dedicated to a review of the general mechanisms of the electric transport in the normal state.

In the second chapter an introduction to superconductivity and to the concept of Josephson coupling have been discussed.

The third chapter is dedicated to the description of the properties of InAs material (bulk and nanostructutered).

The fourth chapter summarizes all the nanofabrication procedures developed for the fabrication of non-suspended junction between InAs-nanowire and aluminium, suspended junction between InAs-nanowire and aluminium and in the last sections,the efforts accomplished for the fabrication of the novel type of hybrid systems between InAs-nanowire/YBCO will be shown.

In the fifth chapter the cryogenic system and the measurement setup used for the characterization of the devices builded are described.

In the sixth chapter the transport measures, and their elaboration, of

InAs-nanowires and aluminium junctions will be shown.

In the seven chapter the transport measurements of InAs-nanowires/YBCO junctions and their comparative analysis performed with InAs-nanowires and aluminium junctions have been performed.

Keywords:
InAs nanowire, superconducting proximity effect, low temperature superconductor, high temperature superconductor, hybrid nanostructures, semiconducting barriers, mesoscopic systems, nanostructures, nanotechnology, clean room.

This thesis is written with Latex 1.3

Chapter 1

Electrical transport theory in the normal state

In this chapter the theoretical concepts of the electrical transport in metals and semiconductors (bulk and at low dimensionality) will be introduced. We briefly outline a few relevant physical mechanisms and related models.

1.1 Overview of transport theory

A complete treatment of the transport in solid state systems is reported in classical textbooks [44–49].

1.1.1 Bulk transport

First theory of electrical and thermal conduction in the metals was formulated by Drude. He assumes metal as a free electrons gas (negative charge) on a frozen jellium of ions (positive charge background). This model neglects the interaction $e^- - e^-$ (*called independent electron approximation*), supposes an elastic and instantaneous electron-ion collisions and defines the parameter τ (called *relaxation time*) as the time between two collision events of the electron. In the same way the mean

free path of an electron (ℓ) that plays a fundamental role in the transport of low dimensional systems is defined as the length covered by the electron in the time τ. On these assumptions Drude, in the Newton's dynamics, esteems the conductivity of the metals:

$$\sigma = \frac{e^2 n \tau}{m^*} \tag{1.1}$$

where σ, m^*, n and e represent the conductibility of metal, the mass effective, the density and the charge of carriers, respectively.
Since τ takes in account the scattering mechanisms dependent on the temperature, as reported in 1.1 the trend of σ of the system will be strongly dependent on T. In addition, the relation 1.1 does not include special hypothesises on the material.
In the figure 1.1 the characteristic resistivity (ρ) as a function of the temperature for a metal (left hand side) and for a semiconductor (right hand side) is shown.

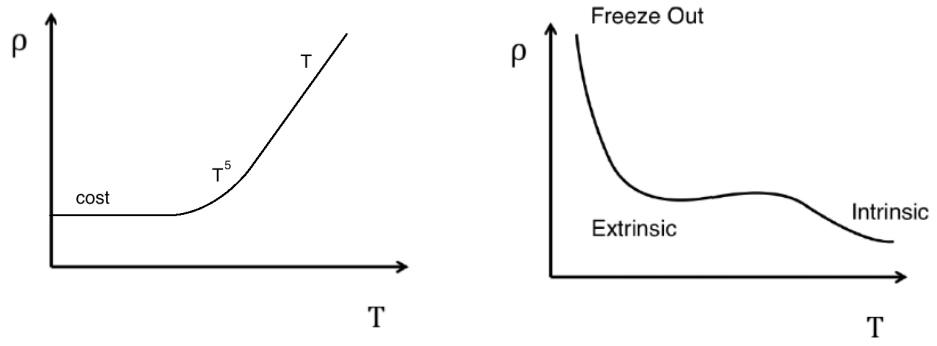

Figure 1.1: On the left-hand side the characteristic ρ as function of the T for a metal is shown. At T higher than Debye temperature (Θ_D) the ρ is proportional to the temperature. For intermediate temperatures ($T \sim \Theta_D = T^5$) the phonons do not have enough energy to move with a single scattering event an electron on opposite side of Fermi surface but many of them need: this transport mechanism is responsible of dependence of ρ on T with the power-law T^5 . At very low T unique mechanism that contributes to the resistance is the electron scattering with the impurities ($e - im$); mechanism independent on T and yields a dependence of ρ constant in temperature. On the right-hand side the characteristic ρ as function of the T for a doped semiconductor is shown. At high T the electrons have enough energy and jump from valence (C.V.) to conduction band (C.B.), where the carrier concentration increase, thus the resistivity shows a low value. In the intermediate regime all the donor atoms are ionized (called the extrinsic) and an increase of the T produces no increase in carrier concentration; for this reason a plateau in ρ is shown. At very low T (freeze out regime) electrons are not thermally excited from the bound donor to the conduction band and consequently an increase of ρ is shown.

1.1.2 Transport in low dimensional systems

By comparing the lengths L (L=$\{L_x; L_y; L_z\}$ represents the geometric sample sizes in Cartesian coordinates), $\lambda_F = \frac{2\pi}{k_F}$ (Fermi wavelength), ℓ ($\ell = v_F \times \tau$; where v_F is the Fermi velocity of electrons) and the phase coherence length ($L_\phi = \sqrt{(D \times \tau_\phi}$; where D represents the diffusion coeff. and τ_ϕ the relaxation time of phase memory) different transport regimes can be classified. For a system also the dimensionality (d) is defined: if $\lambda_F > L_x$ the transport is confined in one dimension and the free motion of carriers is limited to two spatial dimensions. This systems are called 2d-systems. If $\lambda_F > \{L_x, L_y\}$ the electrons motion is confined in two dimensions and are free to move in one dimension (systems are called 1d). For the quantum dots the relation $\lambda_F > \{L_x, L_y, L_z\}$ is verified and they are known as 0-dimensional systems. If we take in account the density of state of a system (DOS) is possible to show as the dimensionality of system changes its transport properties [44, 46, 47, 50]. In figure 1.2 the DOS dependents on the dimensionality of the system is shown.

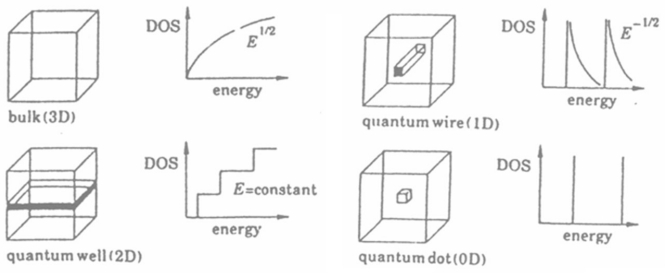

Figure 1.2: Schematic diagram illustrating the representation of the electronic DOS depending on dimensionality.

When the relation $\lambda_F \ll \ell < L$ is satisfied the carriers describe a classical dynamics. In that case, if it also verified the relation $L_\phi < \ell$ the transport follows in diffusive regime. It means that many elastic scattering events occur while the carriers are travelling through the crystal. Instead, if $L_\phi > \ell$ the carries are travelling in the system without any scattering and it is in ballistic regime. When in a system the relation

$L \leq \lambda_F$ is verified the dynamic of transport evolves in quantum regime and is described by Schrödinger equation. In this transport regime a semiconductor can be described in term of either electrons in the CB or the holes in the VB. A model that well explains the dynamic of the electrons in CB is called *single-band mass effective approximation (SBA)* [46]. The Schrödinger equation in SBA is:

$$\left[-\frac{\hbar^2}{2m^*}\frac{\partial^2}{\partial \vec{r}^2} + U(\vec{r}) \right] \Psi(\vec{r}) = \left[E - E_{CB} \right] \Psi(\vec{r}) \tag{1.2}$$

where, $m^* = \frac{1}{\hbar^2}\frac{\partial E}{\partial k^2}$ and thus takes into account the energy band curvature, E_{CB} represents the bottom of the CB and $U(\vec{r})$ includes the potential of crystal as well as the potential of impurities. The equation 1.2 depends on the dimensionality of the system through its confining potentials and its wave function factorizations. In the Tab 1.1 the different electronic transport regimes are summarized.

Transport Regimes			
Classical		**Quantum**	
Ballistic	**Diffusive**	**Ballistic**	**Diffusive**[1]
$\lambda_F \ll L < \ell$	$\lambda_F \ll < \ell < L$	$L \leq \lambda_F < \ell < L_\Phi$	$\ell < L_\Phi < \lambda_F \leq L$

Table 1.1: A summary of the electric regime transports.
[1] A system that evolves in the quantum diffusive regime can also include, when is verified that $\lambda_F << \ell < L_\Phi < \xi_\ell$ (where ξ_ℓ defines a length on which the electron is localized in the material.) weak localization corrections which leads to a decrease in conductance [1] or to corrections due to the strong localization effects when $\lambda_F < \ell < \xi_\ell < L_\Phi$ [13].

A new length scale (called thermal coherent length) that depends on T and defines the length on which the electrons travel inside the material without loss of the phase is $\xi_T = \sqrt{\frac{\hbar D}{k_B T}}$. ξ_T plays a fundamental role in the electronic transport of superconducting hybrid systems [51].

1.2 1d-system: Quantum Wires

The NWs used in this thesis represent quasi-1-dimensional system ($d \simeq \lambda_F$). We assume that the NWs has rectangular section as is shown in fig.1.3-a. The electrons are confined in plane parallel to the wire cross section (x,y) and are free to move only along axial axes of the wire (z). The single-electron Hamiltonian in the effective-mass approximation is $H = -\frac{\hbar^2}{2m^*}\nabla(\overrightarrow{r})^2 + V_{eff}(\overrightarrow{r})$, where $V_{eff}(\overrightarrow{r})$ includes the potential of the band discontinuities, the electrostatic potential of the ionized donors and acceptors and the many-body contribution due to free carriers [50]. The wave function $\Psi(x,y,z)$ of the NWs is factorable as $\Psi(x,y,z) = \phi_{n,m}(x,y)e^{ik_z z}$, where $\phi_{n,m}$ represents the wave function of the electrons confined in the (x,y) plane and $e^{ik_z z}$ is the free component along the z direction. Thus, the constraint in the plane (x,y) defines the discrete sub-band energy levels reported in the eq.1.3. A sketch of the E-k relation for three sub-bands is show in 1.3-b.

$$E_{n_x,n_y} = E_{CB} + \frac{\hbar^2 k_z^2}{2m^*} + \frac{\hbar^2\pi^2}{2m^*}\left(\frac{n_x^2}{L_x^2} + \frac{n_y^2}{L_y^2}\right) \tag{1.3}$$

where L_x and L_y represent the size of the NW along x and y axes, respectively and $n_x, n_y = 1, 2, ..$ are the number of energy sub-bands. The quantization effect is yielded when the conduction in the sub-band "n" moves to "n+1" [50, 52].

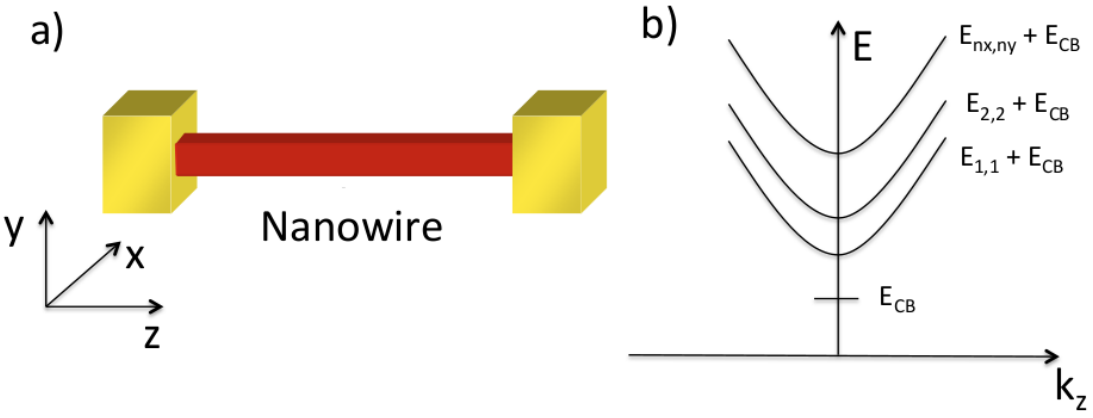

Figure 1.3: A sketch of NWs with rectangle cross section (a) and the dispersion relation plotted for the lowest three modes of the electrons confine in 2 dimensions is shown.

1.3 Disordered electronic systems

The periodicity of a ideal crystal guarantees the validity of the Block's theorem allowing to calculate the band structure also for complicated crystalline materials. In real crystals the disorder (impurities, vacancies or dislocations) exists in varying degrees and breaks the translational invariance of the Hamiltonian of the system hence the of Block's theorem. All these imperfections produce bound states that can bind or release electrons. As the degree of disorder increases the mean free path (ℓ) of the system decrease. As increase the disorder leads the wave function of an electron to be localized to finite and small region of the system and vanishes exponentially decaying on the spatial localization length ξ.

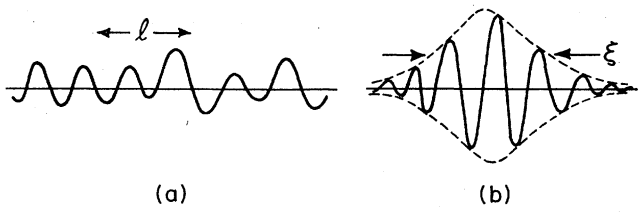

Figure 1.4: The sketch shows (a) wave function of an extended state with mean free path ℓ; (b) wave function of a localized state which amplitude is maximized inside the localized region and vanishes exponentially outside [1].

1.3.1 Anderson theory of the localization

In 1958 Anderson was the first to describe the localization effect of the electronic wave function dues to the disorder. His wave function has form

$$\Psi \sim \exp^{-(r-r_0)/\xi} \tag{1.4}$$

where the r defines the spatial distance away from the localized state in the position r_0.

1.3.2 Transport in extended states

The electron transport theory of these systems, where the Fermi energy remains within the extended states, is based on the Boltzmann formalism [47] whose condition applies if $\lambda \ll \ell$ (it means far from pure quantum regime), where λ and ℓ are the De Broglie wave length and the mean free path, respectively.

1.3.3 Transport in localized states

For localized states the relation $\lambda \ll \ell$ is violated but the electric transport is possible via hopping between the neighbouring localized states. Since the wave function for each localized state has the form 1.4 as a result there is a finite probability that a transition between these two neighbouring states occurs by the tunnelling of an electron from one site to the other. It is possible that the overlapping between the wave

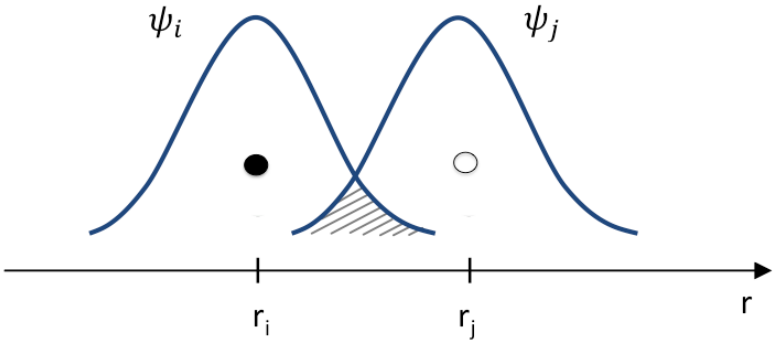

Figure 1.5: The sketch shows the wave functions Ψ_i and Ψ_j overlapped of the neighbouring sites i and j. The black and white circles define the full and empty sites, respectively.

function of two neighbouring states, with energy E_i and E_j, respectively, occurs but in that case the difference of energy $\Delta E = E_i - E_j$ necessary for the hopping can be provided by a phonon. Miller and Abrahams [2] were the first to describe the electrical transport between localized states using the hopping mechanism and found that the conductivity of the system can describe by 1.5.

$$\sigma(T) \sim \exp^{-(E_i - E_j)/k_B T} \tag{1.5}$$

1.3.4 Mott model

Mott [53] noted that if the temperature comes down the phonons energy is not enough to assist the electron hoping ($\Delta E = E_i - E_j$), but the transport is still available in a band energy close the Fermi energy. In this picture the phonons can still assist the hop of electron between the available sites and the probability of occupancy is higher for sites spatial far but near in energy that the vice versa (see the sketch in fig. 1.6). In the Mott model, at low temperature the conductivity is given

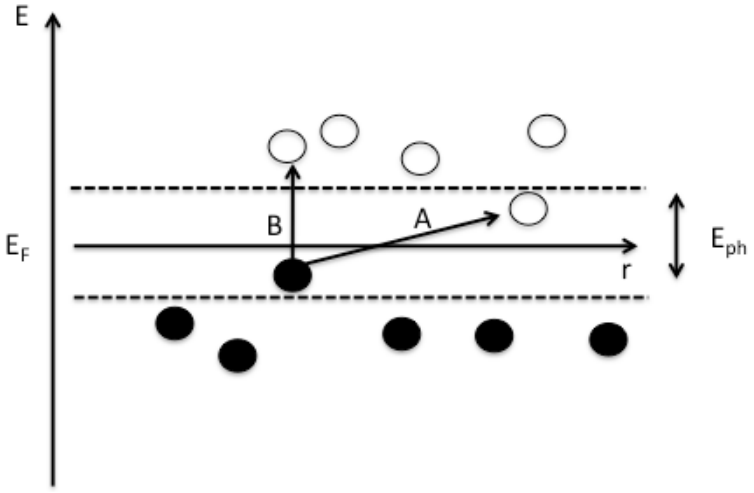

Figure 1.6: The sketch shows the electronic transport in the Mott model. Close the Fermi energy E_F a narrow energy band wide E_{ph} low-energy available phonons can assist the electrons hopping. The carriers prefer to hop on lower energy sites, thus the mechanism A is preferred to B. The black and white circles define the full and empty sites, respectively.

by 1.6

$$\sigma(T) \sim \exp^{-(T_a/T)^{1/(d+1)}} \tag{1.6}$$

where d is the dimensionality of the system and T_a (activation temperature) depends on the density of states of the systems.

1.3.5 Weak localization

The presence of small degree of disorder in a system can produces coherent quantum mechanical backscattering which gives several of quantum transport effects such as the logarithmic dependence of the conductivity

on the temperature [54] that can be explained in terms of weak localizations. These effects exist also in system without any electron-electron interactions (electron-electron interaction leads to other term of corrections of the conductivity). The weak localization corrections has purely a quantum origin: it stems from quantum interferences of an electron moving along self-intersecting trajectories (e.g., in fig.1.5 an electron that starts from the site r_i can reach the site r_j moving along several paths including backscattered paths. These scattering events are predominately elastic, thus the elastic scattering time τ is shorter than the phase coherence time τ_Φ that is preserved along the path $r_i - r_j$). The correction of weak localization to the conductance of the systems are proportional to the return probability of an electron diffusing in un disorder media and depend on the dimensionality and the temperature of the system. $L_\Phi = \sqrt{D \times \tau_\Phi}$ determines the spatial scale of length on which the quantum interference effects occur. At low temperature τ_Φ is large and, for example, as in the case of granular metals, in which the size of a single grain $a \sim (5-10)nm$ (in these systems the grain size "a" plays the same rule that the man free path ℓ in the normal media) L_Φ exceeds the length of many grains, thus the electron trajectories can involve many grains crossing many time its path significantly contributing to the conductivity of the system.
Increasing the temperature decoherence length decreases and as $L_\Phi \sim a$ the electron trajectories are completely included in the grain size, thus suppressing the weak localization corrections [54]. The quantum interference corrections due to the weak localization are $\delta\sigma_{WL} \sim ln(\tau_/\tau_\Phi)$, where τ is the time between two events of scattering. The corrections $\delta\sigma_{WL}$ are suppressed applying a weak magnetic field. This can serve as a immediate experimental test for identifying the contribute of the conductivity of the system yielded by weak localization effects.

1.4 Scaling theory of localization

The scaling theory tries to explain the localization problem by considering the behaviour of the conductance g as a function of the size (L^d) of the system. This approach allows a description of the system in terms

of extended and localized states. Abrams, Anderson, Licciardiello and Ramakrishnan [2] argue that the function ($\beta(g)$ is called scaling function) $\beta(g) = \frac{dln(L)}{dln(g)}$ depends on g alone. In this way the degree of disorder of the system is defined by a single parameter g.

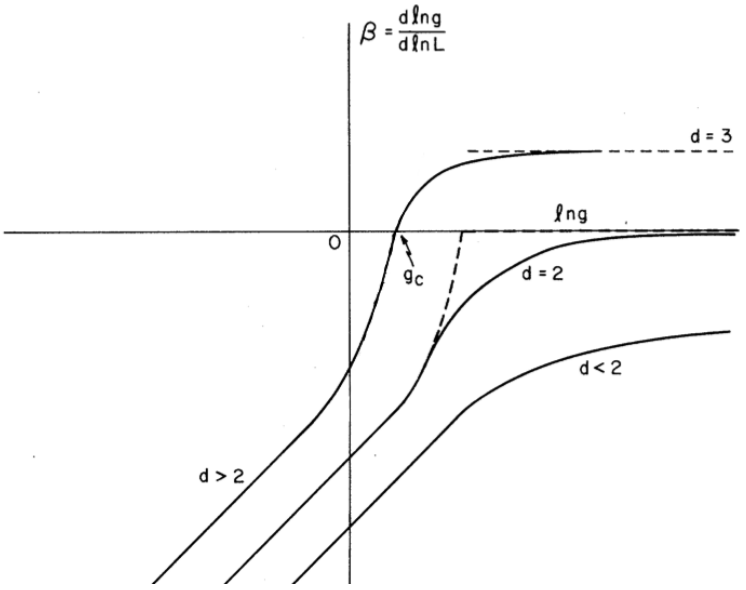

Figure 1.7: The scaling function $\beta(g)$ as a function of logarithm of the conductance for different dimensions of the system and at zero temperature. The positive values of $\beta(g)$ define extended states. For $\beta(g) < 0$ all the states are localized, thus extended states for d=1 and d=1 systems are forbidden. For d=3 the point $\beta(g = g_c) = 0$ is an unstable critical point: for small change the scaling function abruptly assumes a different regime. The image has been adapted from [2].

- **If $g \gg g_c$**
  Only for d=3 the metal-insulator transition involves and the system is in the Ohmic regime. For d=2 and d=1 leads to the asymptotic form $\beta(d) = 0$ and $\beta = 1$, respectively.

- **if $g \ll g_c$**
  Electronic states are localized independent of dimensionality d.

In the case of weak disorder regime ($k_F\ell \gg 1$) the function β assumes form $\beta(d) = (d-2) - a/g$, where "a/g" represents a term dues to the quantum correction. Changing the dimensionality d of the system the scaling function $\beta(ln(g))$ is yield.

Chapter 2

Theory of superconductivity

In this chapter concepts of the theory of superconductivity and models useful for understanding the electrical properties of superconducting junctions will be introduced.

2.1 Introduction to superconductivity

The superconducting state represents the phase of special materials that display zero resistance and perfect diamagnetism below a material dependent critical temperature (T_c). When a weak external magnetic field (B) is applied to the bulk material penetrates the superconductor to a very small distance, characterized by a parameter λ (called ***London penetration depth***), length on which B decays exponentially to zero inside the material [55, 56].
The first quantitative but macroscopic theory of superconductivity was advanced by Ginzburg and Landau (GL). They describes the superconducting state by means of an order parameter ($\Psi = \sqrt{\rho}e^{in\varphi}$; where ρ and φ represent the density of Cooper pairs and the superconducting phase, respectively and $n \in \mathbb{Z}$). The coherence length of a superconductor (ξ) is another important parameter introduced by GL and describes the distance over which Ψ is not constant. In addition, experiments show that the T_C of superconductors is modified by changing the isotope of the elements that form the sample. This result claims that electron-phonon coupling plays an essential role in the phase transition to the

superconducting state.

A first microscopic interpretation of the superconducting state was revealed by Bardeen, Cooper and Schriefer theory (BCS) in 1957. The BCS assumes that the superconducting state is made up of coupled electrons (called Cooper pairs). The electron-electron electrostatic attraction is due to the vibrations of crystal lattice. An electron travels through the crystal and it distorts the lattice. In this way a phonon is created and is absorbed by a second electron that an instant after the first one is travelling in the crystal. Since the propagation speed of the electron is greater than the phonon ($\sim 10^5 cm/s$ and $\sim 10^8 cm/s$ respectively), this difference allows an electron-phonon attractive interaction and ensures that the mean distance between the two electrons is large. The net result of this mechanism is that the electron-electron attraction mediated by a phonon outweighs the electronic Coulomb repulsion thus a Cooper pairs is assembled [57]. In the BCS framework, consideration on symmetry and energy of the superconducting system require that the electrons of Cooper pairs have opposite wave vector and spin (means that the total momentum a spin of Cooper pair, in the centre-of-mass frame, are equal to zero). In addition, the electrons of the Cooper pairs are allocated around the Fermi surface within an energy band $\hbar\omega_D$, where ω_D represents the Debye frequency of the phonons. The onset of superconductivity is accompanied by the opening of a temperature dependent energy gap $2\Delta(T)$ at the Fermi level; the energy cost from the increase in kinetic energy that is associated with the occupation of states above E_F is also outweighed by the reduction in energy achieved by the formation of the Cooper pairs. Therefore, $2\Delta(T)$ defines the amount of energy needed to break the Cooper pair.

The analysis of exited states, at T=0K, in the BCS framework is achieved by appropriate transformations (called canonical transformations) that describe the creation and annihilation of quasiparticles and leads to the Bogoliubov-Valatin equations [55]. Only in 1958 Gor'kov showed how it is preferable a generalisation of the microscopic theory of the superconductivity in terms of single-particle Green's functions [58] that allow to take in account the temperature dependence of the system. In the case of time-independent and uniform medium, the Gor'kov's equations give to the relations 2.1, reasonably in agreement with the same get by BCS

theory.

$$\begin{cases} \dfrac{\Delta_0}{k_B T_c} \approx 1.76 \\ \Delta(T) \approx 3.06 k_B T_c \Big(1 - \dfrac{T}{T_c}\Big)^{1/2};\ T_c - T \ll T_c \\ H_c(T) \approx 1.74 H_C(0) \Big(1 - \dfrac{T}{T_c}\Big); T \to T_c \\ \Big[\dfrac{C_s - C_n}{C_n}\Big] \approx 1.43 \end{cases} \tag{2.1}$$

where Δ_0 represents the superconducting gap a T=0K, $H_C(0) = [4\pi N(0)\Delta^2(0)]^{1/2}$ defines the magnetic critical field at 0K, $N(0)$ is the superconductive density of carriers and C_s, C_n represent superconducting and normal state heat capacity, respectively.

2.2 Superconducting junctions

In 1962 Brian Josephson predicted that when two extended banks of conventional superconductor are separated by a barrier (L) of insulating material (I), if I is enough thin a supercurrent (I_c) can flows through it. I_c depends on the difference of phase between two superconducting banks [59]. The Josephson effect is described by two equations 2.5 and 2.6. After this discovery many experimental tests have been done and the Josephson effect has been generalized to systems where the barrier is a normal metal or a ferromagnet, or even to a constriction of the same superconducting material of the electrodes and of opportune dimensions [51, 60–63]. In the next section the Josephson theory will be explained. Since I have realized and studied also junctions between HTS and Sm, it will be necessary to explain how the anisotropy of the order parameter in HTS affects the dynamics of the junctions.

2.2.1 Josephson effect

If we consider two independent superconducting banks and assume that their have the same amplitude of the order parameter Ψ_L (Ψ_R) (letf (L) and right (R) bank) but a different phase, the evolution of these two

systems is analyzable through ordinary Schrödinger 2.2:

$$i\hbar\frac{\partial\Psi_L}{\partial t} = H_L\Psi_L$$
$$i\hbar\frac{\partial\Psi_R}{\partial t} = H_R\Psi_R \tag{2.2}$$

If the superconducting banks are brought towards each other, when distance between them will be of the same order of the coherent length a coupling (K) starts. The coherent length depends on the type of barrier: in the case of junctions with an insulating barrier (SIS) it is represented by ξ, instead in the case of normal or semiconducting barriers (SNS or SSmS junctions) the coherent length that needs to takes in account is ξ_T [51]. Hence, the set of equations 2.2 needs to take in account the coupling of two system-banks [64]:

$$i\hbar\frac{\partial\Psi_L}{\partial t} = E_L\Psi_L + K\Psi_R \tag{2.3}$$
$$i\hbar\frac{\partial\Psi_R}{\partial t} = E_R\Psi_R + K\Psi_L \tag{2.4}$$

From the 2.4 performing some calculation the current-phase relations (CPR) 2.5 and the equation that takes in account the time evolution of ϕ (2.6) is got:

$$I_s = \sum_{n=1}^{\infty} I_n sin(n\phi) \tag{2.5}$$
$$\frac{\partial\phi}{\partial t} = \frac{2e}{\hbar}V \tag{2.6}$$

where I_s and ϕ represent the supercurrent that flows through the junction and the phase difference of the superconducting order parameters, respectively. In many cases only the first term of sum is sufficient to define the Josepshon effect. A general representation of the I_s in Josepshon junctions (JJ) can be written as $I_s = I_c sin(\Phi)$, where $I_c = max[I_s]$. The equations 2.6 and 2.5 describe the dynamic of the junction [51, 55, 65].

The JJ is a manifestation of the macroscopic quantum nature of the superconductivity.

2.2.2 SIS junction

The first real microscopic quantum dynamics description of Josephson junctions, that includes dissipative effects of quasiparticle tunnelling, was formulated by Ambegaokar and Baratoff (A.B.) [66]. They used the Green's function method, a powerful tool in many body problems, to generalize the calculation of Josephson effect to finite temperatures. Their model valids in the tunnel junction limit, yields the CPR reported in 2.7.

$$I_s = \frac{2\pi T}{eR_n} \sum_{\omega_n > 0} \frac{\Delta_1 \Delta_2}{\sqrt{(\omega_n^2 + {\Delta_1}^2)(\omega_n^2 + {\Delta_2}^2)}} sin\Phi \tag{2.7}$$

where Δ_β, with $\beta = 1, 2$, $\omega_n = \pi T(2n+1)$, R_n represent the superconducting gap of the banks placed at L and R of the tunnel barrier, the Matsubara frequencies and the resistance of the normal state, respectively. For temperature close T=0K and assuming that the amplitude of the gap function for both the superconducting banks is the same ($\Delta_1 = \Delta_2$) and $sin\Phi = 1$, on these hypothesis the 2.7 becomes a very easy relation 2.8.

$$I_c = \frac{\pi \Delta(0)}{2eR_n} \tag{2.8}$$

2.2.3 SNS junction

Further studies have shown that the Josephson effect can also exist if two superconductors are connected by a weak link (as a normal metal, ferromagnetic, semiconductor, superconductor with smaller critical temperature, constriction, ...) [65, 67]. Aslamazov - Larkin (AL) tried to explain the Josephson effect in weak links for temperature close to T_C. This model well works when the length L of the weak link is shorter than the superconductive coherent length ($L << \xi$) moreover does not depend on weak link properties. The CPR in AL limit is reported in 2.9:

$$I_s = \frac{\pi \Delta_1 \Delta_2}{4ek_B R_n T} sin\phi \tag{2.9}$$

AL model can be generalized to low temperatures and the CPR shows deviations from the $sin\phi$, which can be quite significant, and also depends on the the mean free path of the weak link ([3, 65]). Another

important model for SNS junctions has been formulated by Kulik and Omelyanchuk (KO). KO assumes that the weak link is a 1-dimensional structure ($W << L << \sqrt{\xi_0 l}$, where W, L and $\xi_0 = \frac{\hbar v_F}{2\pi T}$ represent width, length and coherent length of the weak link, respectively), that the junction is symmetric and works in diffusive regime ($\ell \ll \xi_0$). In KO limit the CPR is reported in 2.10 and in figure 2.1 the I_s as function of Φ at various T is shown.

$$I_s = \frac{4\pi T}{eR_n} \sum_{\omega_n > 0} \frac{\Delta cos(\phi/2)}{\sqrt{\Delta^2 cos^2(\phi/2) + \omega^2}} \tag{2.10}$$

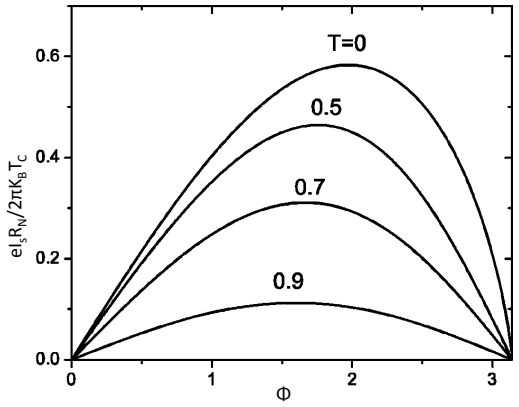

Figure 2.1: CPR in KO model at various temperature. For T close to T_c the CPR becomes the same shows by AL. At low temperature the CPR is not sinusoidal. This graph has been adapted from [3].

2.2.4 SINIS junction

Interest in SINIS junctions is related to their possible applications in superconducting electronics. Junctions in which several types of weak links that carry large supercurrents were reported by Klapwijk and Kleinsasser. This is the natural limit of SNS junctions for lower barrier transparency. This often happens in SNS junctions where the normal barrier is represented by a semiconducting link [3].

The properties of SINIS junctions were analyzed in the Usadel framework. An analytic equation for CPR includes through the parameter (γ_{eff}) the interface between the weak link and superconducting banks [3]. γ_{eff} is defined as $\frac{\gamma_{B1}\gamma_{B2}}{\gamma_{B1}+\gamma_{B2}} * L$, where $\beta = \{L, R\}$, $\gamma_{B_\beta} = \frac{R_{B_\beta}}{\rho_\beta \xi_\beta}$, R_B is the

resistance of barrier and ρ_β and ξ_β represent the normal resistivity and the coherent length of superconducting banks, respectively. In the Usadel framework the material properties of the weak link are also taken into account. In figure 2.2 the I_c vs T for a SINIS symmetric junction that works in the diffusive limit for various γ_{eff} values is plotted.

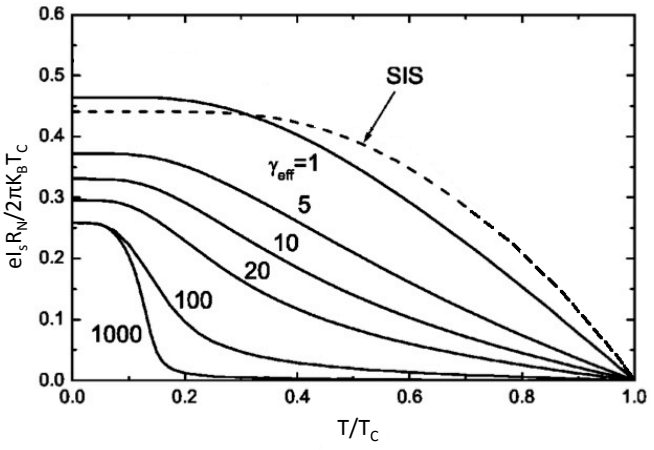

Figure 2.2: Dependance of supercurrent I_c on the temperature T for a SINIS symmetric junction in diffusive regime. The curves are plotted for various values of barrier (γ_{eff}). The dashed curve represents the limit of SIS junction in AB model. This graph has been adapted from [3].

2.2.5 Andreev reflection

?? A simple microscopic model that allows to interpret how a supercurrent can flow though a Superconducting/Normal (SN) junction can be discussed within the Blonder, Tinkham and Klapwijk (BTK) framework [68]. This approach has the advantage to allow an its direct experimental application. They consider an 1-dimensional ballistic channel with a step like variation of the superconducting order parameter $\Delta(x) = \Delta\Theta(x)$. The model takes in account the effect on the superconducting parameters of the S/N interface through a potential $U(x) = H\delta(x)$. For this reason BTK defines a parameter Z strongly related to the transparency coefficient of the barrier that ranging from 0 (metallic limit) to ∞ (tunnelling limit).

If we consider an incoming electron from the normal metal with energy $E < \Delta$ that reaches the SN interface, it can only yield two possible

reflection mechanisms: normal reflection or Andreev reflection (AR) [69]. While former mechanism does not allow a current flow through the interface, latter process adding a Cooper pair to the superconducting condensate and simultaneously, in the normal metal, a hole with opposite spin to the incoming electron is back reflected 2.3. The AR allows to explain how in the junctions between superconductors and normal (or semiconducting) materials the superconducting properties can propagate and influence the electric transport of the normal (or semiconducting) material: this physics phenomena is known as "superconducting proximity effect" [67]. In the case of superconducting junc-

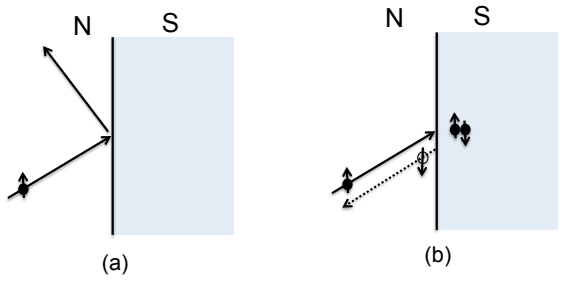

Figure 2.3: Sketch of normal reflection (a) and Andreev reflection (b).

tion made by not s-wave superconductors (e.g. HTS materials that as will be explain in the following section shows a d-wave order parameter) the mechanism of Andreev reflection becomes a bit more complicated [70, 71]. AR in HTS junctions needs to take in account the angle dependence (α) of the superconducting order parameter as well as the angle incident of the electron at N/S interface. The generalization of BTK theory that considers also the anisotropy of superconducting order parameter has been developed by Kashiwaya and Tanaka [72]. In the figure 2.4 the conductance as function of voltage applied for two different junctions made with s-wave and d-wave superconductors are reported. The graphs also include, through the parameter Z, different transparencies at S/N interface.

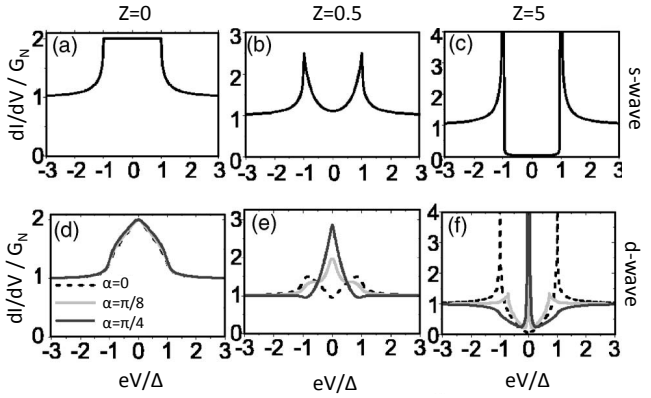

Figure 2.4: Conductance as function of the voltage, in the BTK framework, for two different types of junctions (N/s-wave Sc and N/d-wave Sc) are shown. The plots (a,b,c) are related to N/s-wave junction and include three different transparency values. The plots (d,e,f) are related to N/d-wave Sc junctions and also take in account the anisotropy of order parameter in unconventional superconductors. This graph has been adapted from [4].

2.2.5.1 Multiple Andreev Reflection

The AR mechanism can be also applied to the junctions made with a weak link placed between two superconducting banks (SNS or SSmS). In this process an electron that moves on the left SN interface will be Andreev reflected as a hole that travels to the right NS interface where will be again Andreev back scattered as an electron. If this mechanism is iterated a current of correlated electrons can flow between two opposite superconducting banks. This transport process is called multiple Andreev reflections (MAR) and in the case of a symmetric junction subharmonic gap structures appear at energy $eV = \frac{2\Delta(T)}{n}$, where $n \in \mathbb{N} - \{0\}$. The MAR appear as peaks in the conductance-voltage (G-V) measurements. In figure 2.5 the characteristic G-V shows the MAR for a Al-graphene-Al junction. A complete theoretical treatment has been done by Octavio et al. [73].

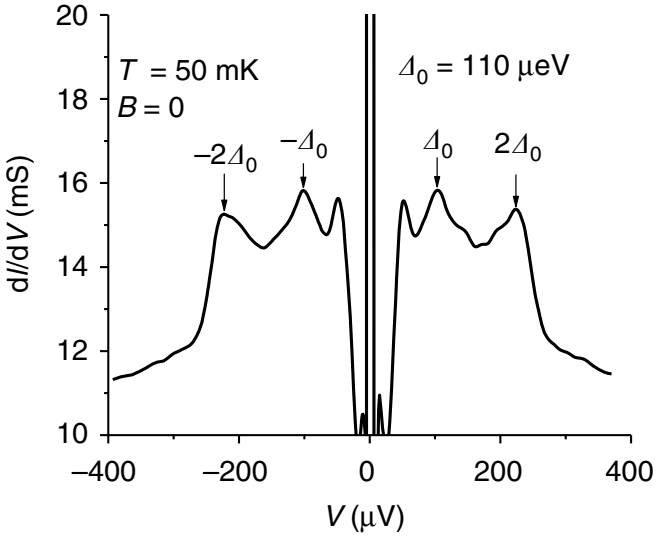

Figure 2.5: Differential conductance (dI/dV) measured at T=50mK for a SNS junction with the normal region made by graphene covered on two sides with aluminium. MAR peaks are denoted by arrows. This graph has been adapted from [5].

2.3 Exotic superconductivity

High Temperature Superconductors were discovered in 1986 by J. G. Bednorz and K. Muller [74]. They observed superconductivity up to 38K in the compound $LaCuO$ doped with Ba or Sr atoms. This result paved the way to a new strand of research. Subsequently more superconducting compounds have been brought to light. $YBa_2Cu_3O_{7-\delta}$ represents the most studied HTS material with T_C, doping dependent, up to 92K. More complex alloys as $Bi_2Sr_2CaCu_2O_8$ [75] and $Tl_2Ca_2Ba_2CuO_{10}$ [76] have been discovered and show a T_C up to 105K and 120K, respectively. Latest researches show that mercury-based compound $HgBa_2Ca_2Cu_3O_8$ has $T_C = 130K$; it represents the highest T_C value of any material [77].
The structure of HTS is quite complex. These compounds have layered made by $Cu-O$ planes; for this reason are called *cuprates*. Since $Cu-O$ planes work as charge reservoirs HTS substantially behave as quasi-2 dimensional systems. The T_C of the cuprate superconductors, for fixed doping factor (δ), depends on the number of CuO_2 planes and increases with their number till to reach the maximum value of T_c (the last depends on the δ value chosen). Due to complex structures, HTS show

a strong anisotropy of the superconducting order parameter that manifests in the transport properties [78]. After 30 years the research in the HTS filed is still active. From the experimental side much work has been done with the aim of improving the quality of the films [79–81]. In the last few years, thanks to the advancement in nanotechnologies applied to superconductors (sophisticated nanopatterning procedures have been developed [82? –92]) accompanied by the advances in a better understanding of the properties of HTS and of HTS devices has allowed to open a novel scenarios and interest in the superconducting nanoelectronic at high temperature. Strong difficulties caused by complex structure of cuprate have slowed down the development of theories for the explanations of their superconducting nature. BCS theory, that well works for s-wave Sc, becomes inadequate for this type of superconductors thus more complex theories are necessary.

2.3.1 $YBa_2Cu_3O_{7-\delta}$

The unit cell of the compound YBCO shows a complex structure (see fig2.6). The stoichiometric but not superconducting phase of YBCO compound is represented by $YBa_2Cu_3O_6$ and shows a tetragonal unit cell. The superconducting YBCO is not a stoichiometric compound and the symmetry of the unit cell is orthorhombic. The yttrium (Y) and barium (Ba) atoms are found between the CuO_2 planes and between the CuO_4 ribbons and CuO_2 planes, respectively. The weak coupling between CuO_2 planes leads to a weak superconductivity in the perpendicular direction differently happens in the planar direction. It is to be noted that there are $Cu-O$ chains along the b-axis. The presence of oxygen atoms in these chains are essential for superconductivity. A variation of oxygen stoichiometry (δ) defines a different phase of the material. YBCO is a hole doped compound and in figure 2.7 its phase diagram is shown.

Since the oxygen plays basic role in the superconducting transport of the cuprate the nanofabrication recipe developed for the fabrication of the devices includes steps that aim to avoid the loss of oxygen (e.g. bake of e-resists at low temperature and for few minutes, short wet etching and dry etching are performed at low temperature.) For this

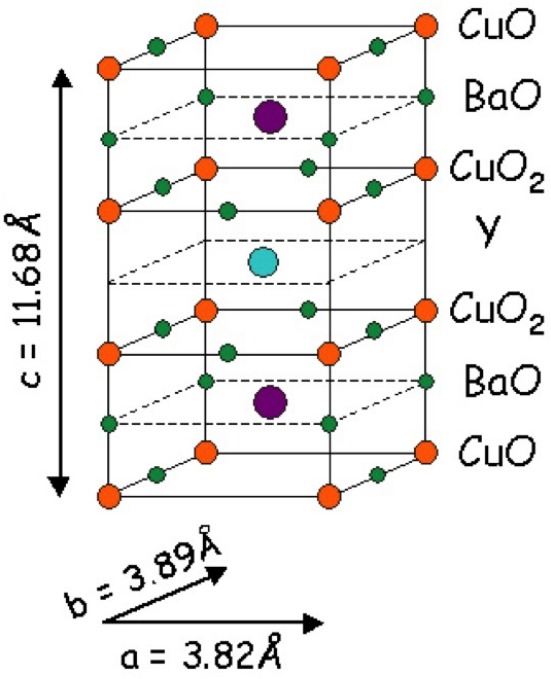

Figure 2.6: Unit cell of $YBa_2Cu_3O_{7-\delta}$ in shown. The lattice parameters are: a≈3.89Å, b≈3.82Å, c≈11.68Å. This image has been adapted from Hoffman Lab - Harvard University, web page `http://hoffman.physics.harvard.edu/materials/images/ybco.gif`.

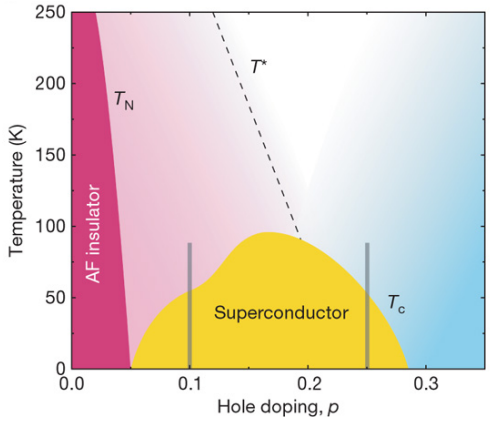

Figure 2.7: Phase diagram for hole doped superconducting cuprate. For $\delta > 0.6$ the compound shows an antiferromagnetic phase. If $\delta < 0.6$ the superconducting behaviour of the material is shown; when $\delta \sim 0.16$ the optimal doped point is reached and $T_C \sim 94K$ is shown. Above T_C and to the left of T^* the phase of material is called "pseudo gap". in this regime the microscopic mechanisms that lead the electric transport are not clear. Above T_C but on the right side of T^* the compound assumes a metal like behaviour. The image has been adapted from [6].

reasons, the investigation of this compound on the nanoscale is really challenging. Differently to LTS that shows the s-wave symmetry of Φ,

experimental observations confirm evidence of d-wave symmetry for Φ of HTS [78, 93–95]. In the Tab 2.1 the main parameters of optimal doped YBCO compound are summarized.

$T_C(K)$	92
$\Delta(0)$(meV)	20-25
λ_L^a (nm); λ_L^b (nm); λ_L^c (nm)	150-300; $\lambda_L^a/2$; 1000
$\xi^a = \xi^b$(nm); ξ_c (nm)	1-3; 0.24
$H_{C2}^a = H_{C2}^b$(T); H_{C2}^c(T)	250;120

Table 2.1: Main parameters for YBCO optimal doped.

Chapter 3

Indium Arsenide

In this chapter the main properties of the InAs semiconducting material bulk and with reduced dimensionality will be shown. InAs semiconducting nanoowires will be used as barriers and we will be particularly interested also in their capabilities of forming good interfaces.

3.1 InAs bulk

Bulk InAs growth on GaAs substrate shows at 300K a carrier mobility value (μ) up to 30000 $cm^2/(Vs)$, high intrinsic electron concentration (up to $n \sim 10^{18} cm^{-3}$) and, thus, low intrinsic resistivity $\sim 100\Omega/\square$ [96, 97]. In fig.3.1 shows a sketch of the band structure of InAs. InAs is a direct band semiconductor with a band gap of 0.35 eV at room temperature. The effective electron mass at the Γ-valley point is m^*=0.023m_e. More details on the properties on the bulk material are reported in [7]. Tunnelling measurements show that a natural narrow accumulation layer of electrons exists at InAs-oxide interface and result from donor surface states which pin the Fermi level above the conduction band [98]. The thickness of this layer is of the order of an electron wavelength (for this reason in the InAs bulk quantization effects are displayed) and therefore shows a natural two-dimensional electron gas at its surface. The donor states give rise to an increase of electron-impurity scattering mechanism which represents a factor that limit the μ of the material;

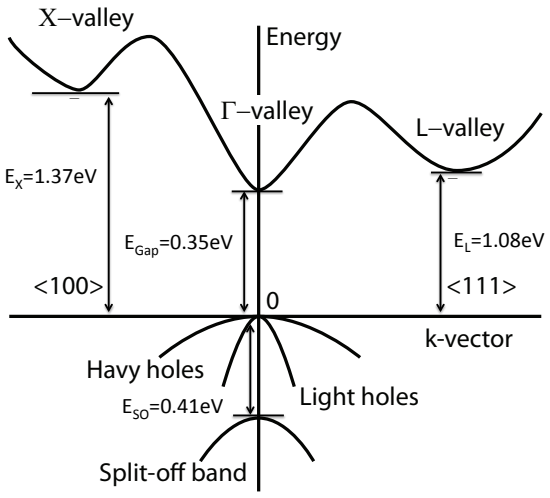

Figure 3.1: Diagram band energy of InAs. The figure has been adapted from [7].

in fact the μ in surface is much lower than the bulk value [99]. To eliminate also the undesirable effect of the surface on device properties a "passivation" step with ammonium polysulphide solution is commonly used [29]. Next section more details about the treatment of the semiconducting surface of the material used in this thesis will be give.

3.2 InAs Nanowires

Indium Arsenide (InAs) NWs strongly n-doped by selenium represents the semiconducting material that work as transport channels in the devices fabricated during this thesis. The NWs are provided by L. Sorba group and have been grown by Au-assisted chemical beam epitaxy (CBE) on InAs (111)B substrates. They have an average diameter (d) and length (L) of 90nm and $2\mu m$, respectively. By a fine tuning of the temperature of the substrate and of the pressure of the gases injected in the chamber, L and d as well as the intrinsic transport properties of NWs can be well fixed (see ??). InAs-NWs strongly n doped belonging to the same batch of growth used for the fabrication of superconducting hybrid devices show a variability more than 10% on its diameter and length. Concerning the resistivity (ρ) of the NWs several junctions have been tested with electric measures and results show as

$\rho assumes a broad range of values \sim [1;10]\Omega \times nm. The growth of NWs is followed by Reflective High$
$-$**102**].

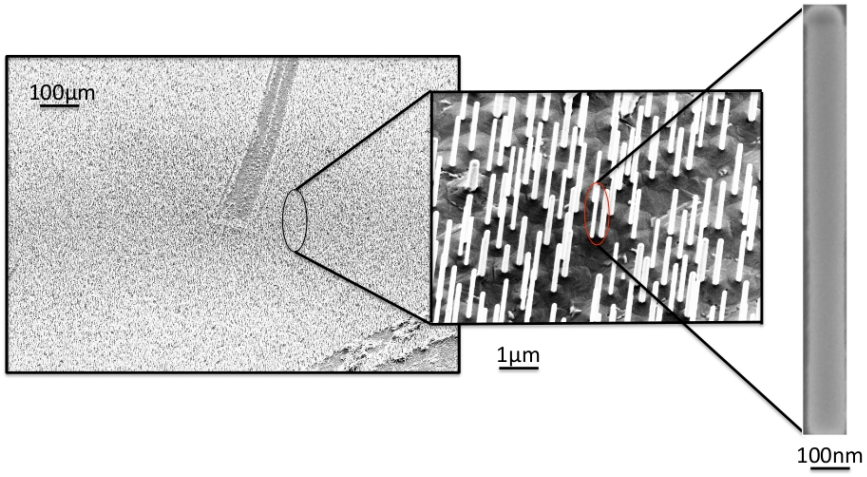

Figure 3.3: SEM images of a InAs-NWs: from the the chip of growth (on the left hand side) to, on the opposite side, a single NWs (long $\sim 2\mu$m and d$\sim 90nm$) is shown.

The NWs are surrounded by a native oxide layer few nanometers thick [103–105] that hampers the flow of current when is contacted without a suitable cleaning. In the next subsection details on InAs NWs surface treatment will be reported.

Theoretical calculations on InAs-NWs show (see fig.3.4) that when decreasing the diameter of the NWs, the lateral confinement starts to have a strong effect on the band structure of the channels, splitting the different sub-bands and increasing their effective masses [8]. Experiments in agreement with theoretical prediction on the effects of the quantum confinement on the transport properties in InAs-NWs are reported in [106].

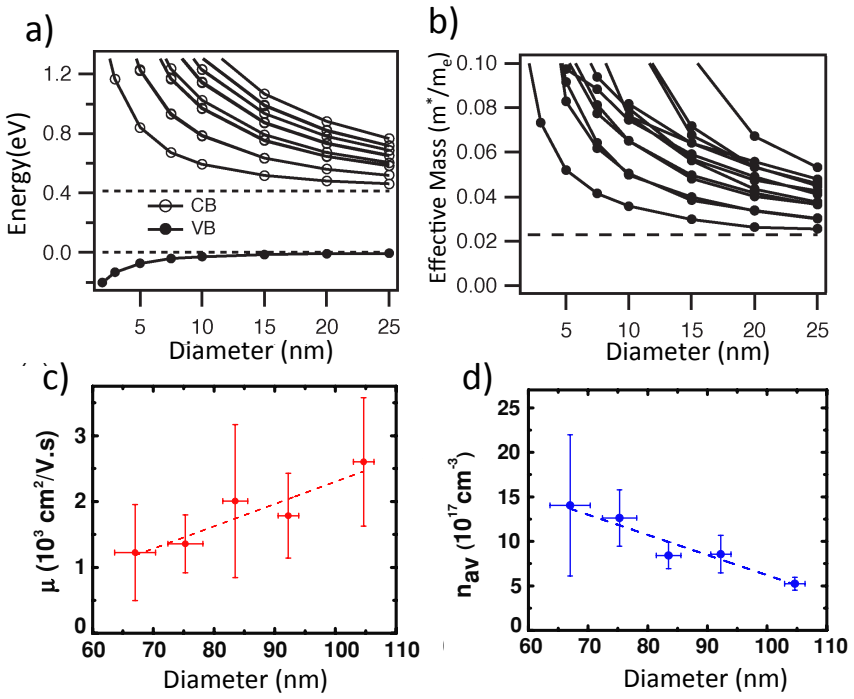

Figure 3.4: (a) Conduction and valence energies subbands calculated at Γ point are plotted as function of the diameter of the NWs. The dashed lines represent the bulk position of the valence and conduction band, respectively. (b) The effective mass of the conduction subbands calculated at Γ point as function of the diameter of the NWs is shown. The dashed line represents the bulk effective mass for InAs $m^* = 0.023m_e$. (c) The graph shows as the mobility of the carriers decreases when the diameter of the NWs shrinks its size. (d) The graph shows as the carriers density increases when the diameter of the InAs-NWs decreases the size. The graphs (a),(b),(c) e (d) show results due to the effect of quantum confinement on the electric transport in the InAs-NWs. The figures a-b and c-d have been adapted from [8, 9], respectively.

3.2.1 NWs surface funzionalization

In order to achieve high transparency at the interface between the NW and a thin metallic layer, the oxidized surface of the NW needs to be cleaned. Few seconds of wet etching with buffered hydrofluoric acid is typically used to remove the oxides [14, 107]. Studies that show the possibility to use the argon milling process as oxide remove step have been reported in [31, 106, 108]. The sulphur surface passivation is the treatment that is commonly applied to funzionalize the surface of III-V semiconductors [28, 29]. The passivation process consists in the removal of native oxides, in the provide to implant bonded sulphur atoms and

in the prevent the oxide regrowth [109–111]. The passivation using ammonium polysulfide, $(NH_4)_2S_x$, water solution represents the technique chosen for these PhD works. The recipe of the chemical preparation is reported in A.

In order to define the etch deep in the NWs etch tests have been performed. Fixing the chemicals concentration (3M) and the water dilution a systematic approach on various chips has been used in order to define the etching rate of oxide. NWs covered by PMMA have been aligned with a electron beam lithography (EBL) session and only half has been passivated. The passivation tests have been performed fixing the temperature of the solution at 40 °C. In fig.3.5 a SEM micrograph of an etch test on the NWs is shown.

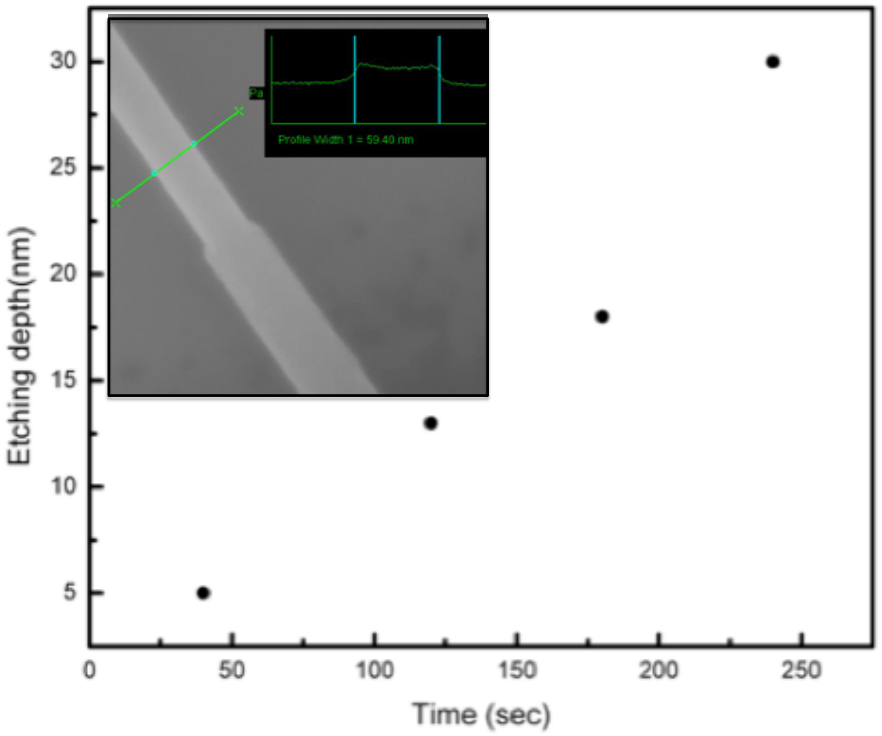

Figure 3.5: The results of etching deep as function of time of etching are shown in the graph. In order to remove only few nanometers of native oxide avoiding damages to the crystalline structure of NWs the passivation time has been fixed to 35sec. The inset a SEM micrograph shows the effect of passivation solution on the InAs-NWs.

3.2.2 Electrical properties at room temperature

The NWs transport parameters have been estimated using field effect measurements. In figure 3.6 a sketch of NWs connection is shown. When a voltage (V_{SD}) is applied to a side of NWs a current (I_{SD}) flows

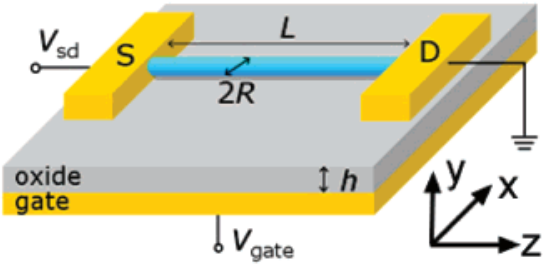

Figure 3.6: [10]

through it. A back gate voltage (V_g) changes the number of transport channels in the NWs modifying its resistance. The mobility of carriers of the NWs devices can be extracted from the measurements of transconductance $g_m = \frac{dI}{dV_g}$ [112, 113]. At low voltage biases (V_{SD}), the relation $g_m = \frac{\mu C}{L^2} V_{SD}$ governs transport in an ideal FET device [114, 115], where C and L represent the total gate-NWs capacitance and the channels length of the device, respectively. In typical back-gate NWs-FET geometries, an analytical formula derived from a metallic cylinder-plane system is routinely used for calculating the gate-NW capacitance $C/L = (2\pi\epsilon_0\epsilon_r)/[cosh^{-1}(R+h)/R]$ where h is the gate oxide thickness, R is the NW radius, and ϵ_0 and ϵ_r are the relative vacuum and dielectric constant of the oxide, respectively. When $h >> R$ the denominator can be simplified to ln(2h/R). By solving the set of coupled equations in 3.1 we get n, μ, τ of the NWs.

$$\begin{cases} \dfrac{I}{V} = \dfrac{e * S * n * \mu}{h} \\ g_m = \dfrac{C * V_{SD} * \mu}{L^2} \\ \mu = \dfrac{e * \tau}{m^*} \end{cases} \tag{3.1}$$

Taking in account the definition of $D = k_B * T * \mu$, that for 1-dimensional systems becomes $D = v_F * \ell$, coupling the relations of D with the values of μ and τ an esteem of ℓ is made.

n (10^{19} cm^{-3})	μ (cm^2/Vs)	ℓ (nm)	m^* (m_e)	L(μm)	d(nm)
1.8±0.8	300±100	20	0.023	2	90±10

Table 3.1: Summary of the extracted parameters for the strongly Se n-doped InAs-NWs

Chapter 4

Nanoprocessing

This chapter describes the nanofabrication techniques developed for the realization of superconducting hybrids junctions. Three different types of devices have been fabricated: non-suspended and suspended junctions between InAs-NWs and Aluminium and suspended junctions between InAs-NW and YBCO. After describing the developed to optimize the performances of the devices, I will discuss the techniques used to combine the semiconducting barrier nanowires with the superconductors.

4.1 Non-Suspended junctions: LTS/InAs-NWs/LTS

The InAs-Nws have been grown by Au-assisted chemical beam epiaxy (CBE) on InAs (111)B substrates. From the growth substrate the InAs-NWs are transferred on Si^+ substrate capped by 280nm of thin dry SiO_2 layer. On the substrate sub-millimetric electrodes and bonding pads have been patterned through standard an ultraviolet lithography (UVL) processing (see the figures on the left hand side 4.2 and 4.3). A layer of Ti/Au (10nm/100nm) has been thermally evaporated and defined by a lift off process (see the fabrication recipe in AppendixB). Subsequently, fine marks have been defined by first EBL step and Ti/Au (10nm/60nm) thermally evaporated. Their quality (uniformity of its edges) defines the misalignment of the metallic contacts on the NWs, thus the success of the superconductive junctions. The relative position

of the NWs is defined with respect to pre-evaporated marks and located through SEM images. Fingers and connections strips of the NWs have been drawn and exposed by close-source software Elphy Plus & Multibeam Raith-GmbH. Development, oxygen ashing of e-resist and passivation procedure (see AppendixA) are followed by the deposition of Ti/Au (12nm/120nm) contacts of width and length of 300nm and 1, respectively. Electrical tests have confirmed that the quality of the contacts between the NW and the metallic fingers significantly improves when the thickness of Ti changes from 0nm to 12nm (see the graph 4.1). For this reason the thickness of Ti interlayer, typically used to create ohmic contacts on the NWs [14, 31, 33, 116], has been fixed to 12nm for all superconducting junctions.

Junctions of length from 110nm to 230nm have been yielded by multi-

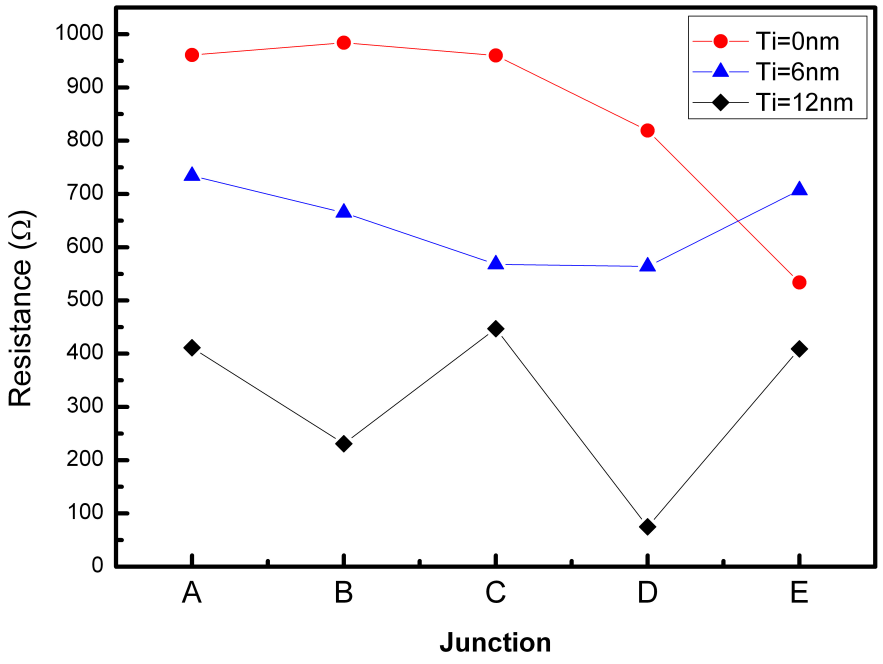

Figure 4.1: The graph shows that an increment of the thickness of Ti interlayer yields a decrease of the junction resistance.

contact geometries builded on the same NWs (see fig.4.2). This design is useful for studying the normal transport properties and their variability along the axis of the NWs.

In order to prevent the degradation of interface NWs - metallic contacts the junctions are stored in vacuum before their electrical measurements in temperature.

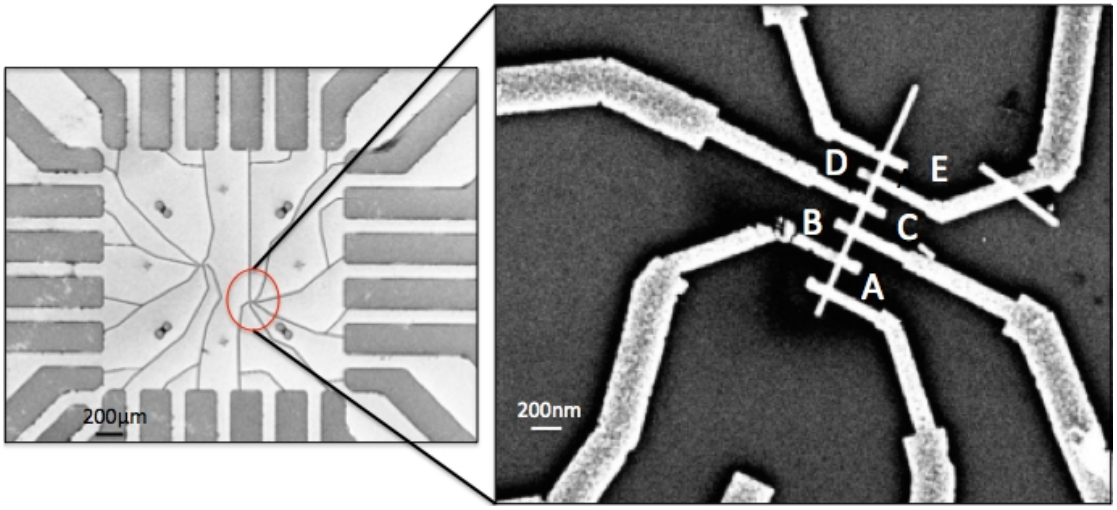

Figure 4.2: The SEM image on the left hand side shows the results of a step of UV lithography (UVL) (micrometric fingers and bonding pads) and sub-micrometric Ti/Al (12nm/120nm) stripes connected to the InAs-NWs fabricated through a electron beam lithography (EBL). The image on the right hand side shows five junctions {A,B,C,D,E with different barrier length {230,200,170,140,110}nm, respectively. These junctions obviously use the same NW as a barrier.

4.2 Suspended junctions: LTS/InAs-NWs/LTS

The realization of the layout with suspended nanowires has been much more challenging and has required both top-down and bottom-up approaches. The fine positioning of the NWs has represented another fabrication obstacle that we have solved (see 4.4.3). Two procedures have been developed for the fabrication of the GAP (inter-electrods spacing) and both require lift-off steps. An approach consists into the exposure of both the arms of the junction in the same EBL session. This method allows to fabricate arms not closer than 100nm. This limit is imposed by the e-resist proximity effect. This fabrication recipe is reported in AppendixC.

A second more sophisticated method requires many fabrication steps. An EBL session is useful to exposure chip marks and one of two facing arms for building the GAP. These structures are defined by Ti/Au (10nm/100nm) thermally evaporated. A second EBL step used the pre-evaporated marks for defining the second arm of the support device. This approach yields GAPs shorter than 100nm because reduces the limitations due to the proximity effect of the e-resists. This method

has also used for the realization of nanoGAPs in HTS materials. For these compounds several fabrication steps are required since the union of top-down and bottom-up techniques are essential for miniaturizing that type of materials [87, 88, 90].

The fig.4.3 - B shows a GAP built by Ti/Au facing electrodes readies for the deposition of the InAs-NWs. Details of InAs-NWs deposition techniques developed are reported in the section 4.4. With help of SEM images the position of the NWs relative to predefined Ti/Au marks has been located. Electric contacts of Ti/Al (12nm/120nm) on the NWs are defined by a last EBL step (see the fig.4.3). The fabrication steps

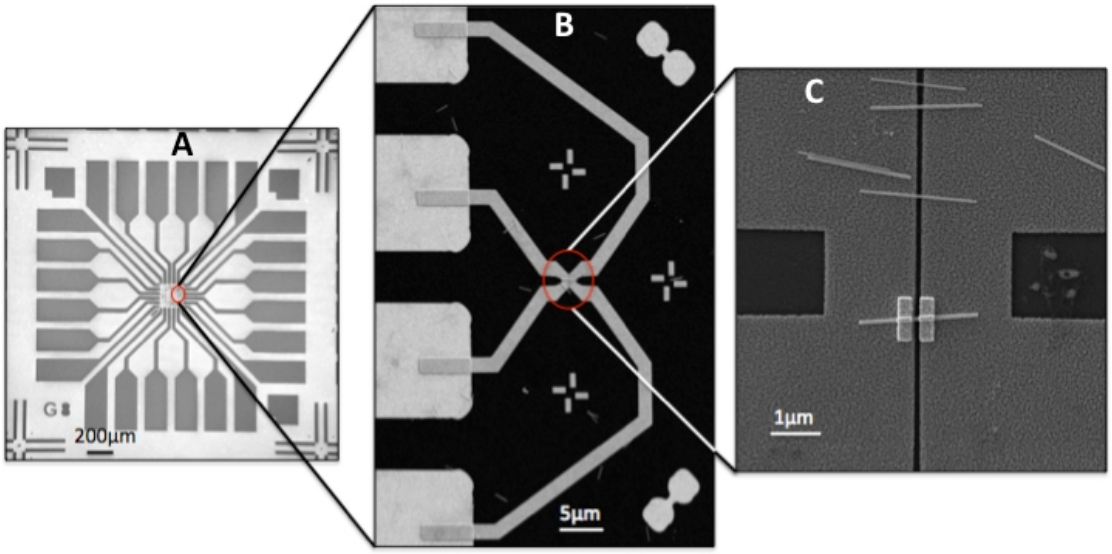

Figure 4.3: SEM micrographs show: - A - the result of a UV lithography (UVL) step (bonding pads and connection stripes); - B - Ti/Au (10nm/60nm) arms aligned to the UVL stripes; - C - InAs-NWs have been positioned by DEP (4.4.3) and contacted by a last EBL step.

developed for building superconducting suspended junctions between InAs-NWs and Aluminium are summarized in fig.4.4.

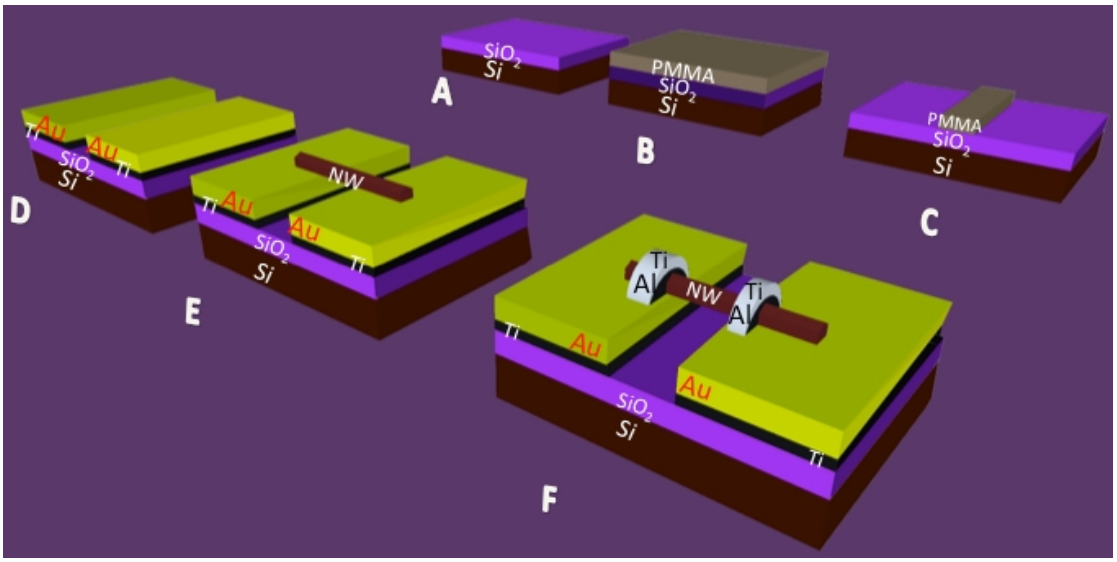

Figure 4.4: Nanofabrication steps useful for building superconducting suspended hybrid channel-devices between InAs-NWs and Aluminium. - A - the support chip device of Si/SiO_2; - B - spin coat of PMMA AR.P-679-04; - C - PMMA developed; - D - Ti/Au (10nm/60nm) thermally evaporated: the GAP is defined ; - E - InAs-NWs drop casted and aligned by DEP (see subsection4.4.3) onto GAP; - F - Ti/Al (12nm/120nm) metallization of the InAs-NWs right after the passivation step. The lift-off procedure in hot acetone defines the device.

4.3 YBCO - InAs-NW - YBCO junctions

To fabricate nanostructures with HTS preserving its pristine properties has been an extremely challenging, high risk but very rewarding activity that has allowed to discovery novel aspects of physics related to these exotic materials. The most used HTS is represented by YBCO and in the last decades several methods have been used to miniaturize HTS (see section 2.3). Efforts connected to the growth of YBCO, the deposition and cleaning of the InAs-NWs have yielded to the development of several design of the devices (see fig.4.6). The limitations of each design have unveiled properties useful to improve a new version. The α version is shown in fig.4.5: an array of 14×14 squares spaced each other 100nm covers a surface of 80μm^2 about. This design does not allow the deterministic positioning of InAs-NWs; for this reason the nanowires have been random dispersed using the technique explained in the subsection 4.4.1. The β version shows problems connected to peeling of gold. This happens when the InAs-NWs are deposited on

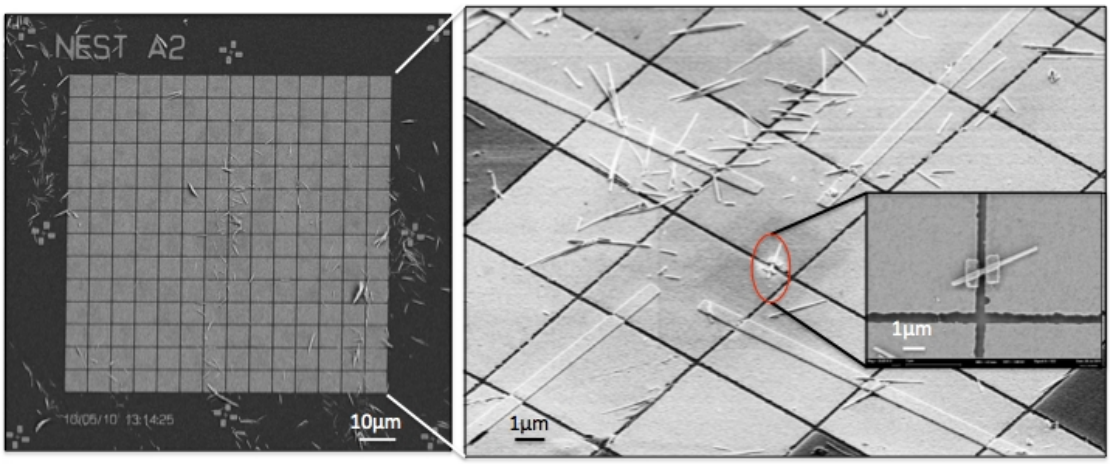

Figure 4.5: In figure on the left hand side the α version of the device composed by an array of 14×14 squares (5×5 μm^2 each one) spaced $\sim$ 100nm that covers a surface of 80μm^2 is shown. In the image on the right hand side InAs-NWs have been dispersed onto GAPs. One EBL and thermal evaporation session define the metallic contacts at the edge of the NWS. The micrograph SEM in the inset shows a junction between semiconducting InAs-NWs and YBCO.

the YBCO chip-device using the technique "pick and place" (see subsection 4.4.1); a friction force between the tissue and the surface of the chip device damages the Au protective layer of YBCO. The δ version allows to get GAP shorter that 100nm but we have verified that its shape does help for the fine positioning of the NWs. The γ version has been developed for getting narrower GAP and to better control the positioning of the NWs. It shows unexpected limitations due to the InAs-NWs positioning: we have observed that the deposition of the NWs systematically occur on the connections stripes and have never been achieved a their positioning on the GAP between the two facing tips. The ϵ version shows narrower GAP and connection leads. The reduced sizes of the connection stripes could involve normal domains in the HTS compromising the detection of the superconducting properties of the InAs-NWs / HTS junctions. For these reasons the development of a new design has been needed. Taking in account the results of the NWs deposition obtained in β, γ, δ and ϵ designs, it has been possible to implement the ζ version that allows to get narrowest GAP and uses an innovative deposition technique (see subsection 4.4.3).

The ability to electrically connect HTS with InAs-NWs is the evidence that several technological issues have been solved and represents

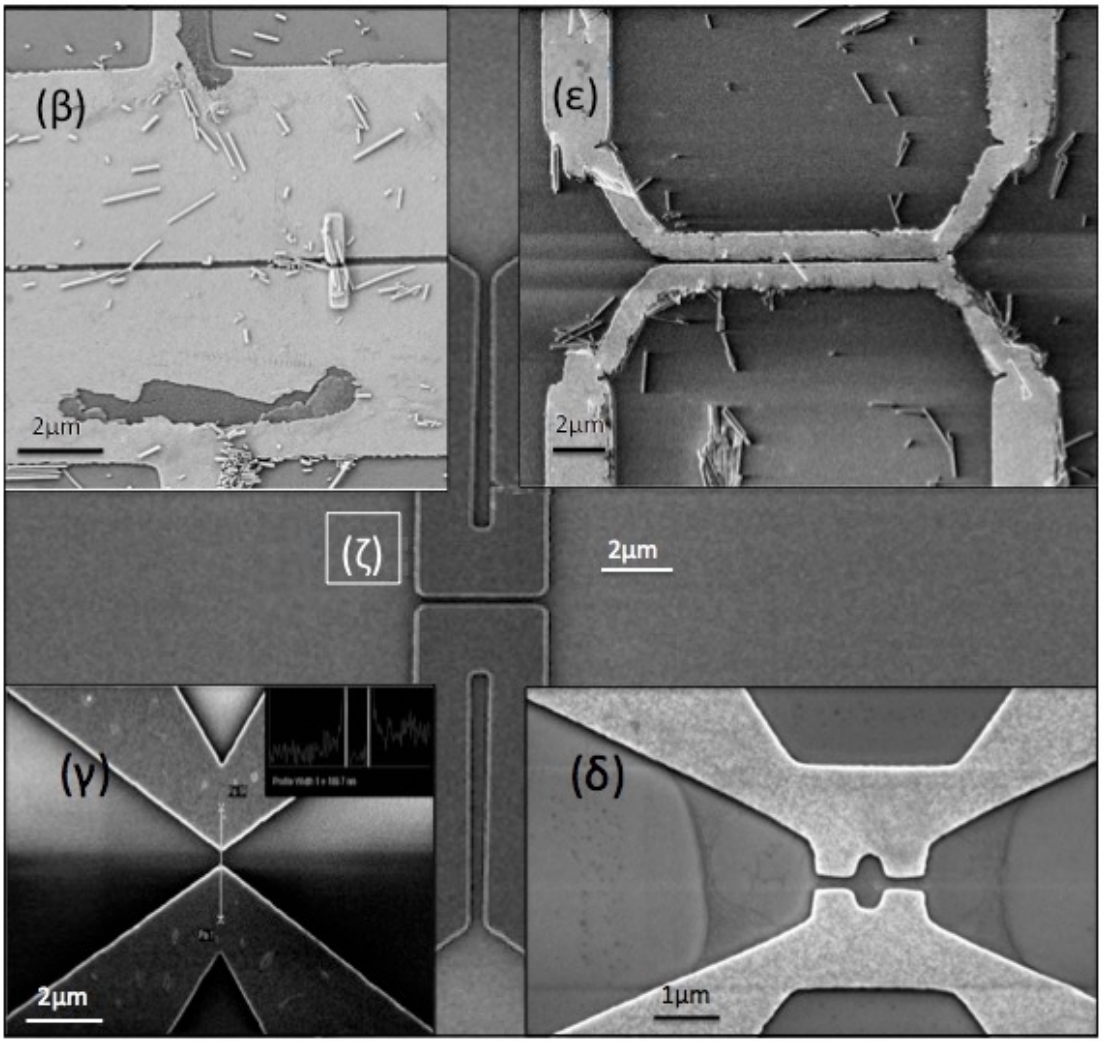

Figure 4.6: Designs developed for building superconducting hybrid junctions between HTS and InAs-NWs. The best design, ζ, allows to build this innovative type of superconducting hybrid junctions between InAs-NWs and YBCO.

the basis for further advances. An aspect of originality of the developed design consists of InAs-NWs suspended on the HTS electrodes with Ti/Au contacts encapsulating the InAs-NWs edges. A sketch of the main fabrication steps is shown in fig.4.12. For this type of junctions the HTS materials work as both NWs mechanical support and Cooper pairs charge reservoirs. Many fabrication steps for building suspended design devices with HTS and InAs-NWs have been optimized taking advantage of the fabrication recipe developed for the suspended junctions between InAs-NWs and LTC (see fig.4.2) and has also been benefited of a consolidated experience on realizing HTS nanostructures [88, 91, 92, 117–132]. In order to reduce the damages on the YBCO,

preserving its superconducting pristine properties, a specific nanofabrication recipe has been developed. This funds on reduced number of e-resist bakes ($60\,^{\circ}\mathrm{C}$ for 5 minutes; parameters are completely outside the manufacturer's specifications but allow to preserve the properties of the YBCO), dry Ar^{+} milling etching performed at low temperature (the YBCO substrate is kept at 120K in order to reduce oxygen loss of the YBCO unite cell during the Argon atoms bombardment) and wet etching few second long in acid solutions (for instance, Ti hard mask useful for defining the GAP has been removed using 18 seconds long acid attack in HF 1:20 solution) have been accomplished.
The devices have been built on c-axes YBCO 50nm thick grown by laser ablation (PLD) on yttria-stabilized zirconia (YSZ) substrate and capped by Au 20nm thick. The HTS materials have been fabricated by CERACO $http://www.ceraco.de/$ **&** **THEVA** $http://theva.com/company/press/$ **GmbH companies.**
The developed design allows to create GAP of size of 200nm in a very reproducible way without degrading the properties of YBCO; b) a InAs-NW can be in situ polished through a passivation etching without significantly damaging the superconducting YBCO thin film, always protected by a thin Au layer in all fabrication steps; c) sub-micrometers rectangular areas can be patterned on InAs-NWs suspended on YBCO banks, thus defining the areas for contacts. Progress on NWs positioning has been also made as discussed in 4.4.
The same c-axis YBCO sample have been employed to fabricate pure YBCO-NWs used as reference devices. The nanofabrication procedure adopted for the realization of YBCO-NWs is reported in the ref.[88].
The best design of the YBCO support device, shows in fig.4.7, have been obtained using the following e-beam-lithography (EBL) parameters: beam energy 20KeV; beam aperture 7.5μm**; beam current** $\approx 20pA$**; dose factor** $\approx 200\mu C/cm^2$ **and work distance 5mm. Two banks of size of** $(10 \times 1)\mu m^2$ **are facing each other at a variable distance. From each bank two larger leads depart for electrical connections. This configuration systematically allows to check if some unwanted shorts (more easily occurring when shrinking the trench size) are present before the NWs deposition as well as the superconducting properties of YBCO arms independently of the NWs.**

The key feature is the definition of the trench size between the elec-

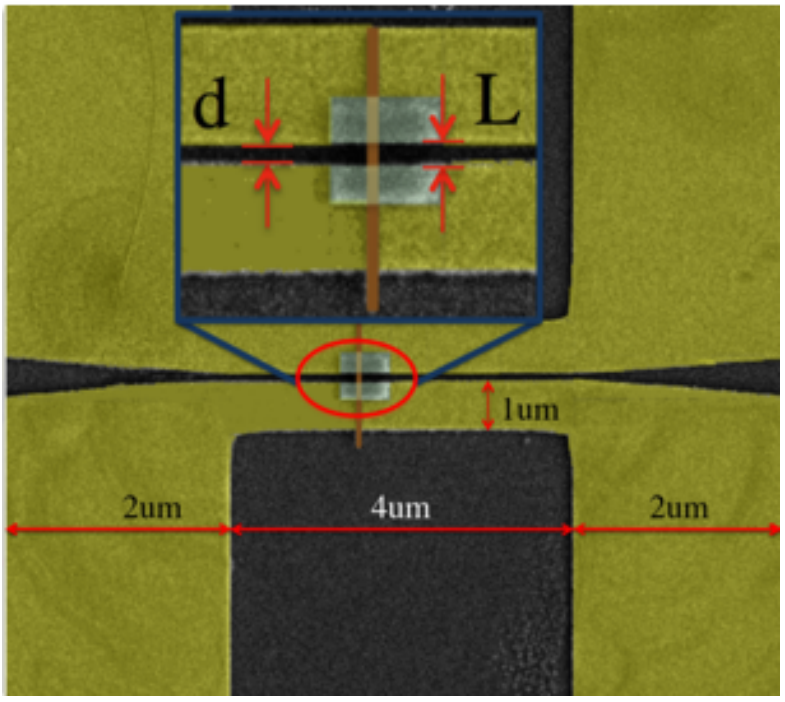

Figure 4.7: The image shows a YBCO/InAs-NW/YBCO junction in which the InAs nanowire appears as a thin brown filament on top of the trench in the YBCO layer of width d. The YBCO arms are $\sim 1\mu$m wide. The ohmic contacts between the NW and the SC arms are realized by evaporating two metallic Ti/Au areas (color gray) on the NW and distant between them (L) $\sim$ 200nm. The dimensions of metallic rectangles are $(300\times1000)\text{nm}^2$ each.The image in the inset shows a zoom of the metallic contacts on the InAs-NWS.

trodes, which is the main parameter that has been varied. For trenches larger than 200 nm, electrodes are never in short. On the contrary, when inter-electrode distance is further decreased, the design of the device and the EBL parameters need to be suitably modified. As a matter of fact, when two electrodes are facing each other at a distance smaller than 150nm, the e-beam exposure of one of the electrodes produces undesirable effects on the other ("proximity effect in e-beam lithography"). As a consequence, a set of nano-links in between the electrodes may be created. Currently for $160 < L < 180$ **nm the 40% of electrodes show a short. In the range** $120 < L < 160$ **nm the percentage of devices that show a short increases to 50%. For** $100 < L < 120$ **nm it becomes about 75%. Below** $L < 100$ **nm the 95% of electrodes are electrically linked. Data analysis has been accomplished taking in account two thousand trenches realized in 90** $(5 \times 5mm^2)$ **samples of YBCO/Au.**

To decrease the trench size below the 100 nm, other sophisticated EBL

techniques need to be developed, as for instance a double step of lithography. This technique has allowed the realization of a preliminary set of shorter trenches, thanks to the reduced e-beam proximity effect of the PMMA.

A Ti hard mask 40nm thick is evaporated then a cold Ar^+ milling is performed for cutting the layers of Au and YBCO, thus defining the shape of the device. Ar^+ milling doses have been calibrated in the fabrication of high quality YBCO NWs. YBCO NWs up to 50nm wide show higher critical temperature and huge values of critical current densities, thus suggesting low depression of YBCO surface properties [88, 92, 117].

Thickness measurements of YBCO/Au (see fig.4.10) followed by an electric check confirm that 21 minutes of Ar^+ milling (the etching has been accomplished with the following setting: pressure 1×10^{-4} Torr, beam voltage 315V and beam current 5mA) define the design of the device shown in fig.4.7. An oxygen plasma ashing at 10W, with a bias voltage of 100V for 5 minutes has always been performed before Ar^+ etching. Last step is fundamental since an growth of amorphous carbon dues to

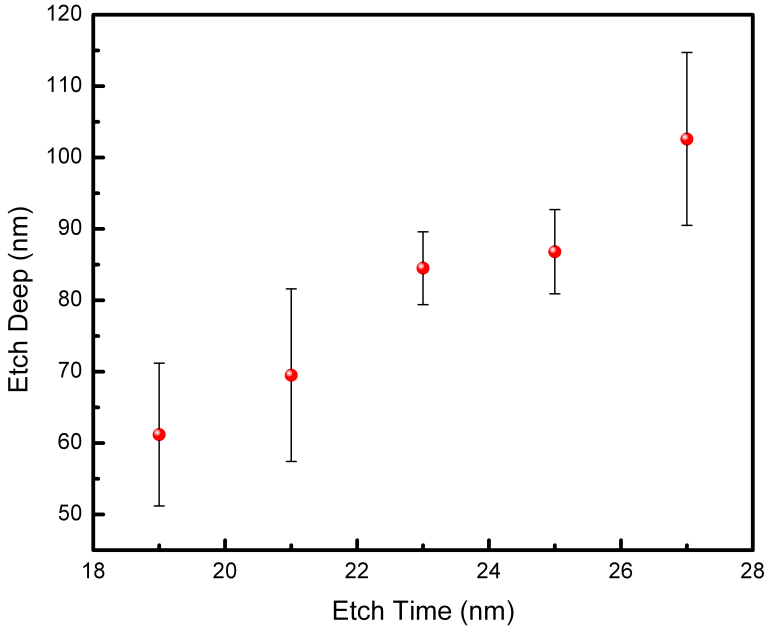

Figure 4.8: The graph shows the etch deep of the Au/YBCO sample as function of etch time. The data have been extracted from 52 devices. The statistical analysis concerning the etch deep after 21 minutes of Ar^+ milling has been performed on 28 devices. It yields the value (3.31 ± 0.17)nm/min as etch rate.

the SEM images session has been observed [133]. In addition, a carbon mask is used by research group [87, 92, 121] to replace the Ti hard mask

for miniaturizing samples of YBCO bulk. The results of carbon growth during the SEM session have been performed with the working distance at 5mm, beam aperture of 30 μm and EHT of 5 KeV. In fig.4.9 it is shown as a layer of carbon becomes thicker when increasing the SEM observation time (from 15 seconds for thinner layer to 90 seconds for thicker layer).

Ti hard mask thickness has been fixed to 40 nm since we have ob-

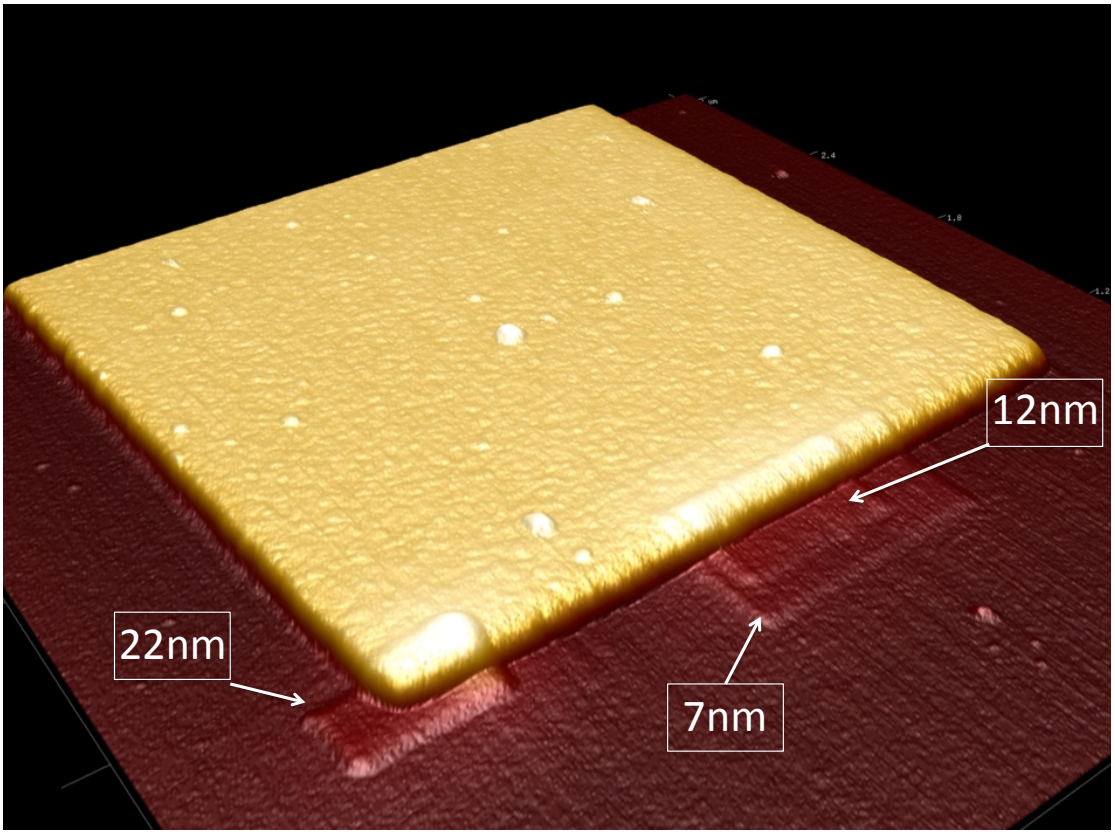

Figure 4.9: Atomic Force Microscope image shows three different thicknesses of the amorphous carbon due to SEM analysis. The rectangles of carbon 7nm, 12nm and 22nm thick are yielded by 15, 30 and 90 seconds of the SEM observation, respectively.

served that, on average, 21 minutes of Ar^+ milling (etching time useful for defining non-shorted GAPs in YBCO and Au 50nm and 20nm thick, respectively) etch 30nm of Ti. In the fig.4.10 the dependance of the Ti etch deep as function of the etch time is shown. The Ar^+ bombardment has an effect on the GAP width. It erodes materials from edges of facing arms, thus increasing the GAP size. In fig.4.11 the increment of the GAP size (ΔGAP) as a function of etching time is shown. After the Ar^+ milling step a gentle HF wet etching (diluted with DI water 1:20)

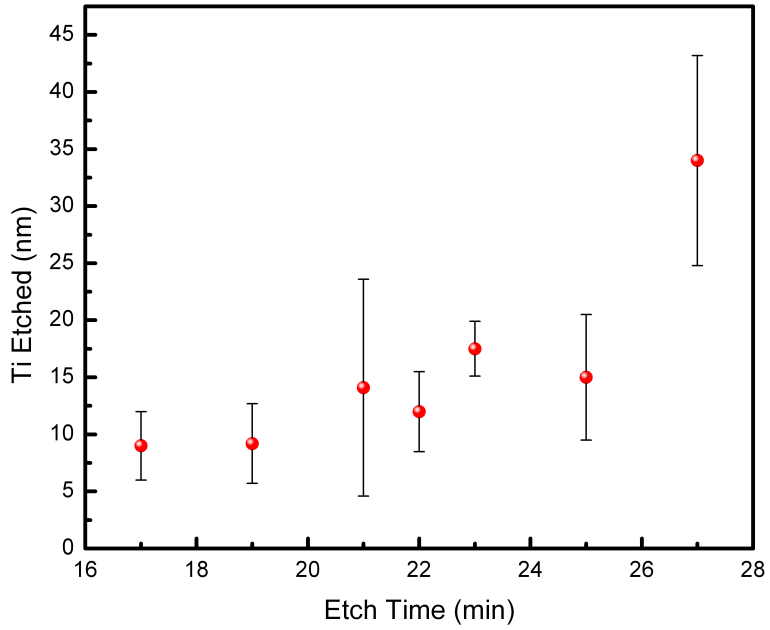

Figure 4.10: The graph shows the thickness of removed Ti as a function of the etching time. The statistical analysis has involved 88 devices. Ti etch rate is (0.78 ± 0.52)nm/min. Value estimated on 46 devices etched for 21 minutes.

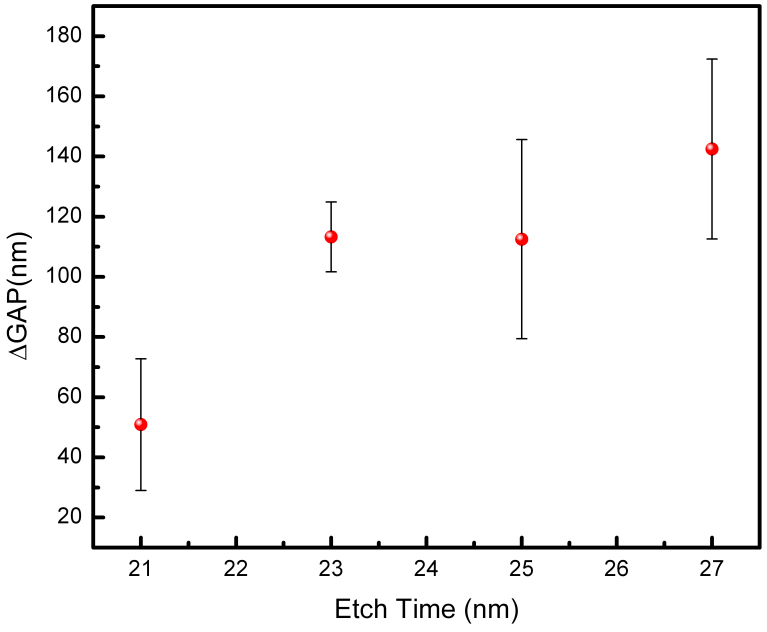

Figure 4.11: The graph shows the broadening of the GAP (ΔGAP) dues to effect of the Ar^+ bombardment. The value of ΔGAP is (2.4 ± 1.1)nm/min and is obtained after 21 minutes of etching.

18 seconds long is performed for removing the residual Ti layer. The trenches, right before the NWs deposition, are checked one by one by

Scanning Electron Microscopy and then by two points electric measurements, thus guaranteeing the absence of any possible shorts. Narrower and insulating GAPs "only" represent the starting point for the realization of superconducting hybrid devices with YBCO and semiconducting InAs-NWs.
Using the DEP technique (4.4.3) InAs-NWs are positioned on the shortest and insulating GAPs. The metallic contacts on the NWs have been exposed through a thin layer (∼2.5nm) of Ti thermally evaporated on PMMA AR.P 679.04 previously spin coated. The metallic layer avoids, during the EBL exposure, the electrons beam shift dues to the strong insulating properties of the YBCO substrate, creating, in the worst case, metallic contacts between the InAs-NWs and the side wall of the YBCO trenches. In addition, we have verified that partially immersing, in ammonium polysulfide for 35 seconds YBCO-NWs wide from 100nm to 2μm their superconducting properties are completely destroyed by passivation solution. For these reasons, as the fig.4.7 shows, the metallic contacts on the InAs-NWs have been builded slightly far (∼10nm for side) from the YBCO GAP edge and spaced L. Development of the PMMA, oxygen plasma ashing, passivation in ammonium polysulfide, thermal evaporation of Ti/Au-(12nm/120nm) and the lift-off in acetone represent the final steps to the superconducting hybrid junctions between semiconducting InAs-nanowire and YBCO.
In fig.4.12 a sketch of the fabrication steps developed for building junctions between YBCO and InAs-NWs is shown.
In order to fabricate this innovative superconducting hybrid junctions several details concerning YBCO and InAs-NWs have been taken care. The fabrication recipe that allows to build this innovative type of superconducting junctions is reported in the AppendixE.

4.4 Nanowires Positioning

In this work the devices have been fabricated using three main techniques for the InAs-NWs deposition. Two of them use dry and wet random positioning of the InAs-NWs. The last deposition method is represented by the wet random dispersion of the InAs-NWs finely

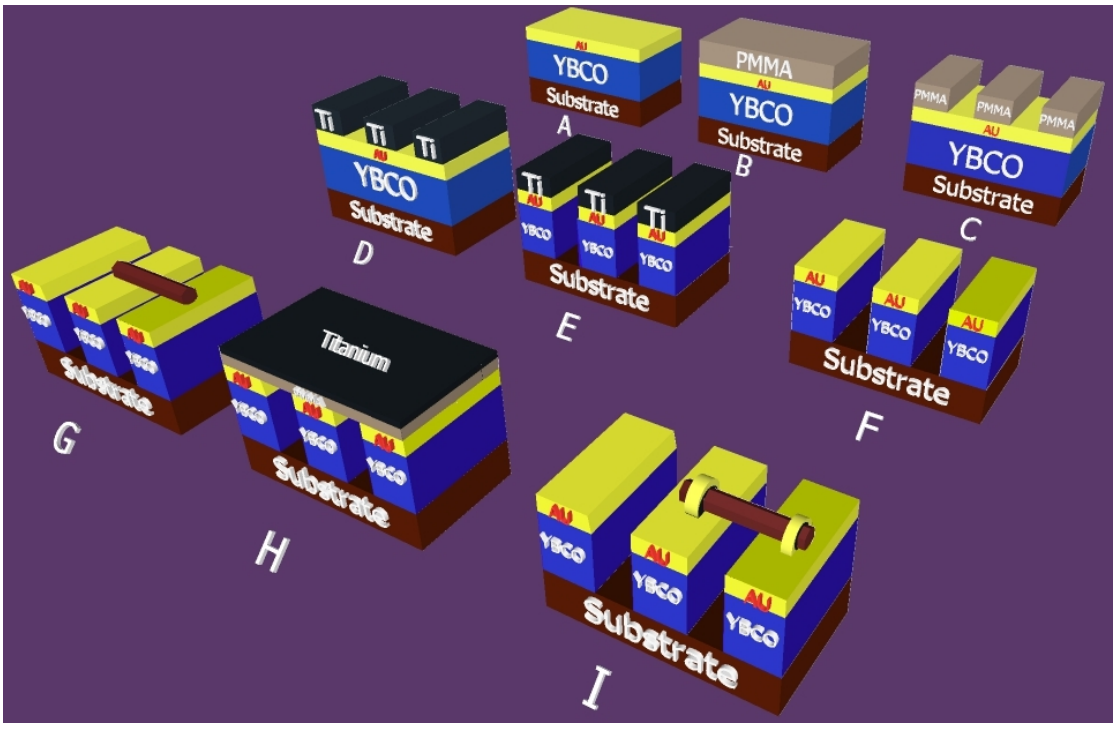

Figure 4.12: Fabrication steps. - A - YBCO sample capped by a thin protective Au layer; - B - spin coating of positive PMMA - type AR.P-679.04; - C - exposure and development of the PMMA; D - Ti hard mask thermally evaporated; - E - cool Ar^+ ion beam etching; - F - HF selective wet etching for Ti mask; - G - NWs positioning; - H - spin coating of PMMA AR.P-679.04 and the thermal evaporation of 2-3 nm of the Ti guarantee the absence of drift during the last EBL step dues to the charging effect of the insulating substrate; - I - result of a gentle Ti etching, PMMA development and thermal evaporation of Ti/Au on the InAs-NWs. The superconducting junction between InAs-NWs and YBCO is ready for the electrical characterization.

driven by dielectrophoretic force.
In the next subsections details on the techniques developed for the positioning of InAs-NWs will be reported.

4.4.1 Dry random dispersion

NWs are harvest by gentle rubbing a little piece of clean-room tissue, cut in the shape of triangle, against the growth substrate and are placed, by mild taps of the sharp triangle tip on the device substrate (this technique is also called "pick and place"). This method allows the positioning of NWs with an accuracy close to $50\mu m^2$ that depends on how well the profile of deposition field is defined (the deposition field of the device realized in this work has been define by an array of marks

or by micrometric connection stripes). This method has been used for the fabrication of the non-suspended junctions between InAs-NWs and Aluminum (see the section 4.2).

4.4.2 Wet random dispersion

This technique provides InAs-NWs in liquid solution. The IPA is a ordinary solvent used in the nanofabrication activities and is also compatible with the materials used for the fabrication of superconducting hybrid junctions builded in this work. Beforehand to disperse the NWs in solution the back side of the InAs-NWs growth substrate has been encapsulated with UV resist. This operation avoids the contamination of IPA solution with particles originate from the back of the growth substrate. Then a piece of few millimeters square of InAs-NWs growth substrate is placed in a vial with few milliliters of IPA. By low power sonication agitation 1 minute long the InAs-NWs are free to move in solution. The density of InAs-NWs in the liquid has been tested depositing 2 μl of solution on a clean Si/SiO_2 chip-test. The solution has been gentle blown with nitrogen gas and by optical microscope 10 NWs per 50μm^2 have been observed. This value strongly depends on the density of the InAs-NWs on the growth chip and on the volume of solution (NWs in IPA) used. This deposition method has been used for both non-suspended and suspended superconducting junctions.

4.4.3 Dielectrophoresis

Dielectrophoresis (DEP) is a well-known technique for the controlled deposition of nano- and micro-scale structures and exploits the forces exerted by an non-uniform electric field E on a dielectric particle due to its induced dipole moment p. In particular, when the size of the nano-/micro-structure can be neglected, one can expect a force and torque

given by the equations 4.1.

$$\begin{cases} \mathbf{F} = (\mathbf{p} \cdot \nabla)\mathbf{E} \\ \mathbf{T} = \mathbf{p} \times \mathbf{E} \end{cases} \tag{4.1}$$

The magnitude of the induced dipole p depends on the complex dielectric functions of the DEP liquid medium $\epsilon_m^*(\omega)$ and of the particle $\epsilon_p^*(\omega)$, where $\omega = 2\pi\nu$ (ν is the frequency of the AC electric field and $\epsilon^* = \epsilon - j\sigma/\omega$). The resulting force can be calculated in the case of a prolate ellipsoid and results to be proportional to the gradient of the electrostatic energy following the law $\mathbf{F} \propto \epsilon_m^* Re[K_\alpha(\omega)]\nabla\mathbf{E}^2$ where we introduced the Clausius-Massotti factors [134]

$$K_\alpha(\omega) = \frac{\epsilon_p^* - \epsilon_m^*}{A_\alpha(\epsilon_p^* - \epsilon_m^*) + \epsilon_m^*}, \qquad \alpha = L, S. \tag{4.2}$$

The form factors A_α depend on the eccentricity e of the ellipsoid and attain two different values when the field is oriented along the long (L) and short (S) axis. Our NWs have a length which is ≈ 20 times the diameter; we can thus estimate $e = \sqrt{1 - (1/20)^2} \approx 0.9987$, leading [134] to $A_L \approx 0.007$ and $A_S \approx 0.497$. The positive or negative sign of $Re[K_\alpha]$ determines whether the particle is attracted (positive DEP) or repelled (negative DEP) from regions with large E. Since our DEP protocol was performed using IPA alcohol ($\epsilon_m \approx 18$ and negligible conductivity $\sigma_m \approx 6\,\mu\mathrm{S/m}$) as the medium and highly-doped InAs NWs as the "particle" ($\epsilon_p \approx 10$ and sizable conductivity $\sigma_p \approx 10^5\,\mathrm{S/m}$), deposition is expected to work already at rather low frequencies [1]. Provided the correct DEP sign is achieved, the force in equation 4.1 will tend to attract the nanostructure to regions with a large electric field, the torque in equation 4.1 will tend, thanks to its easier polarizability along its axis, to align the NWs to the field lines. Usually, DEP is performed using electrodes separated by a gap of size comparable to that of the target nanostructures. In our case, we need to position the NWs on top of electrodes separated by a gap with a size d approx $100 - 200\,\mathrm{nm}$, thus $10 - 20$ times smaller than the NW length; this is an unusual configuration for DEP. One issues with such a small-gap geometry is that the

[1] Very low frequencies ($\nu \ll 1\,\mathrm{kHz}$), though, should still be avoided since DEP is expected to be less effective in this regime [134–136].

field E in the gap can become very strong even for relatively moderate excitation voltages (∼1V/100nm), with a significant risk of destructive electrostatic discharges (e.g. electrical breakdown of air is of the order of $\sim MV/m$ thus of same order of the electric field generated in the GAP). In fig.4.13 effects of voltage amplitude lightly higher than 1V applied to the GAP-device are shown.

This poses stricter limitations to the highest voltage that can be safely

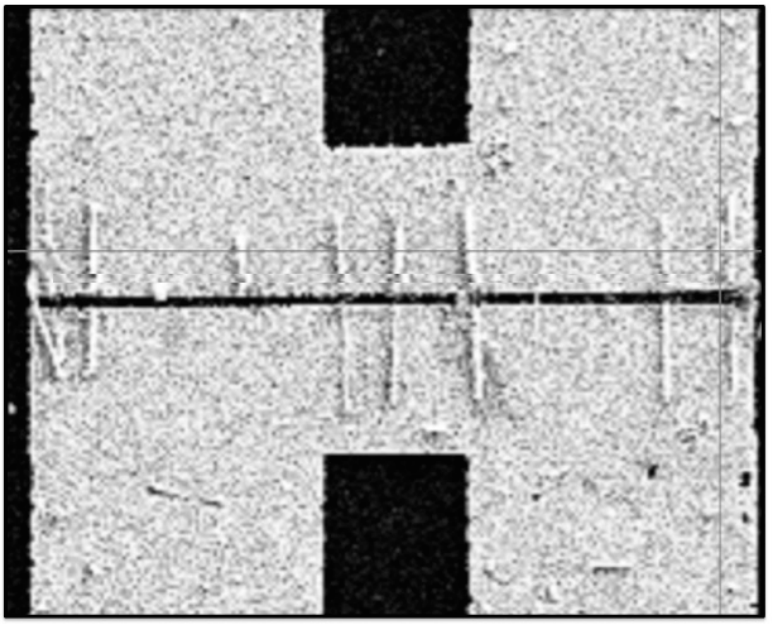

Figure 4.13: SEM micrographs shows several InAs-NWs aligned by DEP technique on the metallic banks. Voltage lightly higher than the optimal values yields strong electric fields in the GAP area that completely burn the NWs.

applied to the electrodes and, in turn, reduce the size of the region where DEP forces are able to overcome the effect of Brownian motion and random liquid convection and thus to capture the NWs. In addition, for small structures, trapping forces converging to the gap occur in a region which can easily be even smaller than the NW size and rapidly decay in the surrounding volume; therefore they are not very effective in trapping the nanostructure. These issues motivate us to develop a new DEP electrode designs. In order to obtain a four-wire contact geometries, we always designed two facing electrodes. In figure 4.14 two designs of several developed for the InAs-NWs deposition by DEP are shown. SEM micrograph (a) shows a geometry that despite generates huge electric field in the GAP area does not allow to pick and place

NWs exactly on the GAP. We have observed that InAs-NWs are positioned perpendicularly to the side of the tips. These results have been attributed to the shape and the dimension of the device developed. To

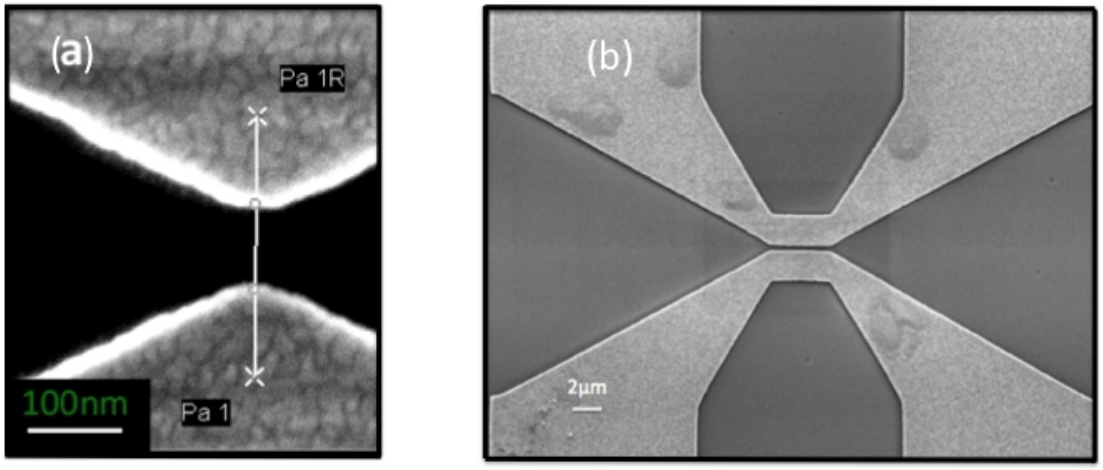

Figure 4.14: SEM micrographs of two GAP-designs are shown. The image (a) represents a GAP-device created by two tips facing. Applying a voltage at arms the higher electric field is yielded in between the GAP but we have verified that several NWs are driven and positioned perpendicular to the leads and no NWs on the GAP between two tips. The image (b) shows the best geometry developed that allows to pick, drive and place the InAs-NWs on the GAP.

study the evolution of the NWs deposition for these failed designs has allowed us to improve and develop the best shape for the DEP-device. The image 4.6-(b) shows the best design developed for the NWs positioning by DEP. We note that for each design of the device large surface coverage so that a sizeable E field could be induced over a significant volume and leads to a larger capture cross-section. The fabrication of the best DEP design device has been confirmed by numerical simulations of the induced DEP field for structure of various dimensions. In Fig. 4.15 we compare predictions [2] for a standard case of two $1\,\mu$m-wide fingers separated by a thin gap of $200\,$nm (panel a) and for a $2\,\mu$m-long gap geometry (panel a), which reproduce the experimental configuration of Fig. 1e. In both cases we plot the modulus of the gradient of the electrostatic energy density for a biasing voltage of ± 1V at the two electrodes and using $\epsilon_m = 18.23$ for the isopropyl alcohol. A $2\,\mu$m-long NW was added as a length reference. The comparison indicates that the second geometry is more effective in capturing the NWs and orienting them in the planned direction, for a given electrode bias since

[2] Calculations were performed with the PDE solver COMSOL Multiphysics 3.5a.

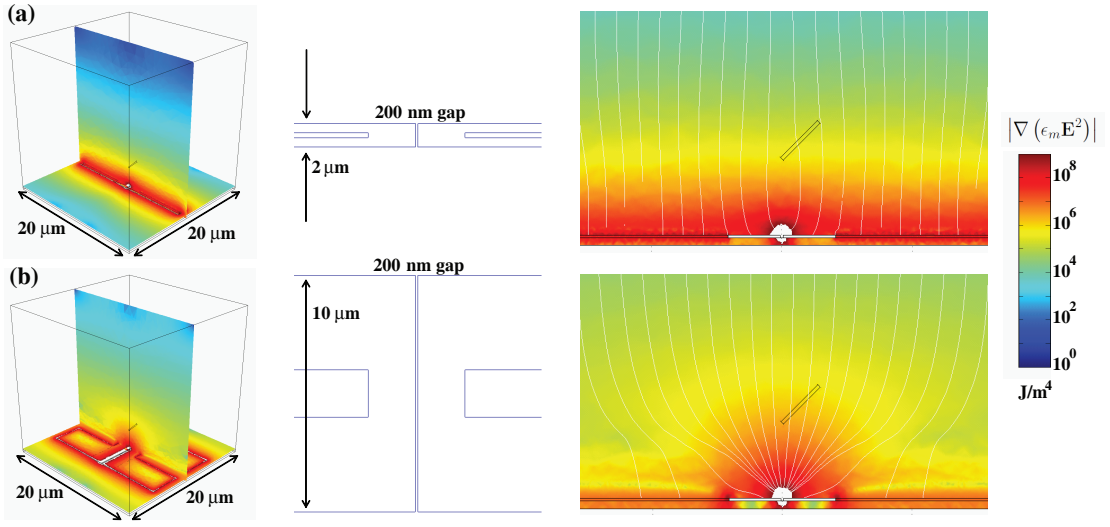

Figure 4.15: Numerical simulations for the gradient of the electrostatic energy density $|\nabla\epsilon\mathbf{E}^2/2|$ for two different electrode configurations. Panel (a) refers to a double finger architecture with a lateral size of 1 μm and a gap of 200 nm. Panel (b) refers to the geometry shown in Fig.1. In both cases a ± 1 V bias was applied to the two electrodes and using $\epsilon_m = 18.23$ for the isopropyl alcohol. On the right had side white lines indicate the direction of the gradient and highlight the more efficient trapping of the geometry in panel (b). It is important to note that the field line density in the right panels does *not* have any direct correspondence with $|\mathbf{E}|$ since the field configuration is three-dimensional and has a strong dependence on the out-of-plane direction, particularly in thin-finger the case (a). A 2 μm long cylinder was added as a reference at about 3 μm from the electrodes.

DEP forces extend further away from the gap with respect to the case of panel (a). This is even more evident looking at the white lines on the right hand side plots, which indicate the direction of the DEP action: in our DEP geometry attractive forces converge to the gap over a a quite large volume; differently, as anticipated, a much poorer capture efficiency can be expected in the more standard geometry of panel (a). Experimentally, our DEP process was achieved as follows. InAs NWs were dispersed in isopropanol by sonication of the growth substrate. The deposition was then achieved by putting a drop (2 μl) of the solution on the substrate and, at the same time, by applying an AC voltage to the Ti/Au electrodes, as indicated in the overlay in fig. 4.16. Since we use a very small inter-electrode gap, the substrate is largely screened; as a consequence, it is not expected to have an important effect and can be left floating [134]. Optimal results were obtained by applying an AC voltage in the range $0.75 - 1.20$ V and a frequency of $1 - 10$ kHz, while

frequencies $\nu \lesssim 100\,\mathrm{Hz}$ were found to be less effective [134–136]. The AC field was applied until the isopropanol completely dried up. These values gave a good deposition yield, without the accumulation of NW clusters. In fig.4.16 in (a) the sketch of DEP technique and in (b) a InAs-NWs/ Al junction (the NW has been aligned by DEP) are shown.

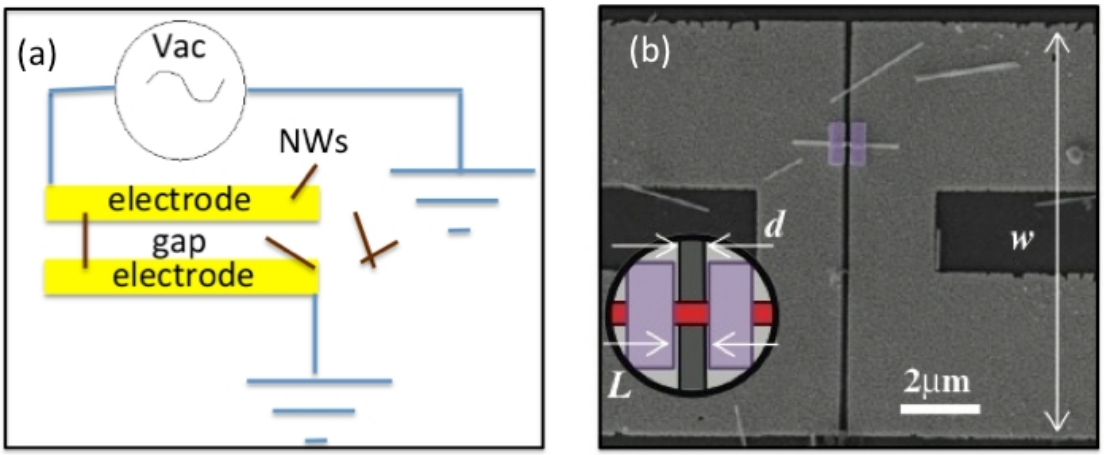

Figure 4.16: The figure shows: (a) the sketch of the DEP technique: an arm is applied the ac voltage and the rest of the device is place at ground potential. $2\mu\ell$ of InAs-NWs dispersed in solution are drop-casted on the chip then the a.c. voltage ($\sim 1V$ @10kHz) is applied. As result, the NWs (brown objects) are aligned to the electrodes of the device; - (b) SEM micrograph of InAs-NWs/Al junction. Two Ti/Al (12nm/120nm) contacts (colour violet) are thermal evaporated on the InAs-NWs positioned on the GAP by DEP. The width of GAP is (d∼130nm) and the metallic contacts on the NWs are spaced $L \sim 150nm$ apart.

Chapter 5

Cryogenic systems and measurements setup

In this chapter we will describe the main refrigerator system used for the measurements at low temperatures and the electric set-up employed to perform the characterization of the superconducting hybrid junctions. Junctions between InAs-NWs and superconductors (LTS and HTS) and devices in which the transport channels have made by a flake of graphene/graphite positioned in suspension on YBCO trenches, have also been characterized at very low temperature.

5.1 Cryogenic ^{3}He system

The measurements at low temperatures have been performed using two type of cryogenic systems that allow to reach the base temperatures of 300mK and 20mK, respectively.
All the electrical characterisation of InAs-NWs/YBCO junctions have been accomplished using the cryostat Oxford Instruments Heliox that taking advantage of ^{3}He technique of refrigeration allowing to reach the temperature of 250mK. The system is immersed in a helium (^{4}He) thermal bath at temperature of 4.2K and the chip-device, electrically connected to the cryostat, is thermally decoupled to the ^{4}He bath through a vacuum chamber, called inner vacuum chamber (IVC), thus allowing

to set temperature of the device from 250 mK up to 90K. A sketch of the system is shown in fig.5.1. The chip holder, on which the sample is connected, is thermally anchored to the ^{3}He pot stage. The sample, during the electrical characterization in temperature, is kept in vacuum at pressure of 10^{-2} mbar. As the fig.5.1-b&c show, a capillary draws ^{4}He from the bath to the 1K pot pumped for reaching the temperature below 2K. Pumping on the 1K-pot is regulated by a needle valve. A this temperature, the ^{3}He gas, that is contained in close tank, starts to condense. The 300mK base temperature is reached by pumping on the ^{3}He by a molecular pump (sorption pump), which consists of a large amount of zeolite, enclosed in a small cylinder inside the cryostat, actives below 30K. When the sorption is at a temperatures lower than 30 K, the vapours of ^{3}He are adsorbed, thus the base temperature is reached. An heating system regulates the switch on/off of the sorption pump stage.
The steps that allow to reach the base temperature are:

1. **dip the cryostat in the ^{4}He bath and reach the temperature 5K about of ^{3}He stage;**

2. **set the needle valve in order to have the temperature close to 2K of the ^{3}He stage;**

3. **heating up the sorption stage at the temperature close to 35K and keep for 30min (needs to be close the 2K till the complete condensation of ^{3}He that brings at 250mK the ^{3}He-stage);**

4. **cooling down the sorption monitoring the 1K pot temperature;**

5. **the sample will reach the temperature of 250 mK that can be kept several hours.**

The system allows the electrical characterization with high thermal stability in the range of temperature [0.25; 90]K.

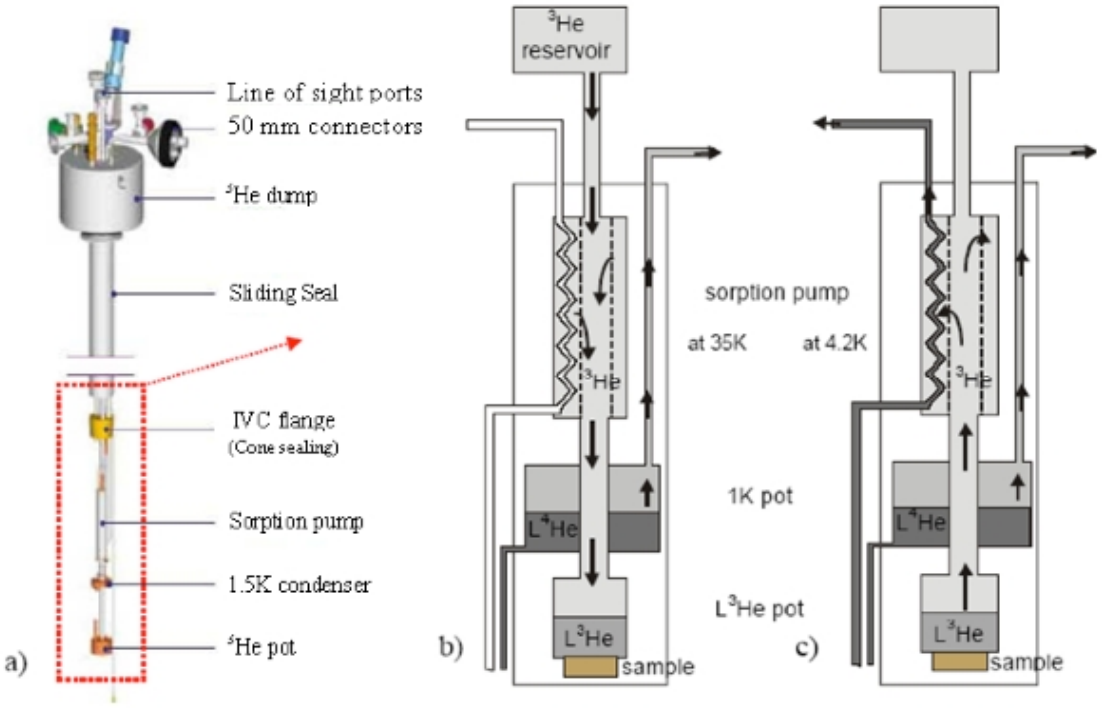

Figure 5.1: In figure a) the main components of the Oxford Instruments Heliox are shown; in fig. b) the condensation process of ^{3}He, that allows to reach the temperature of 250mK, is shown; the sketch c) shows the process of heating up of the cryostat.

5.1.1 Filters, lines and shields

The electrical characterization of the junctions has been performed in cryogenic system equipped with an electronic that performs high ratio signal/noise measurements including filtering stages at low temperatures (see fig.5.2). To decrease the noise coupled between the device and the external environment, each line is connected to a stage of low pass filters (cut off frequency of $\sim 2MHz$) and two stages of copper powder filters (CPF) at low temperatures. The CPF cut out the signals at high frequency ($\sim 1GHz$). In fig.5.2 the three stage of filters are shown.

The electric setup of measurements is connected to the devices through electric lines made with manganin (Cu-Mn-Ni alloy with low heat capacity) from external environment to the 1K pot stage and from 1K pot to the ^{3}He stage are made of Nb/Ti alloy (superconducting materials that allows high current flows). In order to reduce electromagnetic noise the connection lines are twisted in pair. The system is also provided with handmade high gain amplifier and shields from external magnetic

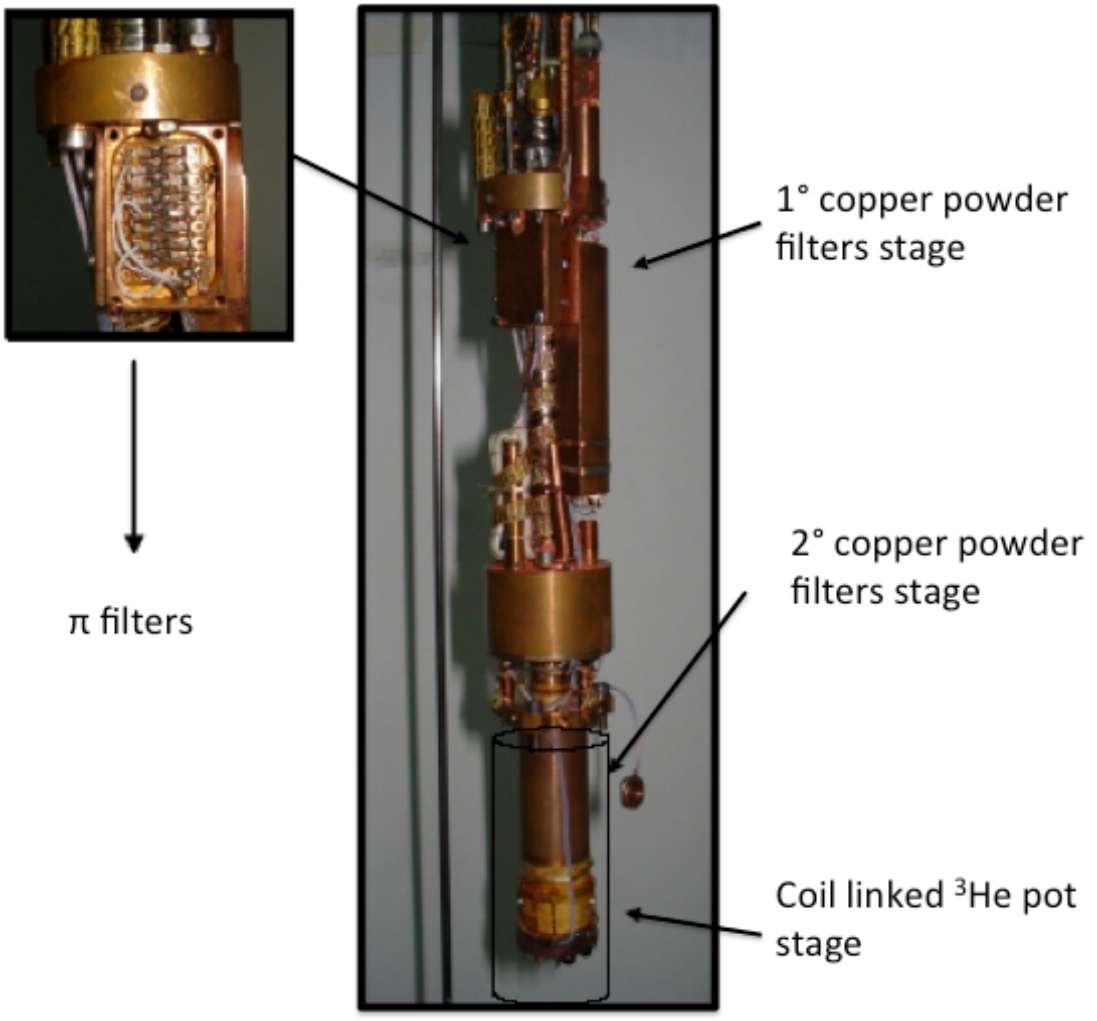

Figure 5.2: In the figure three stage of filters are shown: Low pass stage (π filter with cut off frequency close to 2MHz) and two stages of copper powder filters that cut-out signals about GHz frequencies.

fields. It is also equipped with a NbTi superconducting coil to apply an external magnetic field to the system, up to 300 mK, and with a microwave line allowing to irradiate the device via RF signals emitted by a linear antenna.

5.2 Dilution Refrigerators

Non-suspended hybrid junctions have also been characterized at very low temperature (∼10 mK) in the Dr. Francesco Giazotto Lab (NEST Laboratory, Scuola Normale di Pisa) using the Triton 200 Cryogen-free dilution refrigerator made by Oxford Instruments (`http://www.`

oxford-instruments.com/products/cryogenic-environments/dilution-refrigerator/cryogen-free-dilution-refrigerators/cryogen-free-dilution-refrigerator). The devices have been biassed in current and the voltage signal was amplified and read by a multimeter.
The first superconducting hybrid junctions made between a flake of Graphene/Graphite that works as suspended channels transport placed on the support YBCO trenches were characterized in the Prof. Francesco Tafuri Lab (Seconda Universitá degli Studi di Napoli/Dipartimento Ingnereria Industriale e dell'Informazione) using the Kelvinox MX400 made by Oxford Instruments (http://www.oxford-instruments.com/products/cryogenic-environments/dilution-refrigerator/wet-dilution-refrigerators/dilution-refrigerator-kelvinox400ha). This refrigerator is shielded against external magnetic field and radiofrequency noise. Filters systems installed and thermally anchored at different stages of the dilution unit, wiring from room temperature stage are twisted pairs and shielded by a tube mades of a metallic alloy, allow to perform high quality low noise measurements at very low temperatures (∼10 mK).

5.3 Measurement set-up

The measurements have been performed in four probe contacts configuration. The superconducting junctions have been biassed in current. A limitation resistor (R_L) which can be selected in the range [1-100M]Ω is in series to the waveforms generator. The current injected in the device depends on R_L. The voltage across the device is measured by a battery-powered differential amplifier. The excitation and voltage curves are read by an oscilloscope. In order to increase the sensitivity of the measure, the current-voltage characteristics are mediated at least on 100 sweeps. This allows to get an error in the critical current $\sim 3nA$ (it has been defined as the maximum error at a fixed value of voltage). Resistance-temperature measurements have been performed with low frequency (11Hz) bias current of 5nA, lower than the critical current of the device, and the voltage across the junctions has been amplified by battery-powered differential amplifier and read by a lock-in. This setup allows to get for the measurements of resistance an percentage

error $\sim 1\%$. This has been evaluated as the ratio between the maximum error in resistance and the average resistance: it represents the worst error values in the measurements of resistance.
The data have been stored through a LabVIEW program. In fig.5.3 a sketch of the set-up used for the electrical characterization of the superconducting junctions is shown.

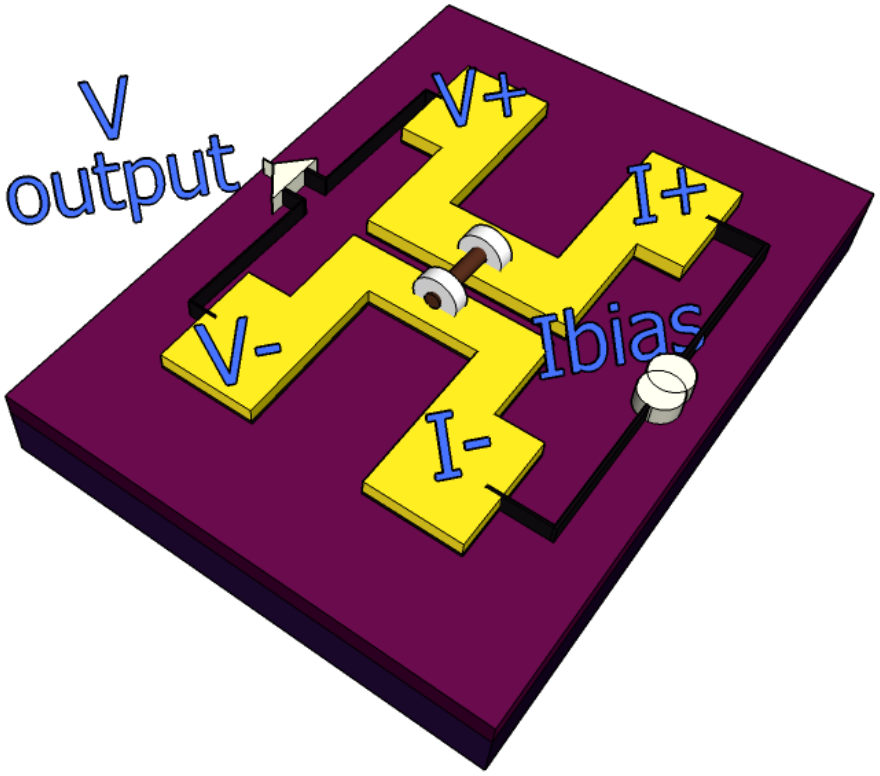

Figure 5.3: Schematic drawing of the measurement set-up used for the electrical characterization of the superconducting hybrids junctions is shown. The device is biassed in current I_{bias} and the voltage that drops across the device is amplified by a differential amplifier, thus is ready to be read by a lock-in or a multimeter and saved on PC.

Chapter 6

Transport measurements Al - InAs-NWs - Al

In this chapter we will present and discuss the experimental results obtained for the Non-Suspended and Suspended superconducting junctions build between Aluminium and InAs-NWs introduced in the chapter 4. We will show the electrical characterisation performed on these devices through current-voltage measurements as a function of the temperature. The critical current dependence on the temperature for both type of superconducting junctions have also been analyzed and are in good agreement with theoretical predictions. The comparison between two type of architectures indicates that the fabrication protocol developed is robust and allows to achieve for the suspended-design junctions the same superconducting properties measured in non-suspended devices. This is an promising result circumvents most of material science compatibility problems, thus enabling the implementation of nanowire for all types of superconductors, including HTS. The properties of YBCO-InAs-YBCO junctions will be discussed in the next chapter.

6.1 Non-Suspended Al- InAs-NWs - Al junctions

In this section we will focus our attention on the Non-Suspended superconducting junctions composed of the InAs-nanowire barrier and

Titanium/Aluminium electrodes (see 4.2). Current-voltage characteristics as a function of the temperature will be shown for different lengths of the barrier.
The electrical characterization of these junctions have been performed in four probes configuration as reported in 5.3.
Figure 6.1 shows a set of typical current-voltage characteristics at different temperatures from one of the measured Non-Suspended Al - InAs-NW - Al junctions. This device (with barrier length L=140 nm) has a critical current amplitude (I_c) of $\sim 160nA$ (corresponding to a supercurrent density of $J_c \sim 3kA/cm^2$. For all the esteems of critical current density we assume an uniform current distribution along the nanowire.) at the temperature T=10mK. The junction normal-state resistance is $R_n \sim 180\Omega$ and the $I_c \times R_n$ product yields the value $\sim 30\mu$eV. Taking into account the geometric parameters of the device

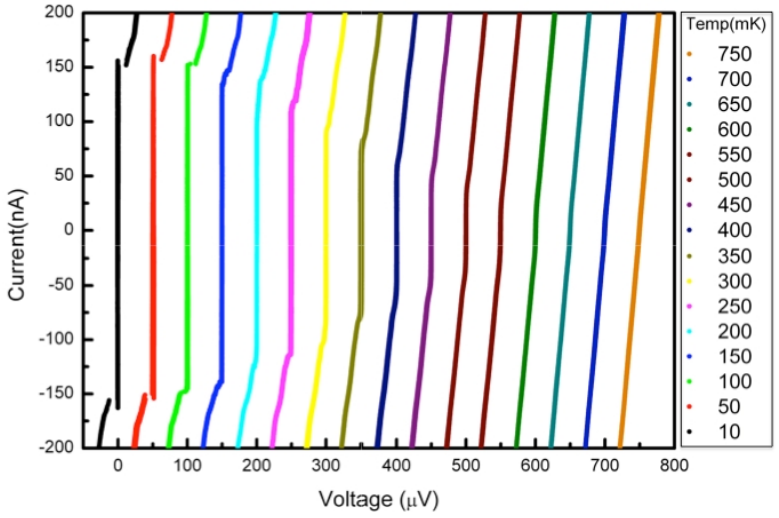

Figure 6.1: Current vs voltage characteristics for Non-Suspended Al - InAs-NW - Al junction with L=(140±5)nm (electrode spacing) measured at different temperatures. The curves have been horizontally shifted by $50\mu V$ for clarity. The critical current at the base temperature shows an amplitude I_c of 160nA and decreases when the increase of the temperature. At T=600mK the amplitude of I_c is included in noise of the measurement. We assume T=600mK as the critical temperature of the junctions.

and the normal transport properties of this type of InAs-NWs (3.2.2) we have estimated, at temperature T=300mK, a normal coherent length $\xi_n = \sqrt{(\hbar D/2\pi k_B T)} \sim 300nm$ and a Thouless energy $E_{Th} = \hbar D/L^2 \sim 4meV$ (E_{Th} represents an energy scale that has a strong rule in mesoscopic

physics and governs much of the physics of diffusive disordered systems and is connected to the inverse of the diffusion time of carriers through the system [137]). By comparing Δ with E_{Th} and length L with ξ_n we found that the dynamic of the superconducting system occurs in the short and diffusive junction limit ($\ell \ll \xi_n$ and $\Delta \ll E_{Th}$) [12]. Ic(T) is analyzed by using a model which holds for short diffusive superconductor-normal metal-superconductor (SNS) junction obtained by solving the linearized Usadel equation [12]. The best fit is yielded by L_{eff}=320nm and $R_b = 80\Omega$, where L_{eff} and R_b represent the effective length of the junction (it is much larger than the interelectrode spacing. This result is supported by observing the design of the junction (see fig6.1): the electrodes cover a considerable section of the NW. The same fit procedure and interpretation have been accomplished in [26]. Mathematica script and the result of fit procedure in Appendix G are shown.

Assuming an ideal situation (no backscattering of electrons in the con-

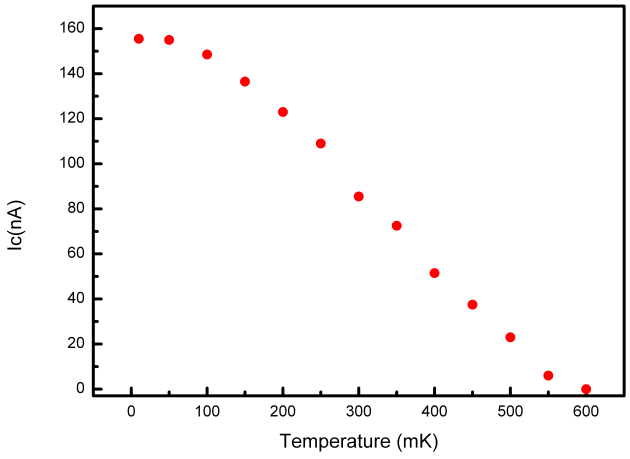

Figure 6.2: The critical currents as a function of the temperature for a devices of length L=140nm. I_c has been extracted using a $V = 1\mu V$ threshold and at the base temperature $I_c = 160nm$; this value corresponds a $J_c \sim 3kA/cm^2$ (the same order of magnitude found for this type of NWs [11]).

tacts), in the Buttiker-Landauer framework [47], there is the possibility of overestimation the transparency ($\mathbb{T}$) and the number of channels in the InAs-NWs. Let us define $R_{2w} = R_{4w} + R_b$, where R_{2w} and R_{4w} represent the resistance of the device measured by 2 wires and 4 wires configuration, respectively, and R_b is the barrier resistance estimated

by previously fit procedure. Taking in account the relations $R_{2w} = \frac{R_q}{NT}$ and $R_{4w} = R_q\frac{1-T}{NT}$ [47], where R_q, N and T represent quantum of resistance $R_q = h/2e^2 \sim 13K\Omega$, the numbers and the average transapernсy of the channels, respectively, we estimate, for the junction D (L=140nm, I_c(10mK)=160nA, R_n=180Ω)), a number of channels N$\sim$ 130 and an average transparency $\mathbb{T}$ ∼0.35. These results are in reasonable agreement with the values found through different data elaboration for junctions made with this type of InAs-NWs [11, 23, 26].
In Tab.6.1 the values of the critical current (at T=10mK) and the normal resistance for a set of superconducting junctions built on the same InAs-NWs (see fig.4.2) are summarized.

Dev	L (nm)	I_c(T=10mK)(nA)	R_n(Ω)
A	230	10	560
C	170	90	240
D	140	160	180
E	110	170	150

Table 6.1: Measurements properties for a Non-suspended junctions between Al - InAs-NW - Al fabricated on the same NWs. The data show a linear ratio between normal region length (L) and normal resistance (R_n). The InAs-NW have been clamped by Ti/Al-(12/120)nm. The error in L is $\sim 5nm$ and it depends on the accuracy of the software (Smart Tiff - SEM Raith GmbH toolbox) that allows us to evaluate the spatial size of the devices. We find that the error in the measurements of R_n is 1% (see 5.3).

6.2 Suspended Al - InAs-NWs - Al junctions

In this section we describe the electrical characterization of Suspended Al - InAs-NWs - Al junctions fabricated following the DEP protocol (see section 4.4.3). These devices have shown superconducting properties comparable to those typically observed in the more standard Non-Suspended architecture, thus confirming that the superconducting transport is not affect by the layout of the device (by the suspension of the nanowire).

These results open the way to the realization of superconducting devices between HTS - InAs-NWs - HTS (fabrication 4.3 and transport measurements 7) in which HTS, for reasons due to their growth, need to be placed below the semiconducting InAs-Nws.
The electrical characterization of Suspended Al- InAs-NWs have been accomplished from room temperature down to 300 mK using an filtered and magnetically shielded Heliox refrigerator (see section 5).

6.2.1 Resistance - Temperature

In figure 6.3 shows typical Resistance vs. Temperature ($R(T)$) curves are shown for suspended devices fabricated starting from nano-trenches of different sizes d (see fig.4.16-b) which substantially provide the having a channel length $L \approx d$. Since the room temperature normal resistance

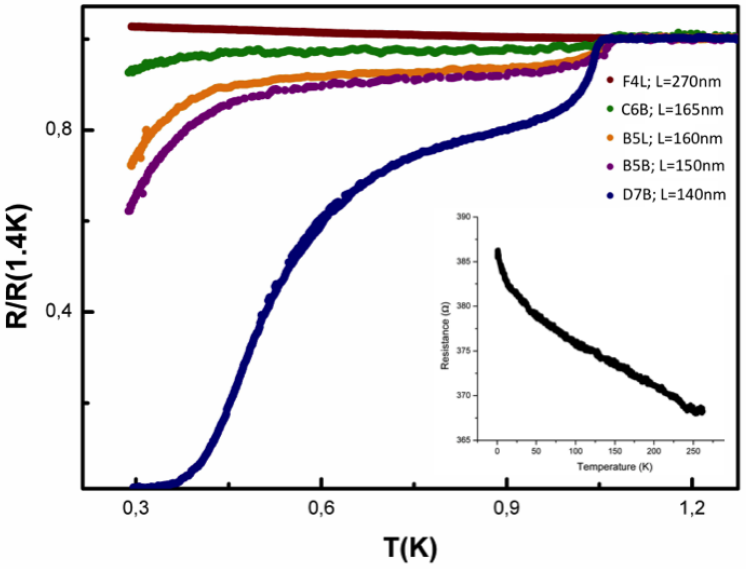

Figure 6.3: Normalized $R(T)/R(1.4\,\mathrm{K})$ curves of suspended devices characterized by a different channel length L: 270nm (device F4L), 165nm (C6B); 160nm (B5L), 150nm (B5B) and D7B (140nm). At the temperature of 1.1K a drop in resistance is shown and is a consequence superconducting transition of the of Ti/Al connection stripes. A different behaviour is observed as a function of L: devices with $L \lesssim 200\,\mathrm{nm}$ display a metallic behaviour; if $L \lesssim 150\,\mathrm{nm}$ the full transition to the superconductive regime is obtained. In the inset a typical R(T) curve (for the device B5B with L=150nm) that covers all the range of temperature is shown.

R_N of the devices ranges from 180Ω to the 400Ω (see Tab.7.1), the graph shows the resistances normalized to their values at $T = 1.4\,\mathrm{K}$ (for clarity

only the resistance - temperature curves of five junctions with different L have been plotted). From room temperature down to $T = 1.1\,\mathrm{K}$ the $R(T)$ curves show a similar insulating trend (the inset in fig.6.3 shows a typical R(T) for the device B5B with L=150nm from room to base temperature), independently of the extension L of the normal region. For all the devices, a drop in the resistance is observed at $T = 1.1\,\mathrm{K}$, as a consequence of the superconducting transition of the Ti/Al pads. Below this temperature, a different behaviour depending on the L parameter is shown. For the device F4L, 270nm long, the insulating behavior continue down to 300mK, indicating that the transport in the NW is not influenced by superconducting contacts. The devices with $150nm L \lesssim 200nm$ the resistance monotonically decrease reaching non zero value at the base temperature, indicating that a complete transition to the superconducting state needs lower temperature. For devices with L$\lesssim$150nm, a complete superconducting transition is typically observed. These results indicate a clear influence of the channel length L in the induction of a proximity effect across the contact barriers and into the NWs. In the Tab. 7.1 the values of resistance and length of suspended Al- InAs-NWs - Al junctions are summarized.

Dev	L (nm)	$R_n(\Omega)$
B5B	150	390
B5L	160	470
C6B	165	350
D7B	140	180
F4L	270	460
G4R	220	610
G5L	170	520
G5R	200	1600

Table 6.2: Measurements properties for suspended Al - InAs-NWs - Al junctions. The experimental errors in L and R_n are 5nm and 1%, respectively (see 6.1).

6.2.2 Current - Voltage

The current voltage ($I-V$) characteristics of the superconductive devices were carefully analized as a function of the temperature and selected curves are shown in fig.6.4 for device D7B. The behaviour of these devices is typical of that of an overdamped Josephson junction showing showing thermal rounding typical of RSJ model, enhanced by the low values of Ic which may favor phase diffusion effects [51, 119]. The critical current, extracted using a $V = 1\mu V$ threshold, is $I_c = 62\,\mathrm{nA}$ at $T = 300\,\mathrm{mK}$; this value corresponds to a critical current density of about $1.0 \times\ \mathrm{kA/cm^2}$, in agreement with values typically found for this type of InAs-NWs used for building junctions in non-suspend architectures [11] and higher than the best result s published for suspendend junctions between InAs and Alluminium [23].

These superconducting properties are comparable to those of our conventional devices fabricated directly on the Si/SiO_2 substrate (see section 6.1). This confirms that 1) the high quality of the device where InAs Nw is placed in suspension on two metallic banks and 2) the discussed DEP method (see section 4.4.3) provides a valid route for the realization of high quality hybrid devices on narrow-gap electrodes.

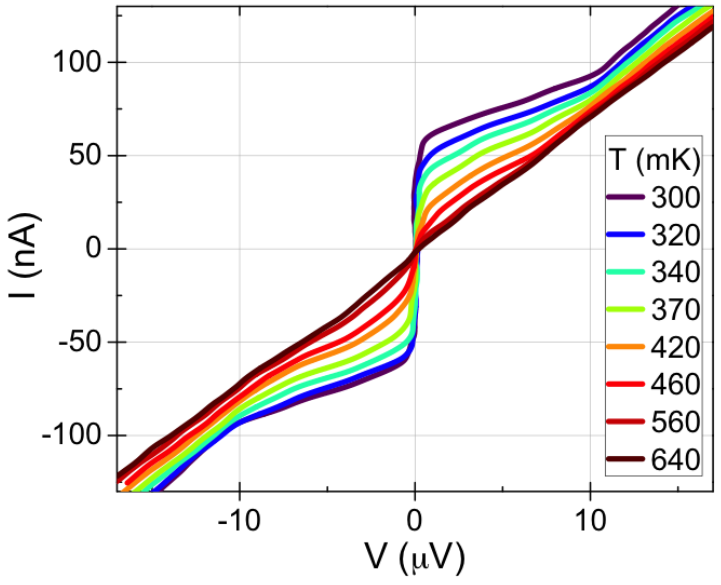

Figure 6.4: Current-Voltage characteristics for Suspended device of length L=140nm as a function of the temperature. The critical currents at the base temperature (300mK) $I_c = (62 \pm 3)nA$.

6.2.3 Critical current - temperature

Starting from the normal transport properties of the InAs NWs, L=140nm and $D = 0.02\,\mathrm{m}^2/\mathrm{s}$ (see 3.1), we estimate a Thouless energy $E_{Th} = \hbar D/L^2 \approx 700\mu eV$ and at T=300mK a normal coherence length $\xi_N = \sqrt{\hbar D/2\pi k_B T} = 300\,\mathrm{nm}$; these parameters indicate that the devices operate in the diffusive short-junction limit ($\ell \ll \xi_n$ and $\Delta \ll E_{Th}$) [12]. Further insight in the transport mechanisms of the suspended devices can be obtained from the temperature dependence of the superconducting critical current $I_c(T)$, which we show in fig.6.5. We compare the experimental I_c vs. T behaviour with a model which takes into account the barrier transparency. The upper concavity of the I_c vs T curve of fig.6.5 is indeed an indication of a sizeable superconducting (S)-normal (N) interface resistance, as shown in [138]. In this framework, the energy scale ruling the $I_c(T)$ dependence is an effective Thouless Energy E^*_{th} which takes into account the ratio between the resistances of the S/N interfaces and the one of the normal conductor [138]. Our experimental data indeed can be well approximated by an exponential function [139]:

$$I_c(T) \propto exp(-T/T^*) \tag{6.1}$$

where T^* is linked to the reduced Thouless energy by $E^*_{Th} = 2\pi k_B T^*/24$. The fit is shown as a full red line and was obtained with a value $E^*_{th} = 3.1\,\mu\mathrm{eV}$. The $I_cR_n \sim 10\mu eV$ product for the device D7B is significantly lower than the theoretical value of $\Delta\sim 120\mu eV$ for an ideal SNS junction. This reduction of I_cR_n happens in quite a variety of SNS junctions [65, 140] and between NWs and superconductors has been measured by several groups [11, 14, 141] and has been attributed to a finite transparency of the NWs-Superconductor interface. The behavior of I_c and the reduced value of the I_cR_n product is a clear indication that the superconducting trasport of this device occurs in the diffusive long-junction limit ($\ell \ll \xi_n$ and $E^*_{Th} < \Delta$). This change of the superconducting transport regime is ascribed to the interface effects that hamper the superconducting proximization of the InAs-NW.

A different esteem of $\mathbb{T}$ for the device D7B has been carry out by BTK framework (see chapter 2), through the excess current I_{exc} (that depends on $\mathbb{T}$ and L), extracted from the current voltage characteristic at

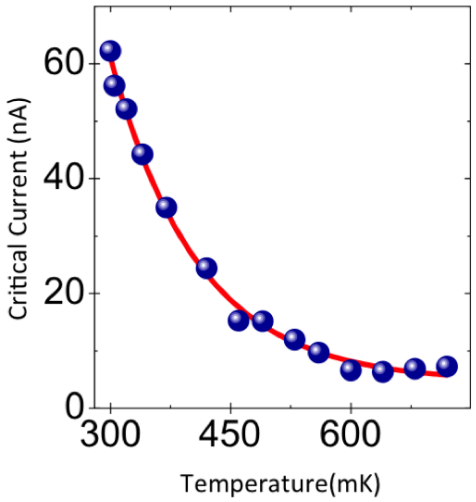

Figure 6.5: The critical currents as a function of the temperature for a devices of length L=140nm. The critical currents have been extracted using a $V = 1\mu V$ threshold and at the base temperature (300mK) I_c =62nA (the error in I_c is 3nA (see 5.3)). If we assume a uniform current distribution along the NWs it corresponds a density of critical current of $\sim 1KA/cm^2$ (in agreement with the value found for the same type of NW [11]).

large value of voltage by a linear fit (see Appendix F). At T=300mK we found an $I_{exc} = (69)$nA and $R_n = 180\Omega$ (the error in I_c and R_n are 1nA and $1\times10^{-5}\Omega$, respectively and have been evaluated by linear fit procedure). From the ration $eI_{exc}R_n/\Delta(T)$ we have found the corresponded $Z \sim 0.4$ (strongly related to the transparency), that suggests the metallic barrier limit [68].

6.2.4 Differential conductance - Voltage

Fig.6.6 shows the temperature evolution of the differential resistance dV/dI curves as a function of the voltage in the sub-gap region (the sup-gap corresponds to the states at energy lower then the energy-gap ($\Delta = 120\mu eV$ for Al) of the superconductor) for the device D7B. Most of the devices between Al - InAs-NWs - Al fabricated with different length have shown the same type of the conductance - voltage curves. In fig.6.6 symmetric conductance structures are observed at $V \approx 10$ and $25\,\mu$eV and their position is not influenced by the temperature, indicating that do not depend on the superconducting gap $\Delta(T)$, thus they cannot be ascribed as peaks due to Andreev bound states [141, 142]. The curves dI/dV as a function of T show that the amplitude of the

peaks decreases as the temperature is increased and is almost completely suppressed at T=720mK: this evolution indicates that these structures have some connection with superconductivity. Other works in the literature have reported the appearance of differential resistance peaks having similar temperature behaviour and have related them to the coupling of Josephson current to the acoustic degrees of freedom of the suspended NWs [143]. However, since similar peaks are also observed in non-suspended devices with different length L (see, for instance, the inset of fig.6.6 where a dI/dV vs T curve for a non-suspended Al - InAs-NW - Al junctions is shown), the acoustic resonance frequency depends on L should shift the peaks along voltage axis, thus this explanation is ruled out. Another possible explanation takes into account the possible presence of some kind of spatial inhomogeneous resistive state in the NW ??. In this scenario, the peaks would be related to the sequential appearance of normal domains in the NW as the current is increased. Connecting the peculiar shape of R(T) curve with amplitude peaks temperature-independent in dI/dV vs V characteristic for the device D7B, the presence of inhomogeneous resistive state in the NW region in proximity with Al contacts is also supported. As visible from the data of fig.6.3, the $R(T)$ curve of devices with L in the range (150-160)nm exhibit a large plateau which extends from the superconductive onset of the Al patches at $T = 1.1\,\mathrm{K}$, down to $T = 500\,\mathrm{mK}$ reasonably ascribable to the presence of impurities in the NWs.

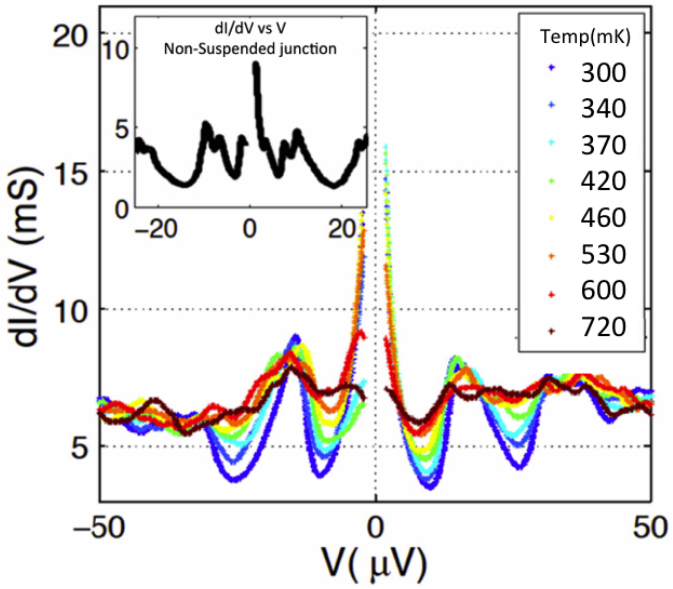

Figure 6.6: (Differential resistance dV/dI as a function of V for suspended device D7B(L=140nm and $R_n = 180\Omega$). The low voltage part of the data (where superconductivity is present) was cut for clarity. Only the sub-gap region is shown in order to highlight the presence of peaks with temperature independent voltage position. Similar peaks are visible also in the dV/dI curve of non-suspended device shown in the inset.

Chapter 7

Transport measurements YBCO - InAs-NWs - YBCO

The InAs-NWs have been already used as barriers with LTS, and mostly with Al contacts [14, 23, 24]. In hybrid systems between superconductors and semiconductors, interface effects and boundary conditions will eventually tune the superconducting proximity effect and the capability of transferring coherence from the electrodes to the barrier [3, 51, 65, 70, 144–146]. The induced coherence length in the semiconducting barrier depends on the carrier density as well and can significantly vary as reported in the literature [51, 147–158]. In the previous chapter, we have already shown that Josephson coupling in InAs-NWs/Al junctions which are shorther than 200 nm. Supercurrents have been occasionally mentioned for barrier lengths up to 500 nm [14] but without specifying critical currents and other junction parameters. In table 7.1 we summarize the main data set of different types of hybrid Sc-Nw-Sc junctions obtained by other groups. On the base of these results that have shown how supercurrent can flow through semiconducting nanowires, we believe that once the dimensions of the InAsNWs barrier and the interface resistance have been optimized, the high gap values of HTS should nominally guarantee, in quasi one-dimensional systems, higher values of the critical current when compared to LTS systems. This is due to the fact that I_c that flows in the junction is directly proportional to the gap value of the superconductor ($I_c = \frac{2e\Delta}{\hbar} \times f(T, \phi, R_n)$; where Δ is the gap of superconductor, $2e$ is the charge of the Cooper

Dev	$\rho_{@300K}$ (mΩ*cm)	L (nm)	eR_nI_c (meV)	I_c(nA) @Temp (mK)	∅ (nm)	n ($10^{18}(cm^{-3})$)	Reference
A	0.42		0.44	5700@800	120	100	[159]
B	1.8	30	0.10	800@15	80		[23]
C	3.7-9.0	20-50	0.10	350@350	90	18	[25]
D	0.9-2.2	100	0.27	615@10	50-80	3	[26]
B	[400-4000]*	100-450	0.002-0.06	135@40	40-130	2-10	[14]
B				3@30	50-300		[160]
B	0.82	140	0.011	62@300	90	18	[24]

Table 7.1: Here we collect as a reference some significant results on different types of Sc-NWs-Sc hybrid junctions which can be found in literature. The types of junctions are indicated as follows: A=Nb/InN(Nw)/Nb; B=Al/InAs(Nw)/Al; C=Vn/InAs(Nw)/Vn; D=Pb/InAs(Nw)/Pb. The physical parameters of the junctions are represented with symbols and letters as follows: ρ=resistivity of junction; L= length of the junction; ∅=average diameter of the NW; n=carrier density of the NW. The symbol * represents the values of the normal resistance (Ω) of the junctions.

pair and f is a function that depends on the temperature (T) of the system, on the phase difference (ϕ) of the order parameters of two superconducting banks and on the normal resistance R_n that includes all the microscopic parameters of the junction [51]).

In this chapter we will present and discuss the experimental results obtained by transport measurements in temperature of this novel type of hybrids nanojunctions made between semiconducting InAs-Nanowires and c-axis $YBa_2Cu_3O_{7-\delta}$. We will show and discuss the characteristics resistance as a function of the temperature that have been exhibited a strong dependence on the normal region length (L) of the devices. These results demonstrate that the current flows through the junctions, reflecting that a good transparence interfaces between the InAs-NWs and the High Temperature Superconducting Cooper pair reservoirs (HTS) have been achieved circumventing the huge problems due to the poor compatibility of HTS technology with both InAs-NWs material and semiconducting technology.

Our achievements in HTS - InAs-NWs - HTS junctions (a current flows across the NWs and the decrease of resistance for decreasing size L) combined with recent result [92] (a supercurrent induced by c-axis YBCO banks through a short gold weak link placed on two HTS reservoirs) lead us to believe that a shrinking of normal region length allows a

superconducting coupling through the semiconducting InAs-NWs, thus entailing the feasibility of the High-Superconducting field effect transistor (High-T_c-SUFET) [161].

7.1 Resistance vs Temperature measurements

Measurements of the resistance versus temperature R(T) have been performed on various YBCO/InAs-NW/YBCO junctions.Notwithstanding the fact that the bunch of NWs used have rather similar transport properties, the resistance of our devices can vary from chip to chip as it strongly depends on the transparency of the barriers.
In fig.7.3 a resistance-temperature curve of a typical junction between InAs-NWs and YBCO of length larger than 200nm is shown. At room temperature the resistance R_{300K} of the junction is $\sim 1200\Omega$ and with decreasing the temperature the amplitude of the resistance monotonically increases showing a typical semiconducting trend. At base temperature ($\sim 300mK$) the resistance $R_{300mK} \sim 1300\Omega$.

Taking in account that the InAs-NWs used for this type of junc-

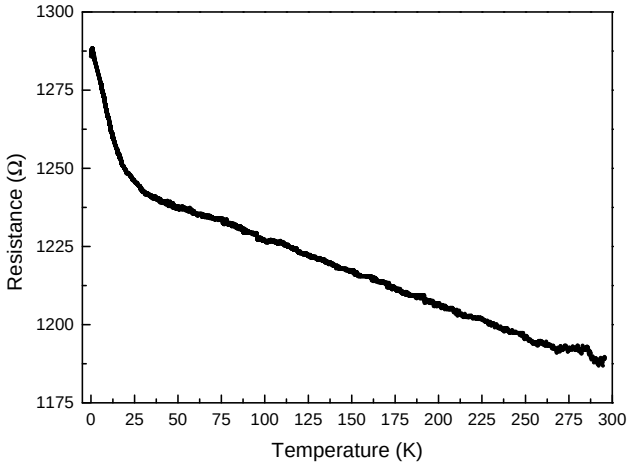

Figure 7.1: Typical resistance as a function of the temperature curve for the YBCO - InAs-NWs - YBCO junction with $L \sim 200nm$.

tions are strongly Selenium n-doped (see section 3.2), the characteristics R(T) have been analyzed in the framework of disordered media (see section1.3) and an activated behaviour of the conduction is expected in

this semiconducting regime.

The curves 7.1 in the temperature range $4.2K < T < 300K$ have been plotted on a log scale (it is customary plot for this type of data elaboration [162]) and fitted by the equation 7.1 (this relation comes from an easy manipulation of the eq.1.6);

$$\ln R(T) \sim \frac{T_a}{T} + cnst. \tag{7.1}$$

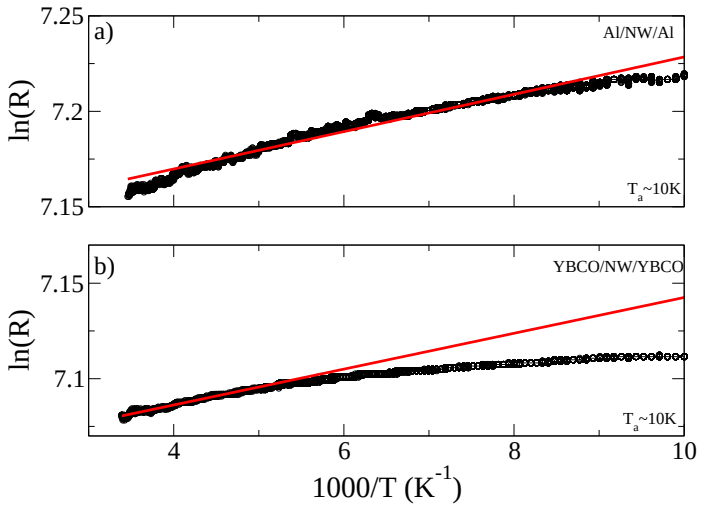

Figure 7.2: The figure shows the logR vs 1000/T fits by the eq.7.1 for junction between - (a) - InAs-NWs/LTS (∼200nm long) and - (b) - InAs-NWs/HTS (∼300nm long). The fitted activation temperature T_a is reported for two cases.

The figure 7.2 shows two R-T curves concerning: a) suspended junction between InAs-NW contacted with patches of Ti/Al is about 200 nm long; b) junction between InAs-NW is deposited on YBCO pads and clamped by a Ti/Au rectangle about 300nm long. Both types of hybrid devices have been built using the same thickness of Ti ($\sim 12nm$) interlayer (see section 4).

Here, we compare the R-T trend of the two semiconducting junctions. The InAs-NW/Al of figure a) is to stress that we find the same qualitative behavior in semiconducting InAs-NWs, of comparable length, deposited on Al and YBCO banks, respectively.

The working functions for the materials InAs-NWs, YBCO, Al, Ti and Au, used for building the junctions are approximate $\Phi_{InAs} \sim 4.9\ eV$, $\Phi_{YBCO} \sim 6.1eV$, $\Phi_{Al} \sim 4.4eV$, $\Phi_{Ti} \sim 4.33eV$ and $\Phi_{Au} \sim 5eV$, respectively

and if the condition $\Phi_{Sm} > \Phi_M$ (where Φ_{Sm} and Φ_M represent the working functions of semiconductor and the other materials, respectively) is satisfied then a Schottky barrier is avoid.
The fit of fig.7.2,a) gives an activation temperature $T_a \sim 10K$ for the InAs-NW/Al junction, which confirms the absence of a Schottky barrier. In the case of InAs-NW/Al, a reduced bending downward of the bands of InAs with negatively charged carriers trapped at the interface is expected, to match the chemical potentials at the junction.
For InAs-NW/YBCO junctions, it is difficult to give an estimate of the induced Schottky barrier height, in particular in view of the thin layers of Ti ($\sim 12nm$) and Au ($\sim 20nm$) that have been added at the interface to prevent oxygen diffusion or structural decomposition. A comparison of the work functions ($\Phi_{YBCO} > \Phi_{InAs}$) would suggest the formation of a strong Schottky barrier. Naively one would expect a strong bending upward of the bands in the InAs with a significant transfer of electrons into the metal. Charge transfer could be further assisted by the strong n-doping of the InAs-NWs. One would predict quite a sizeable T_a at high temperature, if the Schottky barrier were driving the conductance in InAs-NW/YBCO. Also, some nonlinearity in the I/V characteristic could be expected with a kind of offset diode voltage of fractions of eV. Surprisingly, the fit of the InAs-NW/YBCO samples, about 300 nm long, provide an activation temperature T_a comparable with the one of InAs-NW/Al (see fig.7.2,b). In various samples, for a InAs-NW length of $\sim$ 300 nm, T_a ranges from about 5 K to 20 K. However in this case the fit does not show a satisfactory agreement with the activated behavior in a large temperature regime (still satisfying the condition $T >> T_a$), as predicted by semiconductor theories, probably because of spurious interface effects. It could be argued that the Ti layer in the Ti/Au patch deposited on top of the InAs-NWNW could drive the electrostatics of the interface and make the Schottky barrier disappear. The Ti interlayer increases the transparency of the contact barrier and, at difference with InAs-NW/Al, the conduction in InAs-NW/YBCO samples has been found to be Ohmic in all samples at T>1 K, when the suspended length of the InAs-NW/YBCO is $\sim 200nm$. The R(T) decreases with decreasing temperature and the transport behavior appears to be metallic, except for very low temperatures. Since we have

estimated a mean free path $\ell \sim 20nm$ (see section 3.2.2), it implies that transport reasonably falls in the diffusion limit at high temperatures and a linear temperature dependence of the resistivity $\rho(T)$ is expected in this temperature range:

$$\rho(T) = \rho_0 \left[1 - \alpha(T - T_0)\right], \tag{7.2}$$

The fit of the data of fig.7.3 with $\rho_0 = \rho(T_0 = 100K) \sim 4.6 \cdot 10^{-6}\Omega$ has been accomplished and gives a slope $\alpha \sim 0.4 \cdot 10^{-3}K^{-1}$. From 25 K down to 2.5 K the resistance curve flattens, possibly due to impurity scattering. While the InAs-NW/YBCO that we fabricate with our procedure can become metallic if the intermediate region is short enough (we find $L < 200nm$ as critical length), the same does not seem to occur for InAs-NW/Al fabricated with equal procedure.
The conductivity that we can extract from the sample in fig.7.3, and from other similar samples, is $\sigma \sim 2 \cdot 10^5 \Omega^{-1}/m$ at room temperature. Hence, the conductance at scale ℓ is $g_0 \approx \sigma S/\ell \sim [100\Omega]^{-1}$ which is consistent with the limiting value in fig.7.3. g_0 characterizes the microscopic disorder and it is assumed as a threshold value in the scaling theory of localization. The samples like that of fig.7.3, may have $\ln g < \ln g_0$ and the system may scale to metallic behaviour for $L \gg \ell$. InAs-NW/YBCO junction of fig.7.1 displays resistances about one or two orders of magnitude higher and behave semiconducting. Similarly, InAs-NW/Al samples have a resistance that is sizeable larger than $100\Omega = g_0^{-1}$ and it is reasonable that they do not scale to metallic behaviour for $L \gg \ell$.

7.2 Comments on superconducting hybrids junctions between YBCO and InAs-NWs

To sum up, we have demonstrated the feasibility of the fabrication procedure of YBCO/suspended InAs-NW/YBCO junctions. The first achievement of our work is that junctions YBCO/Au- suspended InAs-NW-Au/YBCO of lengths $\sim$ 200 nm are not insulating allowing to the current flows through the InAs-NWs suspended channels. The other

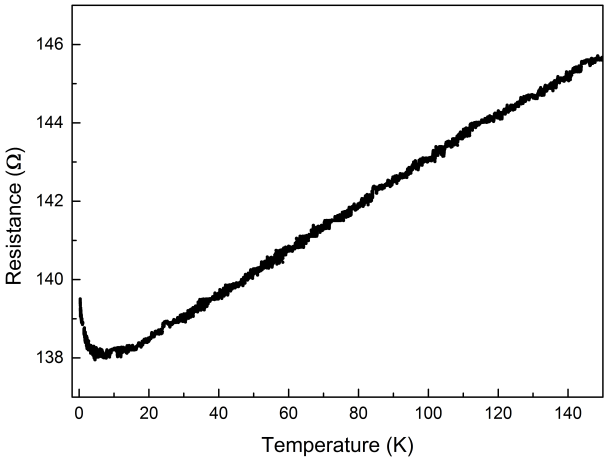

Figure 7.3: Characteristic resistance vs temperature for YBCO - InAs-NWs - YBCO junction with L∼200nm. A metallic behaviour from room temperature down to 25K is shown. From 25 down to 2.5K, the resistance does not show a dependence on the temperature; this behaviour is possibly due to the scattering by impurities. The resistance increases sharply between 2.5K and 0.3mK. This increase could be ascribed to incipient localization.

encouraging result is the decrease of resistance when the size of the suspended wire changes from 300 nm to 200 nm.

For L= 300 nm the resistance of the InAs-NWs interfaced with the Au/YBCO electrodes, is semiconducting-like (see fig.7.1). The resistance increases as a function of the temperature from room temperature to 300 mK, demonstrating the prevailing role of the InAs-NW and the substantially null effect of the superconducting banks. When reducing L down to 200 nm, the $R(T)$ dependence becomes metallic-like from room temperature to about 20 K (see fig.7.3). This behaviour is not exhibit by InAs-NW/Al devices, thus for InAs-NW-Au/YBCO junctions we ascribe the metalic-like trend of the R(T) to the YBCO electrodes. At lower temperatures there is a strong increase of the resistance both in the semiconducting and in the metallic samples possibly due to localization effects (for example, the correction of weak localization to the resistance are $\sim 1/ln(T)$ (see section 1.3.5), thus for decreasing temperature could yield and abruptly increase of resistance). In this range of temperature (from $\sim 2.5K$ to 300mK), the superconductivity seems to play no role in this length regime of the nanowire.

Our fabrication processes are the further demonstration of the progress

achieved in nanotechnology applied to HTS and in mastering more and more robust and high quality hetero-structures. This type of architecture not only may benefit of the high critical temperatures of the HTS electrodes but can be also extended to different barriers from semiconducting to ferromagnetic. This allows to experience new variety of functionalities and possibly NWs of different materials performing as tunable barriers. The achievements in the fabrication reported in the present work can be considered as very encouraging in the direction of the realization of Josephson hybrid HTS/InAs-NW/HTS junctions. The challenge is to realize high transparent barriers with superconductors tolerating high magnetic critical fields. Applications such as field effect transistors and nano-sensors may take advantage of these new possibilities offered by nanotechnology. Our YBCO/InAs-NW/YBCO junctions, being hybrid devices potentially controlled by low-dimensionality, spin-orbit coupling and superconducting proximity, could possibly host exotic Andreev bound states and Majorana states [34, 163–166].

Conclusion

In this work we have investigated the transport properties of superconducting hybrid systems made with semiconducting InAs-NWs - Aluminium and semiconducting InAs -NWs- YBCO. Mixing bottom-up and top-down nanofabrication approaches Josephson junctions in non-suspended and suspended design have been built. For devices with aluminium, the InAs-NWs have been positioned by random and assisted technique (the last is known as Dielectrophoresis technique).The native oxide shell of InAs-NWs that hampers the current flux trough the interface have been removed by a chemical procedure (passivation with NS_4H_x). This allowed a good transparency at the interface InAs-NWs/Al, thus the induced superconducting proximity has been displayed. Suspended and non-suspended junction between InAs-NWs - Aluminium have been systematically investigated by transport measurements up to 10mK. For InAs-NWs - Aluminium non suspended junctions a supercurrent has been observed for normal region 230nm long. Both type of devices shown that the critical current decrease with increase of the temperature; at the temperature of 600mK both the designs shown a transition to normal state. A comparison of the transport properties for suspended and non-suspended architectures show that the coupling between the substrate and the normal region of the junction does not affect the transport properties of these devices. The results of yielded junctions are in excellent agreement with the best data achieved by uncontested leaders in this research field (groups of University of Delft, Harvard, Lund, Grenoble,..). These results guaranties the high quality of works developed and pave the way toward the development and the integration of more advanced systems.

The nanotechnology platform developed for suspended LTS junctions

has represented the starting point for the integration between YBCO and the semiconducting InAs-NWS. Several efforts been accomplished and many design of the structures have been developed. A special design that allowed us to circumvent nanofabrication problems due to the complex structure of YBCO unit cell and its compatibility with InAs-NWs and semiconducting nanoprocessing has been found.

Innovative superconducting hybrid devices YBCO/NWS have been characterized with electric transport measurements as function of temperature and show as a current injected into YBCO banks can cross the NWs that works as a weak link. Current passes through the InAs-NWS, demonstrating the feasibility of the whole fabrication process. The other encouraging result is due to the resistance dependances on the normal length (L) of junction.

Resistance temperature (R-T) curves for device with L longer than 200nm systematically shown a semiconducting behaviour in all the range of temperature. Devices with $L < 200nm$ show, in the range of temperature 300K-20K, a R-T with a metallic like trend. This behaviour is not exhibited in Al/InAs-NWs devices, thus we believe that is ascribable to the YBCO. From 25K down to 2.5K the resistance does not shown a dependance on the temperature. This behaviour is possibly due to the scattering by impurities. At lower temperatures (from 2.5K down to base temperature) the resistance abruptly increase; behaviour possibly dues to the localization effects.

The achievements in the nanofabrication reported in the present work can be considered as very encouraging in the direction of the realization of the Josephson field effect transistor with HTS/InAs-NW/HTS.

Appendix A

3M Ammonium polysulfide $(NH_4)_2S_x$

1. **Commercial Sulphur 144 mg;**
2. **Ammonium Sulfate 1.5ml;**
3. **Mix 2h;**
4. **Dilution deionized water13.5ml;**
5. **Mix 2h;**
6. **The solution is ready and has a life time of 4 weeks. When yellow flakes appear on the liquid surface means that its reactivity changes.**
7. **Few $m\ell$ of solution are enough for cleaning NWs on a Si/SiO_2 substrate with few mm^2 of surface;**
8. **Bake the solution at $40\,^{\circ}\mathrm{C}$ for 3minutes;**
9. **Passivate from 35 to 45 seconds;**
10. **Rinse the sample in the deonized water for 15 seconds;**
11. **The NWs are ready for the metallization.**

Appendix B

Support chip device

1. **Clean a wafer of 2 inch Si/SiO_2 wafer capped by 280nm thick oxide with acetone;**
2. **Oxygen plasma: 10W for 5minutes;**
3. **Bake the sample at $150\,^{\circ}\mathrm{C}$ for 5 minutes;**
4. **Spin coat LOR 3A on the wafer using the settings with spin speed of 500rmp for 3 seconds and 3000rpm fro 35 seconds;**
5. **Bake at $170\,^{\circ}\mathrm{C}$ for 5 minutes;**
6. **Spin coat S1818 at 500 rpm for 3 seconds and 6000 rpm for 60 seconds;**
7. **Bake at $115\,^{\circ}\mathrm{C}$ for 1minute;**
8. **Exposure 10 seconds**
9. **Develop with $MF319$ for 60 seconds and rinse with DI water for 30 seconds;**
10. **Bake at $120\,^{\circ}\mathrm{C}$ for 5 minutes;**
11. **Oxygen ashing plasma 10W for 1minute;**
12. **Thermal evaporation Ti/Au (10nm/100nm);**
13. **Lift off hot acetone for 5 minutes and rinse in IPA for 30 seconds;**
14. **LOR remove MF319 for 30seconds and rinse in DI water for 30 seconds;**

Appendix C

Non-Suspended Hybrid Junctions

The support chip device (details are reported in Appendix B) are used for the fabrication of Non-Suspended Hybrid Junctions between InAs-NWs NWs and LTC.

1. **Clean the support chip device(Acetone/IPA);**
2. **Random deposition (wet or dry) of InAs-NWs;**
3. **SEM images for NWs localization;**
4. **Spin coat of PMMA type AR-P.679.04 at 6000rpm for 1minute;**
5. **Bake at 60 °C for 5 minutes;**
6. **EBL exposure;**
7. **Develop for stopper solution IPA for 30 seconds;**
8. **Oxygen ashing 10W for 1minute;**
9. **Passivation in Ammonium polysulfide (Details are reported in Appendix A);**
10. **Thermal evaporation of Ti/Au -(10nm/120nm);**
11. **Lift-off in acetone 15 minutes - IPA;**
12. **Fast SEM images session;**
13. **Store in vacuum the junctions;**
14. **The junction are ready for the electrical characterization.**

Appendix D

Suspended Hybrid Junctions between InAs-NWs and LTS

The support chip device (details are reported in Appendix B) are used for the fabrication of Suspended Hybrid Junctions between NWs and LTC.

1. **Clean the support chip device (Acetone/IPA);**
2. **Spin coat of PMMA type AR-P.679.04 at 6000 rpm for 1minute;**
3. **Bake at** $60\,^{\circ}\mathrm{C}$ **for 5 minutes;**
4. **EBL exposure;**
5. **Develop for 1 minute and rinse in IPA for 30seconds;**
6. **Oxygen ashing 10W, bias voltage 100V, for 1minute;**
7. **Thermal evaporation of Ti/Au - (10nm/100nm);**
8. **Lift-off hot acetone for 15 minutes;**
9. **SEM images;**
10. **The GAP are ready!!**
11. **NWs positioning with dielectrophoresis technique (Details are reported in 4.4.3);**
12. **SEM images for NWs localization;**
13. **Spin coat of PMMA type AR-P.679.04 at 6000 rpm for 1minute;**
14. **Bake at** $60\,^{\circ}\mathrm{C}$ **for 5 minutes;**
15. **EBL exposure;**

16. **Develop for 1 minute and rinse in IPA for 30 seconds;**
17. **Oxygen ashing 10W, bias voltage 100V, for 1minute;**
18. **Passivation in Ammonium polysulfide (Details are reported in Appendix A);**
19. **Thermal evaporation of Ti/Al - (10nm/120nm);**
20. **Lift-off in acetone 15 minutes and rinse in IPA for 30 seconds;**
21. **Fast SEM images session;**
22. **Store in vacuum the junctions;**
23. **Electrical characterization of the junctions.**

Appendix E

Suspended Hybrid Junctions between InAs-NWs and HTS

Recipe for fabricating superconducting InAs-NWs/YBCO junctions

1. **Blown with dry N_2 gas a new sample of YBCO capped by Au;**
2. **Spin coat PMMA AR-P679.04 at 6000runs/min for 60 seconds;**
3. **Bake PMMA at $160\,^{\circ}\mathrm{C}$ for 5minutes.**
4. **EBL exposure and development in AR-600-56 at room temperature for 60 seconds and rinse in IPA for 30 seconds;**
5. **Oxygen plasma ashing: 10W, 1minute, bias voltage 100V.**
6. **Spin coat PMMA AR-P679.04 at 6000runs/min for 60 seconds;**
7. **Ti Hard mask ~ 40nm thick thermal evaporation;**
8. **Lift-off ACE for 20minutes, 1minute of sonication plus siringature;**
9. **SEM images: check shorts and measure GAP width after the Ti hard mask;**
10. **Thickness measurements before ion milling etching (IBE);**
11. **Oxygen plasma cleaning before IBE step: 10W, 5 minutes, bias voltage 100V.**
12. **IBE at low temperature ($\sim -150\,^{\circ}\mathrm{C}$): bias voltage 315V and vacuum process performed at $1E-4$ Torr;**
13. **Thickness measurements after IBE and before HF etching;**
14. **Ti hard mask remover: HF at 49% diluted 1:20 in DI water; etch time 18 seconds and rinse in DI water for 2 seconds;**

15. **Thickness measurements of YBCO/AU.**

16. **Thickness measurements after IBE and HF etching;**

17. **SEM images: check shorts and measure GAP width;**

18. **Electrical check of the GAPs;**

19. **Oxygen plasma ashing: 10W, 1minute, bias voltage 100V.**

20. **InAs-NWs deposition (dry or wet) / positioning (by hands / by DEP);**

21. **SEM images: locate the NWs on the YBCO GAP respect marks;**

22. **Spin coat PMMA AR-P679.04 at 6000 runs/min per 60 seconds.**

23. **Bake at 60C per 5 minutes;**

24. **Evaporation of Ti thin layer (2-3 nm): fundamental to exposure the contacts on the InAs-NWs that does not drift during the exposure. This is due to the substrate charging;**

25. **EBL exposition: contacts on the InAs-NWs;**

26. **Ti remove: wet etching in HF 1:20 for 10 seconds and rinse in DI water for 2 seconds;**

27. **Development in AR-600-56 for 120 seconds and rinse in IPA for 30 seconds;**

28. **Oxygen plasma ashing at 10W, bias voltage 100V, 60 seconds;**

29. **InAs-NWs passivation in NH_4S_x (3M ammonium polysulfide solution diluted 1:8) for 35 seconds at $40\,^{\circ}\mathrm{C}$;**

30. **Ti/Al - (12nm/120nm) thermal evaporation;**

31. **Lift-off in acetone at room temperature for 20 minutes: weak sonication 1 second long. NO Siringature;**

32. **Fast SEM images at low EHT voltage (3KeV);**

33. **Store in vacuum the junctions;**

34. **Electrical transport measurements.**

Appendix F

Excess current

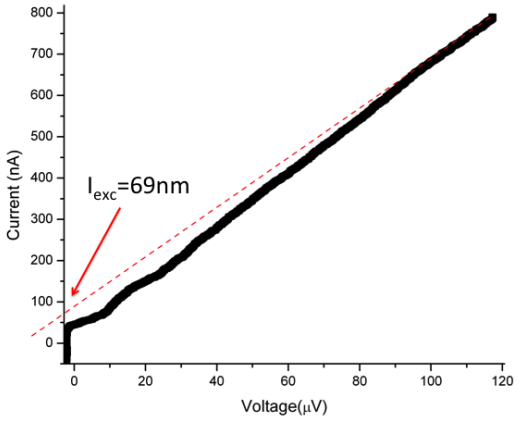

Figure F.1: Current voltage characteristic at T=300mK of D7B device with length L=140nm and normal resistance $R_n = 180\Omega$. The excess current $I_{exc} = (69 \pm 1)nA$ has been extrapolated by a fit linear of the normal region of I-V curve Blonder.

Since $eI_{exc}R_n/\Delta \sim 1.7$ **involves** $Z \sim 0.4$

Appendix G

Fit $I_C(T)$ short diffusive junction

Mathematica routine for $I_c - T$ data fit

$delta = Interpolation[Import["/Users/domenico/Desktop/Mathe/gapnew.dat","Table"]];$
$sdata = Table[delta];\ ListPlot[sdata];$

$q = 1.6021/10^{19};$
$hP = 1.05459/10^{34};$
$me = 9.1095/10^{31};\ kB = 1.3807/10^{23};$
$Rtunnel = 180;(*resistance@300K*);$
$Tc = 0.6;$(***superconductorcriticaltemperature*);**
d0 = 1.76 kB Tc(*BCSGAPatzerotemperature

$*);$

$gap[T_] := delta[T/Tc]d0;$

$L = 320/10^9;(*effective\ length\ of\ channels*)$
$kk = 2/10^2;(*$**diffusioncoeffm**$^2/s*)$

$(*Linearized\ Usadel\ Equation*)$

$A[Rb_,T_,n_] := 1 + (Rb/Rtunnel)^2 * L^2 * Abs[2 * PikBT(2n+1)]/(hP * kk);$
$B[Rb_,T_,n_] := 2Rb/RtunnelL * Sqrt[Abs[2 * PikB * T * (2n+1)]/(hP * kk)];$
$K[T_,n_] := Sqrt[Abs[2 * PikB * T * (2n+1)]/(hP * kk)];$
$Is[Rb_,T_] := Pi * kB/(q * Rtunnel) * T * Sum[((gap[T])^2 Sqrt[2 * Abs[Pi * kB * T *$
$(2*n+1)]/(hP*kk)] * L/(((Pi * kB * T * (2*n+1))^2 + (gap[T])^2) * (A[Rb,T,n] *$
$Sinh[K[T,n] * L] + B[Rb,T,n] * Cosh[K[T,n] * L]))), n, -100, 100];$
$(*test: Ic@10mK with R_b = 100)*)$
$Is[100, 0.01]$
$(*experimental\ data*)$
$data = \{...\};$

$(*experimental\ error*)$
$error = \{3\};$

$(*Plots*)\ nlm = NonlinearModelFit[data, Is[Rb,T], Rb, T, Weights -> 1/error^2]$
$nlm["ParameterTable"]$

$Show[ListPlot[data], Plot[nlm[x], x, 0, 1], AxesLabel- > T, Ic]$

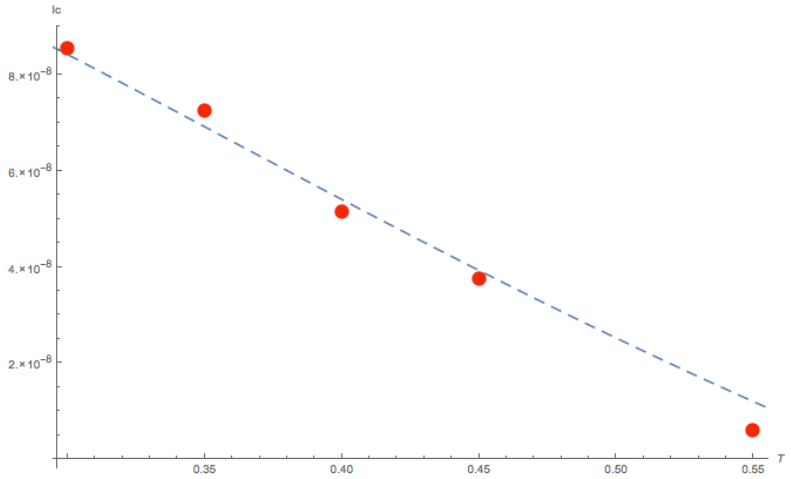

Figure G.1: I_c - T graph. The fit procedure has been accomplished by using a model which holds for short diffusive superconductor-normal metal-superconductor (SNS) junction [12]. The estimated parameter are $\mathrm{L}_{eff}(in the Mathematica script is called L) and \mathrm{R}_b$ the barrier resistance.

Bibliography

[1] Patrick A. Lee and T. V. Ramakrishnan. Disordered electronic systems. ***Rev. Mod. Phys.***, **57:287–337**, Apr 1985. URL http://link.aps.org/doi/10.1103/RevModPhys.57.287.

[2] E. Abrahams, P. W. Anderson, D. C. Licciardello, and T. V. Ramakrishnan. Scaling theory of localization: Absence of quantum diffusion in two dimensions. ***Phys. Rev. Lett.***, **42:673–676**, Mar 1979. URL http://link.aps.org/doi/10.1103/PhysRevLett.42.673.

[3] A. A. Golubov, M. Yu. Kupriyanov, and E. Il'ichev. The current-phase relation in josephson junctions. ***Rev. Mod. Phys.***, **76:411–469**, Apr 2004. URL http://link.aps.org/doi/10.1103/RevModPhys.76.411.

[4] Samanta Piano, Fabrizio Bobba, Filippo Giubileo, Anna Maria Cucolo, Marcello Gombos, and Antonio Vecchione. Pairing state in the ruthenocuprate superconductor $\mathrm{Rusr_2Gdcu_2o_8}$: A point-contact andreev reflection spectroscopy study. ***Phys. Rev. B***, **73:064514**, Feb 2006. URL http://link.aps.org/doi/10.1103/PhysRevB.73.064514.

[5] Jhi Seung-Hoon Lee Hu-Jong Lee Gil-Ho, Kim Sol. Ultimately short ballistic vertical graphene josephson junctions. ***Nat Commun***, **73:064514**, Jan 2015. URL http://dx.doi.org/10.1038/ncomms7181.

[6] LeBoeuf David-Levallois Julien Bonnemaison Jean Baptiste Liang Ruixing Bonn D. A. Hardy W. N. Taillefer Louis Doiron Leyraud Nicolas, Proust Cyril. Quantum oscillations and the fermi surface in an underdoped high-tc superconductor. ***Nature***, **447:064514**, Maj 2007. URL http://dx.doi.org/10.1038/nature05872.

[7] Ioffe Institute Division of Physics of Dielectric and Semiconductors. Inas - indium arsenide. URL http://www.ioffe.ru/SVA/NSM/Semicond/InAs/.

[8] E. Lind, M. P. Persson, Y. M. Niquet, and L. E. Wernersson. Band structure effects on the scaling properties of [111] inas nanowire mosfets. ***IEEE Transactions on Electron Devices***, **56(2):201–205**, Feb 2009.

[9] Shadi A Dayeh. Electron transport in indium arsenide nanowires. ***Semiconductor Science and Technology***, **25(2):024004**, 2010. URL http://stacks.iop.org/0268-1242/25/i=2/a=024004.

[10] **D. R. Khanalaand J. Wu. Gate coupling and charge distribution in nanowire field effect transistors. *Nano Letters*, 7(9):2778–2783, 2007. doi: 10.1021/nl071330l. URL** http://dx.doi.org/10.1021/nl071330l.

[11] **S. Roddaro, A. Pescaglini, D. Ercolani, L. Sorba, F. Giazotto, and Beltram F. Hot-electron effects in inas nanowier josephson junctions. *Nano Research*, 4:259, 2011. URL** http://link.springer.com/article/10.1007%2Fs12274-010-0077-6#page-1.

[12] **Tero T. Heikkilä, Jani Särkkä, and Frank K. Wilhelm. Supercurrent-carrying density of states in diffusive mesoscopic josephson weak links. *Phys. Rev. B*, 66:184513, Nov 2002. URL** http://link.aps.org/doi/10.1103/PhysRevB.66.184513.

[13] **P. W. Anderson. Absence of diffusion in certain random lattices. *Phys. Rev.*, 109:1492–1505, Mar 1958. URL** http://link.aps.org/doi/10.1103/PhysRev.109.1492.

[14] **Yong-Joo Doh, Jorden A. van Dam, Aarnoud L. Roest, Erik P. A. M. Bakkers, Leo P. Kouwenhoven, and Silvano De Franceschi. Tunable supercurrent through semiconductor nanowires. *Science*, 309(5732):272–275, 2005. URL** http://science.sciencemag.org/content/309/5732/272.

[15] **L. Hofstetter, S.a Csonka, J Nygard, and C. Schonenberger. Cooper pair splitter realized in a two-quantum-dot y-junction. *Nature*, 461, 2009. URL** http://www.nature.com/nature/journal/v461/n7266/suppinfo/nature08432_S1.html.

[16] **J-D. Pillet, C. H. L. Quay, P. Morfin, C. Bena, A. Levy Yeyati, and P. Joyez. Andreev bound states in supercurrent-carrying carbon nanotubes revealed. *Nature Publishing Group*, 6:965–969, 2010. URL** http://dx.doi.org/10.1038/nphys1811.

[17]

[18] **Francesco Giazotto, Panayotis Spathis, Stefano Roddaro, Subhajit Biswas, Fabio Taddei, Michele Governale, and Lucia Sorba. A josephson quantum electron pump. *Nat Phys*, 7:857–861, 2011. URL** http://dx.doi.org/10.1038/nphys2053.

[19] **Xiao-Liang Qi and Shou-Cheng Zhang. Topological insulators and superconductors. *Rev. Mod. Phys.*, 83:1057–1110, 2011. URL** http://link.aps.org/doi/10.1103/RevModPhys.83.1057.

[20] **A. I. Buzdin. Proximity effects in superconductor-ferromagnet heterostructures. *Rev. Mod. Phys.*, 77:935–976, 2005. URL** http://link.aps.org/doi/10.1103/RevModPhys.77.935.

[21] **Hubert B Heersche, Pablo Jarillo-Herrero, Jeroen B. Oostinga, Lieven M. K. Vandersypen, and Alberto F. Morpurgo. Bipolar supercurrent in graphene. *Nature*, pages 56–59, 2007. URL** http://dx.doi.org/10.1038/nature05555.

[22] **Naomi Mizuno, Bent Nielsen, and Xu Du. Ballistic-like supercurrent in suspended graphene josephson weak links. *Nat Commun*, 2013. URL** http://dx.doi.org/10.1038/ncomms3716.

[23] **Nilsson Henrik Wu Fan Xu H. Q. Fogelström Mikael Shumeiko Vitaly Abay Simon, Persson Daniel and Delsing Per. Charge transport in inas nanowire josephson junctions. *Phys. Rev. B*, 89:214508, Jun 2014. URL** http://link.aps.org/doi/10.1103/PhysRevB.89.214508.

[24] **D. Montemurro, D. Stornaiuolo, D. Massarotti, D. Ercolani, L. Sorba, F. Beltram, F. Tafuri, and S. Roddaro. Suspended inas nanowire josephson junctions assembled via dielectrophoresis. *Nanotechnology*, 26(38):385302, 2015. URL** http://stacks.iop.org/0957-4484/26/i=38/a=385302.

[25] **P Spathis, S Biswas, S Roddaro, L Sorba, F Giazotto, and F Beltram. Hybrid inas nanowire-vanadium proximity squid. *Nanotechnology*, 22(10):105201, 2011. URL** http://stacks.iop.org/0957-4484/22/i=10/a=105201.

[26] **J. Paajaste, M. Amado, S. Roddaro, F. S. Bergeret, D. Ercolani, L. Sorba, and F. Giazotto. Pb/inas nanowire josephson junction with high critical current and magnetic flux focusing. *Nano Letters*, 15(3):1803–1808, 2015. URL** http://dx.doi.org/10.1021/nl504544s.

[27] **Lincoln J. Lauhon, Mark S. Gudiksen, Deli Wang, and Charles M. Lieber. Epitaxial core-shell and core-multishell nanowire heterostructures. *Nature*, 420, 2002.**

[28] **D B Suyatin, C Thelander, M T Bjork, I Maximov, and L Samuelson. Sulfur passivation for ohmic contact formation to inas nanowires. *Nanotechnology*, 18(10):105307, 2007. URL** http://stacks.iop.org/0957-4484/18/i=10/a=105307.

[29] **V. N. Bessolov and M. V. Lebedev. Chalcogenide passivation of iii-v semiconductor surfaces. *Semiconductors*, 32(11):1141–1156. URL** http://dx.doi.org/10.1134/1.1187580.

[30] **David Appell. Nanotechnology: Wired for success. *Nature*, 419 (6907):553–555, 2002. URL** http://dx.doi.org/10.1038/419553a.

[31] **S. Csonka, L. Hofstetter, F. Freitag, S. Oberholzer, C. Schanenberger, T. S. Jespersen, M. Aagesen, and J. Nygayrd. Giant fluctuations and gate control of the g-factor in inas nanowire quantum dots. *Nano Letters*, 8(11):3932–3935, 2008. URL** http://dx.doi.org/10.1021/nl802418w.

[32] **Charles M. Lieber and Zhong Lin Wang. Functional nanowires. *MRS Bulletin*, 32:99–108, 2 2007. ISSN 1938-1425. URL** http://journals.cambridge.org/article_S0883769400007053.

[33] **V. Mourik, K. Zuo, S. M. Frolov, S. R. Plissard, E. P. A. M. Bakkers, and L. P. Kouwenhoven. Signatures of majorana fermions in hybrid superconductor-semiconductor nanowire devices. *Science*, 336(6084):1003–1007, 2012. doi: 10.1126/science.1222360. URL** http://www.sciencemag.org/content/336/6084/1003.abstract.

[34] **Roman M. Lutchyn, Jay D. Sau, and S. Das Sarma. Majorana fermions and a topological phase transition in semiconductor-superconductor heterostructures. *Phys. Rev. Lett.*, 105:077001, Aug 2010. URL** http://link.aps.org/doi/10.1103/PhysRevLett.105.077001.

[35] **Jason Alicea. Majorana fermions in a tunable semiconductor device. *Phys. Rev. B*, 81:125318, Mar 2010. URL** http://link.aps.org/doi/10.1103/PhysRevB.81.125318.

[36] **Liang Fu and C. L. Kane. Superconducting proximity effect and majorana fermions at the surface of a topological insulator. *Phys. Rev. Lett.*, 100:096407, Mar 2008. URL** http://link.aps.org/doi/10.1103/PhysRevLett.100.096407.

[37] **Jeffrey C. Y. Teo and C. L. Kane. Topological defects and gapless modes in insulators and superconductors. *Phys. Rev. B*, 82:115120, Sep 2010. doi: 10.1103/PhysRevB.82.115120. URL** http://link.aps.org/doi/10.1103/PhysRevB.82.115120.

[38] **Roman M. Lutchyn, Jay D. Sau, and S. Das Sarma. Majorana fermions and a topological phase transition in semiconductor-superconductor heterostructures. *Phys. Rev. Lett.*, 105:077001, Aug 2010. doi: 10.1103/PhysRevLett.105.077001. URL** http://link.aps.org/doi/10.1103/PhysRevLett.105.077001.

[39] **P. Lucignano, A. Mezzacapo, F. Tafuri, and A. Tagliacozzo. Advantages of using high-temperature cuprate superconductor heterostructures in the search for majorana fermions. *Phys. Rev. B*, 86:144513, 2012. URL** http://link.aps.org/doi/10.1103/PhysRevB.86.144513.

[40] **Elbio Dagotto. Complexity in strongly correlated electronic systems. *Science*, 309(5732):257–262, 2005. URL** http://science.sciencemag.org/content/309/5732/257.

[41] **Silvano De Franceschi, Leo Kouwenhoven, Christian Schonenberger, and Wolfgang Wernsdorfer. Hybrid superconductor-quantum dot devices. *Nat Nano*, (10):703–711, 2010. URL** http://dx.doi.org/10.1038/nnano.2010.173.

[42] **P. Krogstrup, N. L. B. Ziino, W. Chang, S. M. Albrecht, M. H. Madsen, E. Johnson, J. Nygrd, C. M. Marcus, and T. S. Jespersen. Epitaxy of semiconductor?superconductor nanowires. *Nat Mater*, 14(4):400–406, r2015. URL** http://dx.doi.org/10.1038/nmat4176.

[43] **Montemurro Domenico, Massarotti Davide, Lucignano Procolo, Roddaro Stefano, Stornaiuolo Daniela, Ercolani Daniele, Sorba Lucia, Tagliacozzo Arturo, Beltram Fabio, and Tafuri Francesco. Towards a hybrid high critical temperature superconductor junction with a semiconducting inas nanowire barrier. *Journal of Superconductivity and Novel Magnetism*, 28(12):3429–3437, 2015. URL** http://dx.doi.org/10.1007/s10948-015-3174-7.

[44] **N.W. Ashcroft and N.D. Mermin. Solid state physics. *Harcourt, Inc.*, 1976.**

[45] G. Grosso and G. Pastori Parravicini. Solid state physics. ***Accademin Press***, 2003.

[46] P. Yu and M. Cardona. Fundamentals of semiconductors. ***Springer***, 2005.

[47] S. Datta. Electronic transport in mesoscopic systems. ***Cambridge university press***, 1995.

[48] E. Akkermans and G. Montambaux. Mesoscopic physiscs of electrons and photons. ***Cambridge university press***, 2007.

[49] T. Heinzel. Mesoscopic electronics in solid state nanostructures. ***Wiley-VCH Verlag GmbH Co. KGaA***, 2007.

[50] S.M.GOODNICK D.K.Ferry and J.Bird. Transport in nanostructures. ***Cambridge university press***, 2009.

[51] A. Barone and G. Paterno. Physics and applications of the josephson effect. ***John Wiley***, 1982.

[52] Alexandra C. Ford, S. Bala Kumar, Rehan Kapadia, Jing Guo, and Ali Javey. Observation of degenerate one-dimensional subbands in cylindrical inas nanowires. ***Nano Letters***, 12(3):1340–1343, 2012. URL http://dx.doi.org/10.1021/nl203895x.

[53] N. F. Mott. Metal-insulator transition. ***Rev. Mod. Phys.***, 40:677–683, Oct 1968. URL http://link.aps.org/doi/10.1103/RevModPhys.40.677.

[54] I. S. Beloborodov, A. V. Lopatin, V. M. Vinokur, and K. B. Efetov. Granular electronic systems. ***Rev. Mod. Phys.***, 79:469–518, Apr 2007. URL http://link.aps.org/doi/10.1103/RevModPhys.79.469.

[55] M.Tinkham. Introduction to superconductivity. ***2nd edition, McGraw Hill, Inc.***, 1996.

[56] P.G. De Gennes. Superconductivity of metals and alloys. ***Westview Press***, 1999.

[57] H. Frohlich. Theory of the superconducting state. i. the ground state at the absolute zero of temperature. ***Phys. Rev.***, 79:845–856, Sep 1950. doi: 10.1103/PhysRev.79.845. URL http://link.aps.org/doi/10.1103/PhysRev.79.845.

[58] L.P. Gorkov. Microscopic derivation of the ginzburg-landau equations in the theory of superconductivity. ***Soviet Physics JETP***, 36 (6), 1959. URL http://www.jetp.ac.ru/cgi-bin/dn/e_009_06_1364.pdf.

[59] B.D. Josephson. Possible new effects in superconductive tunnelling. ***Physics Letters***, 1(7):251 – 253, 1962. ISSN 0031-9163. doi: http://dx.doi.org/10.1016/0031-9163(62)91369-0. URL http://www.sciencedirect.com/science/article/pii/0031916362913690.

[60] **P. W. Anderson and J. M. Rowell. Probable observation of the josephson superconducting tunneling effect. *Phys. Rev. Lett.*, 10: 230–232, Mar 1963. doi: 10.1103/PhysRevLett.10.230. URL** http://link.aps.org/doi/10.1103/PhysRevLett.10.230.

[61] **J. M. Rowell. Magnetic field dependence of the josephson tunnel current. *Phys. Rev. Lett.*, 11:200–202, Sep 1963. URL** http://link.aps.org/doi/10.1103/PhysRevLett.11.200.

[62] **Sidney Shapiro. Josephson currents in superconducting tunneling: The effect of microwaves and other observations. *Phys. Rev. Lett.*, 11:80–82, Jul 1963. URL** http://link.aps.org/doi/10.1103/PhysRevLett.11.80.

[63] **Ivar Giaever. Detection of the ac josephson effect. *Phys. Rev. Lett.*, 14:904–906, May 1965. URL** http://link.aps.org/doi/10.1103/PhysRevLett.14.904.

[64] **R.P. Feynman, R.B. Leighton, and M. Sands. The feynman lectures on physics. *Addison-Wesley Publishing Company, Inc*, III, Quantum Mechanics, 1965.**

[65] **K. K. Likharev. Superconducting weak links. *Rev. Mod. Phys.*, 51:101–159, 1979. URL** http://link.aps.org/doi/10.1103/RevModPhys.51.101.

[66] **Vinay Ambegaokar and Alexis Baratoff. Tunneling between superconductors. *Phys. Rev. Lett.*, 11:104–104, Jul 1963. URL** http://link.aps.org/doi/10.1103/PhysRevLett.11.104.

[67] **De Gennes P. G. Boundary effects in superconductors. *Rev. Mod. Phys.*, 36:225–237, Jan 1964. doi: 10.1103/RevModPhys.36.225. URL** http://link.aps.org/doi/10.1103/RevModPhys.36.225.

[68] **G. E. Blonder, M. Tinkham, and T. M. Klapwijk. Transition from metallic to tunneling regimes in superconducting microconstrictions: Excess current, charge imbalance, and supercurrent conversion. *Phys. Rev. B*, 25:4515–4532, Apr 1982. URL** http://link.aps.org/doi/10.1103/PhysRevB.25.4515.

[69] **A.F. Andreev. The thermal conductivity of the intermediate state in superconductors. *JETP*, 19(5):1228, 1965. URL** http://www.jetp.ac.ru/cgi-bin/dn/e_019_05_1228.pdf.

[70] **S. Kashiwaya and Y. Tanaka. Tunnelling effects on surface bound states in unconventional superconductors. *Rev. Prog. Phys.*, 63 (1641), 2000. URL** http://iopscience.iop.org/article/10.1088/0034-4885/63/10/202/pdf.

[71] **A.A.Golubov and F. Tafuri. Effects of anomalous andreev reflection in high tc layered structures. *IEEE Transactions on Applied Superconductivity*, 11(1):422–425, 2001. URL** http://ieeexplore.ieee.org/stamp/stamp.jsp?tp=&arnumber=919373.

[72] **Satoshi Kashiwaya, Yukio Tanaka, Masao Koyanagi, and Koji Kajimura. Theory for tunneling spectroscopy of anisotropic superconductors. *Phys.Rev.B*, 53:2667–2676, Feb 1996. URL** http://link.aps.org/doi/10.1103/PhysRevB.53.2667.

[73] **M. Octavio, M. Tinkham, G. E. Blonder, and T. M. Klapwijk. Subharmonic energy-gap structure in superconducting constrictions. *Phys. Rev. B*, 27:6739–6746, Jun 1983. URL** http://link.aps.org/doi/10.1103/PhysRevB.27.6739.

[74] **J. G. Bednorz and K. A. Müller. Possible hightc superconductivity in the balacuo system. *Zeitschrift für Physik B Condensed Matter*, 64(2):189–193. URL** http://dx.doi.org/10.1007/BF01303701.

[75] **Gilberd P. W. Presland M. R. Brown I. W. M. Bowden M. E. Christian L. A. Goguel R. Tallon J. L., Buckley R. G. High-tc superconducting phases in the series bi2.1(ca, sr)n+lcuno2n+4+[delta]. *Nature*, 333:153, Maj 1988. URL** http://dx.doi.org/10.1038/333153a0.

[76] **Z. Z. Sheng and A. M. Hermann. Bulk superconductivity at 120 k in the tlca/bacuo system. *Nature*, 332(6160):138–139, Mar 1988. URL** http://dx.doi.org/10.1038/332138a0.

[77] **A. Schilling, M. Cantoni, J. D. Guo, and H. R. Ott. Superconductivity above 130 k in the hg-ba-ca-cu-o system. *Nature*, 363(6424): 56–58, Maj 1993. URL** http://dx.doi.org/10.1038/363056a0.

[78] **Tsuei C. C. and J. R. Kirtley. Pairing symmetry in cuprate superconductors. *Rev. Mod. Phys.*, 72:969–1016, Oct 2000. URL** http://link.aps.org/doi/10.1103/RevModPhys.72.969.

[79] **J.R.Waldram. Superconductivity of metal and cuprates. 1996. URL** https://www.crcpress.com/Superconductivity-of-Metals-and-Cuprates/Waldram/9780852743379.

[80] **Dekkers J., Matthijn, Rijnders Guus, Harkema Sybolt, Smilde Henk Jan H., Hans Hilgenkamp, Rogalla Horst, and Blank Dave H. A. Monocrystalline $yba_2cu_3o_{7-x}$ thin films on vicinal srtio3 (001) substrates. *Applied Physics Letters*, 83(25):5199–5201, 2003. URL** http://scitation.aip.org/content/aip/journal/apl/83/25/10.1063/1.1633010.

[81] **A. Di Chiara, F. Lombardi, F.Miletto Granozio, U.Scotti di Uccio, M. Valentino, F. Tafuri, A. Del Vecchio, M.F. De Riccardis, and L. Tapfer.**

[82] **C H Wu, Y T Chou, W C Kuo, J H Chen, L M Wang, J C Chen, K L Chen, U C Sou, H C Yang, and J T Jeng. Fabrication and characterization of high-tc $yba_2cu_3o_{7-x}$ nanosquids made by focused ion beam milling. *Nanotechnology*, 19(31):315304, 2008. URL** http://stacks.iop.org/0957-4484/19/i=31/a=315304.

[83] **N Curtz, E Koller, H Zbinden, M Decroux, A Fischer L Antognazza, and N Gisin. Patterning of ultrathin ybco nanowires using a new focused-ion-beam process. *Superconductor Science and Technology*, 23(4):045015, 2010. URL** http://stacks.iop.org/0953-2048/23/i=4/a=045015.

[84] **A. I. Mansour, K. H. Chow, and J. Jung. Persistent critical current of $yba_2cu_3o_{7-\delta}$ nanowires. *Journal of Applied Physics*, 110(6):063909, 2011. URL** http://scitation.aip.org/content/aip/journal/jap/110/6/10.1063/1.3638713.

[85] **Morales P., M. DiCiano, and J. Y. T. Wei. Selective epitaxial growth of submicron complex oxide structures by amorphous srtio3. *Applied Physics Letters*, 86(19):192509, 2005. URL** http://scitation.aip.org/content/aip/journal/apl/86/19/10.1063/1.1925781.

[86] **Elkaseh A. A. O., Perold W. J., and V. V. Srinivasu. Josephson nanoconstrictions made by afm plowing of yba_2cu_3o7-x films. *Journal of Applied Physics*, 108(5):053914, 2010. URL** http://scitation.aip.org/content/aip/journal/jap/108/5/10.1063/1.3481425.

[87] **R. Arpaia, S. Nawaz, F. Lombardi, and T. Bauch. Improved nanopatterning for ybco nanowires approaching the depairing current. *IEEE Transactions on Applied Superconductivity*, 23(3):1101505–1101505, 2013. URL** http://ieeexplore.ieee.org/xpl/articleDetails.jsp?arnumber=6463434&action=search&sortType=&rowsPerPage=&searchField=Search_All&matchBoolean=true&queryText=((%22Authors%22:arpaia)%20AND%20%22Authors%22:lombardi).

[88] **G. Papari, F. Carillo, D. Born, L. Bartoloni, E. Gambale, D. Stornaiuolo, P. Pingue, F. Beltram, and F. Tafuri. Ybco nanobridges: Simplified fabrication process by using a ti hard mask. *IEEE Transactions on Applied Superconductivity*, 19(3):183–186, 2009. URL** http://ieeexplore.ieee.org/xpl/articleDetails.jsp?arnumber=5153053&action=search&sortType=&rowsPerPage=&searchField=Search_All&matchBoolean=true&queryText=((%22Authors%22:carillo)%20AND%20tafuri).

[89] **K. Kajino, T. Kimura andY. Horii, M. Watanabe, M. Inoue, and A. Fujimaki. Preparation of narrowed $yba_2cu_3o_{7-x}$ nanobridges down to 30 nm with reduced degradation. *IEEE Transactions on Applied Superconductivity*, 19(3):178–182, 2009.**

[90] **J Bonetti, A., D. S. Caplan, D. J. Van Harlingen, and M. B. Weissman. Electronic transport in underdoped $yba_2cu_3o_{7-\delta}$ nanowires: Evidence for fluctuating domain structures. *Phys. Rev. Lett.*, 93:087002, Aug 2004. URL** http://link.aps.org/doi/10.1103/PhysRevLett.93.087002.

[91] **J. Schneider, H. Kohlstedt, and R. Wordenweber. Nanobridges of optimized $yba_2cu_3o_7$ thin films for superconducting fluxflow type devices. *Applied Physics Letters*, 63(17):2426–2428, 1993. URL** http://scitation.aip.org/content/aip/journal/apl/63/17/10.1063/1.110496.

[92] **Baghdadi Reza, Arpaia Riccardo, Charpentier Sophie, Golubev Dmitri, Bauch Thilo, and Lombardi Floriana. Fabricating nanogaps in $yba_2cu_3o_{7-\delta}$ for hybrid proximity-based josephson junctions. *Phys. Rev. Applied*, 4:014022, Jul 2015. URL** http://link.aps.org/doi/10.1103/PhysRevApplied.4.014022.

[93] **C. C. Tsuei, J. R. Kirtley, C. C. Chi, Lock See Yu-Jahnes, A. Gupta, T. Shaw, J. Z. Sun, and M. B. Ketchen. Pairing symmetry and flux quantization in a tricrystal superconducting ring of $yba_2cu_3o_{7-x}$. *Phys. Rev. Lett.*, 73:593–596, 1994. URL** http://link.aps.org/doi/10.1103/PhysRevLett.73.593.

[94] **D. A. Wollman, D. J. Van Harlingen, W. C. Lee, D. M. Ginsberg, and A. J. Leggett. Experimental determination of the superconducting pairing state in ybco from the phase coherence of ybco-pb dc squids. *Phys. Rev. Lett.*, 71:2134–2137, Sep 1993. doi: 10.1103/PhysRevLett.71.2134. URL** http://link.aps.org/doi/10.1103/PhysRevLett.71.2134.

[95] **D. J. Van Harlingen. Phase-sensitive tests of the symmetry of the pairing state in the high-temperature superconductors - evidence for $d_{x^2-y^2}$ symmetry. *Rev. Mod. Phys.*, 67:515–535, Apr 1995. URL** http://link.aps.org/doi/10.1103/RevModPhys.67.515.

[96] **Tinkham Brad P. Boos J. Brad Lange Michael D. Bennett, Brian R. and Roger Tsai. Materials growth for inas high electron mobility transistors and circuits. *Journal of Vacuum Science Technology B*, 22(2):688–694, 2004. URL** http://scitation.aip.org/content/avs/journal/jvstb/22/2/10.1116/1.1667507.

[97] **J D Grange, E H C Parker, and R M King. Relationship of mbe growth parameters with the electrical properties of thin (100) inas epilayers. *Journal of Physics D: Applied Physics*, 12(9):1601, 1979. URL** http://stacks.iop.org/0022-3727/12/i=9/a=023.

[98] **D. C. Tsui. Observation of surface bound state and two-dimensional energy band by electron tunnelling. *Phys. Rev. Lett.*, 24:303–306, Feb 1970. URL** http://link.aps.org/doi/10.1103/PhysRevLett.24.303.

[99] **Cedric Affentauschegg and Harry H Wieder. Properties of inas/inalas heterostructures. *Semiconductor Science and Technology*, 16(8):708, 2001. URL** http://stacks.iop.org/0268-1242/16/i=8/a=313.

[100] **Ercolani D., Rossi F., Li A., Roddaro S., Grillo V., Salviati G., Beltram F., and Sorba L. Inas/insb nanowire heterostructures grown by chemical beam epitaxy. *Nanotechnology*, 20(505605), 2009. URL** http://iopscience.iop.org/article/10.1088/0957-4484/20/50/505605/meta;jsessionid=779DA951D38FA894F219A66C8E9BE8EE.c4.iopscience.cld.iop.org.

[101] **Vitiello M., Coquillat D., Viti L., Ercolani D., Teppe F., Pitanti A., Beltram F., Knap W. Sorba L., and Tredicucci A. Room-temperature terahertz detectors based on semiconductor nanowire field-effect transistors. *Nano Letters*, 12(96), 2012. URL** http://pubs.acs.org/doi/abs/10.1021/nl2030486.

[102] **Viti Leonardo, Vitiello Miriam, Ercolani Daniele, Sorba Lucia, and Tredicucci Alessandro. Se-doping dependence of the transport properties in cbe-grown inas nanowire field effect transistors. *Nanoscale Research Letters*, 7(1):159, 2012. URL** http://www.nanoscalereslett.com/content/7/1/159.

[103] **M J L Sourribes, I Isakov, M Panfilova, and P A Warburton. Minimization of the contact resistance between inas nanowires and metallic contacts. *Nanotechnology*, 24(4):045703, 2013. URL** http://stacks.iop.org/0957-4484/24/i=4/a=045703.

[104] **Ali Razavieh, Parsian Katal, Mohseni Kyooho Jung, Saumitra Mehrotra, Saptarshi Das, Sergey Suslov, Xiuling Li, Gerhard Klimeck, David B. Janes, and Joerg Appenzeller. Effect of diameter variation on electrical characteristics of schottky barrier indium arsenide nanowire field-effect transistors. *ACS Nano*, 8 (6):6281–6287, 2014. URL** http://dx.doi.org/10.1021/nn5017567.

[105] **I Shorubalko, A Pfund, R Leturcq, M T Borgstram, F Gramm, E Maeller, E Gini, and K Ensslin. Tunable few-electron quantum dots in inas nanowires. *Nanotechnology*, 18(4):044014, 2007. URL** http://stacks.iop.org/0957-4484/18/i=4/a=044014.

[106] **Alexandra C. Ford, S. Bala Kumar, Rehan Kapadia, Jing Guo, and Ali Javey. Observation of degenerate one-dimensional subbands in cylindrical inas nanowires. *Nano Letters*, 12(3):1340–1343, 2012. URL** http://dx.doi.org/10.1021/nl203895x.

[107] **Aagesen Martin Sørensen Claus Lindelof Poul Erik Jespersen, Thomas Sand and Jesper Nygård. Kondo physics in tunable semiconductor nanowire quantum dots. *Phys. Rev. B*, 74:233304, Dec 2006. URL** http://link.aps.org/doi/10.1103/PhysRevB.74.233304.

[108] **M J L Sourribes, I Isakov, M Panfilova, and P A Warburton. Minimization of the contact resistance between inas nanowires and metallic contacts. *Nanotechnology*, 24(4):045703, 2013. URL** http://stacks.iop.org/0957-4484/24/i=4/a=045703.

[109] **Scott A. Jewett and Albena Ivanisevic. Wet-chemical passivation of inas: Toward surfaces with high stability and low toxicity. *Accounts of Chemical Research*, 45(9):1451–1459, 2012. URL** http://dx.doi.org/10.1021/ar200282f.

[110] **Ho-Yuen Cheung, SenPo Yip, Ning Han, Goufa Dong, Ming Fang, Zai xing Yang, Fengyun Wang, Hao Lin, Chun-Yuen Wong, and Johnny C. Ho. Modulating electrical properties of inas nanowires via molecular monolayers. *ACS Nano*, 9(7):7545–7552, 2015. URL** http://dx.doi.org/10.1021/acsnano.5b02745.

[111] **Haibo Shu, Dan Cao, Pei Liang, Shangzhong Jin, Xiaoshuang Chen, and Wei Lu. Effect of molecular passivation on the doping of inas nanowires. *The Journal of Physical Chemistry C*, 116(33): 17928–17933, 2012. URL** http://dx.doi.org/10.1021/jp304350f.

[112] **W.Lu and C.M.Lieber. Semiconductor nanowires. *Journal of Physics D: Applied Physics*, 39(21):R387, 2006. URL** http://stacks.iop.org/0022-3727/39/i=21/a=R01.

[113] **M. D. Schroer and J. R. Petta. Correlating the nanostructure and electronic properties of inas nanowires. *Nano Letters*, 10(5): 1618–1622, 2010. URL** http://dx.doi.org/10.1021/nl904053j.

[114] **Simon M. Sze. Physics of semiconductor devices, 3rd edition. page 832, 2006. URL** http://eu.wiley.com/WileyCDA/WileyTitle/productCd-0471143235.html.

[115] **A.S.Sedra and K.C.Smith. Microelectronic circuits. page 1377, 2009. URL** http://global.oup.com/us/companion.websites/umbrella/sedrasmith/.

[116] **ChangW., AlbrechtS. M., JespersenT. S, KuemmethF., Krogstrup P., NygAYrd J., and Marcus C. M. Hard gap in epitaxial semiconductor superconductor nanowires. *Nat Nano*, 10: 232–236, 2015. URL** http://dx.doi.org/10.1038/nnano.2014.306.

[117] **G. Papari, F. Carillo, D. Stornaiuolo, D. Massarotti, L. Longobardi, F. Beltram, and F. Tafuri.**

[118] **D. Stornaiuolo, G. Rotoli, K. Cedergren, D. Born, T. Bauch, F. Lombardi, and F. Tafuri. Submicron ybacuo biepitaxial josephson junctions: d-wave effects and phase dynamics. *J. Appl. Phys.*, 107:113901, 2010. URL** http://scitation.aip.org/content/aip/journal/jap/107/11/10.1063/1.3388035.

[119] **Massarotti D. Carillo F. Longobardi L. Beltram F. Stornaiuolo D., Rotoli G. and F. Tafuri. Resolving the effects of frequency-dependent damping and quantum phase diffusion in ybco josephson junctions. *Phys. Rev. B*, 87:134517, Apr 2013. URL** http://link.aps.org/doi/10.1103/PhysRevB.87.134517.

[120] **P. Lucignano, D. Stornaiuolo, F. Tafuri, B. L. Altshuler, and A. Tagliacozzo. Evidence for a minigap in ybco grain boundary josephson junctions. *Phys. Rev. Lett.*, 105:147001, 2010. URL** http://link.aps.org/doi/10.1103/PhysRevLett.105.147001.

[121] **D. Gustafsson, H. Pettersson, B. Iandolo, E. Olsson, T. Bauch, and F. Lombardi. Soft nanostructuring of ybco josephson junctions by phase separation. *Nano Letters*, 10(12):4824–4829, 2010. URL** http://dx.doi.org/10.1021/nl103311a.

[122] **J Nagel, K B Konovalenko, M Kemmler, M Turad, R Werner, E Kleisz, S Menzel, R Klingeler, B Baechner, R Kleiner, and D Koelle. Resistively shunted $yba_2cu_3o_7$ grain boundary junctions and low-noise squids patterned by a focused ion beam down to 80anm linewidth. *Superconductor Science and Technology*, 24 (1):015015, 2011. URL** http://stacks.iop.org/0953-2048/24/i=1/a=015015.

[123] **R Arpaia, M Ejrnaes, L Parlato, R Cristiano, M Arzeo, T Bauch, S Nawaz andF Tafuri, G P Pepe, and F Lombardi. Highly homogeneous ybco/lsmo nanowires for photoresponse experiments. *Superconductor Science and Technology*, 27(4):044027, 2014. URL** http://stacks.iop.org/0953-2048/27/i=4/a=044027.

[124] **Sochnikov Ilya, Shaulov Avner, Yeshurun Yosef, Logvenov Gennady, and Bozovic van. Large oscillations of the magnetoresistance in nanopatterned high-temperature superconducting films. *Nat Nano*, 5(7):516, 2010. URL** http://dx.doi.org/10.1038/nnano.2010.111.

[125] **N.E. Litombe, A.T. Bollinger, J.E. Hoffman, and I. BoAYoviA. La2axsrxcuo4 superconductor nanowire devices. *Physica C: Superconductivity and its Applications*, 506:169 – 173, 2014. URL** http://www.sciencedirect.com/science/article/pii/S0921453414001890.

[126] **Nawaz S, Arpaia R, Lombardi F, and Bauch T. Microwave response of superconducting $yba_2cu_3o_{7-\delta}$ nanowire bridges sustaining the critical depairing current: Evidence of josephson-like**

behavior. ***Physical Review Letters***, 110(16), apr 2013. URL http://adsabs.harvard.edu/abs/2013PhRvL.110p7004N.

[127] P. Larsson, B. Nilsson, and Z. G. Ivanov. Fabrication and transport measurements of $yba_2cu_3o_{7-x}$ nanostructures. ***J. Vac. Sci. Techno***, 18(25), 2000. URL http://scitation.aip.org/content/avs/journal/jvstb/18/1/10.1116/1.591145.

[128] H. Assink, A. J. M. Harg, C. M. Schep, N. Y. Chen, D. Marel, P. Hadley, E. W. J. M. Drift, and J. E. Mooij. Critical currents in submicron $yba_2cu_3o_7$ lines. ***IEEE Transactions on Applied Superconductivity***, 3(1):2983–2985, 1993. URL http://ieeexplore.ieee.org/xpl/articleDetails.jsp?arnumber=234030.

[129] Ke Xu and James R. Heath. Long, highly-ordered high-temperature superconductor nanowire arrays. ***Nano Letters***, 8 (11):3845–3849, 2008. URL http://dx.doi.org/10.1021/nl802264x.

[130] Jiang H., Y. Huang, How H., Zhang S., Vittoria C.and Widom A.and Chrisey D. B.and Horwitz J. S., and Lee R. Observation of ultrahigh critical current densities in high-tc superconducting bridge constrictions. ***Phys. Rev. Lett.***, 66:1785–1788, Apr 1991. URL http://link.aps.org/doi/10.1103/PhysRevLett.66.1785.

[131] J. A. Bonetti, Caplan D. S.and Van Harlingen D. J., and Weissman M. B. Electronic transport in underdoped $yba_2cu_3o_{7-\delta}$ nanowires: Evidence for fluctuating domain structures. ***Phys. Rev. Lett.***, 93:087002, Aug 2004. URL http://link.aps.org/doi/10.1103/PhysRevLett.93.087002.

[132] P. Mohanty, J.Y.T. Wei, V. Ananth, P. Morales, and W. Skocpol. Nanoscale high-temperature superconductivity. ***Physica C: Superconductivity***, 408-410:666 – 669, 2004. URL http://www.sciencedirect.com/science/article/pii/S0921453404004277. Proceedings of the International Conference on Materials and Mechanisms of Superconductivity. High Temperature Superconductors $\{VII\}$– $\{M2SRIO\}$.

[133] Stav Zaitsev, Oleg Shtempluck, and Eyal Buks. Effects of electron beam induced carbon deposition on the mechanical properties of a micromechanical oscillator. ***Sensors and Actuators A: Physical***, 179:237 – 241, 2012. URL http://www.sciencedirect.com/science/article/pii/S0924424712001525.

[134] A.W. Maijenburg, M.G. Maas, E.J.B. Rodijk, W. Ahmed, E.S. Kooij, E.T. Carlen, D.H.A. Blank, and J.E. Elshof. Dielectrophoretic alignment of metal and metal oxide nanowires and nanotubes: A universal set of parameters for bridging prepatterned microelectrodes. ***Jour. of Colloid and Interface Science***, 355:486–493, 2011. URL http://www.sciencedirect.com/science/article/pii/S002197971001372X.

[135] Peter A. Smith, Christoper D. Nordquist, Thomas N. Jackson, Theresa S. Mayer, Benjamin R. Martin, Jeremiah Mbindyo, and Thomas E. Mallouk. Electric-field assisted assembly and alignment of metallic nanowires. ***Appl. Phys. Lett.***, 77:1399, 2000. URL http://scitation.aip.org/content/aip/journal/apl/77/9/10.1063/1.1290272.

[136] **P.J. Hesketh, M.A. Gallivan, S. Kumar, C.J. Erdy, and Wang Z.L. The application of dielectrophoresis to nanowire sorting and assmbly for sensors. *Proceeding of the 13th Mediterrranean Conference on Control and Automation*, pages 153–158, 2005. URL** http://ieeexplore.ieee.org/xpl/login.jsp?tp=&arnumber=1467007&url=http%3A%2F%2Fieeexplore.ieee.org%2Fiel5%2F9900%2F31471%2F01467007.pdf%3Farnumber%3D1467007.

[137] **J T Edwards and D J Thouless. Numerical studies of localization in disordered systems. *Journal of Physics C: Solid State Physics*, 5(8):807, 1972. URL** http://stacks.iop.org/0022-3719/5/i=8/a=007.

[138] **J. C. Hammer, J. C. Cuevas, F. S. Bergeret, and W. Belzig. Density of states and supercurrent in diffusive sns junctions: Roles of nonideal interfaces and spin-flip scattering. *Phys. Rev. B*, 76:064514, Aug 2007. URL** http://link.aps.org/doi/10.1103/PhysRevB.76.064514.

[139] **Franco Carillo, Detlef Born, Vittorio Pellegrini, Francesco Tafuri, Giorgio Biasiol, Lucia Sorba, and Fabio Beltram. Relevant energy scale in hybrid mesoscopic josephson junctions. *Phys. Rev. B*, 78:052506, 2008. URL** http://link.aps.org/doi/10.1103/PhysRevB.78.052506.

[140] **Francesco Tafuri and John R Kirtley. Weak links in high critical temperature superconductors. *Reports on Progress in Physics*, 68(11):2573, 2005. URL** http://stacks.iop.org/0034-4885/68/i=11/a=R03.

[141] **H. A. Nilsson, P. Samuelsson, P. Caroff, and H. Q. Xu. Supercurrent and multiple andreev reflections in an insb nanowire josephson junction. *Nano Letters*, 12(1):228–233, 2012.**

[142] **Jie Xiang, A. Vidan, M. Tinkham, R. M. Westervelt, and Charles M. Lieber. Ge/si nanowire mesoscopic josephson junctions. *Nature nanotech*, pages 208–213, 2006. URL** http://www.nature.com/nnano/journal/v1/n3/suppinfo/nnano.2006.140_S1.html.

[143] **Andrey Kretinin, Anindya Das, and Hadas Shtrikman. The self-actuating inas nanowire-based nanoelectromechanical josephson junction. *arXiv:1303.1410*, 2013. URL** http://arxiv.org/format/1303.1410.

[144] **F. S. Bergeret and J. C. Cuevas. The vortex state and josephson critical current ofadiffusive sns junction. *Journal of Low Temperature Physics*, 153(5):304–324, 2008. URL** http://dx.doi.org/10.1007/s10909-008-9826-2.

[145] **M.Yu. Kupriyanov, A. Brinkman, A.A. Golubov, M. Siegel, and H. Rogalla. Double-barrier josephson structures as the novel elements for superconducting large-scale integrated circuits. *Physica C: Superconductivity*, 326327:16 – 45, 1999. ISSN 0921-4534. URL** http://www.sciencedirect.com/science/article/pii/S0921453499004086.

[146] **Kresin Vladimir Z. Josephson current in low-dimensional proximity systems and the field effect. *Phys. Rev. B*, 34:7587–7595, 1986. URL** http://link.aps.org/doi/10.1103/PhysRevB.34.7587.

[147] **Toshikazu Nishino, Mutsuko Hatano, and Ushio Kawabe. Electron tunneling study of superconducting proximity effect in silicon backed with pb alloy. *Japanese Journal of Applied Physics*, 26 (S3-2):1543, 1987. URL** http://iopscience.iop.org/1347-4065/26/S3-2/1543.

[148] **Mutsuko Hatano, Toshikazu Nishino, and Ushio Kawabe. Experiments of the superconducting proximity effect between superconductor and semiconductor. *Appl Phys lett*, 50(52), 1987. URL** http://scitation.aip.org/content/aip/journal/apl/50/1/10.1063/1.98129.

[149] **Hideaki Takayanagi, Tatsushi Akazaki, and Junsaku Nitta. Observation of maximum supercurrent quantization in a superconducting quantum point contact. *Phys. Rev. Lett.*, 75:3533–3536, Nov 1995. URL** http://link.aps.org/doi/10.1103/PhysRevLett.75.3533.

[150] **Hideaki Takayanagi, Jørn Bindslev Hansen, and Junsaku Nitta. Mesoscopic fluctuations of the critical current in a superconductor¯normal-conductor¯superconductor. *Phys. Rev. Lett.*, 74:166–169, 1995. URL** http://link.aps.org/doi/10.1103/PhysRevLett.74.166.

[151] **T.M. Klapwijk.**

[152] **J. P. Heida, B. J. van Wees, T. M. Klapwijk, and G. Borghs. Nonlocal supercurrent in mesoscopic josephson junctions. *Phys. Rev. B*, 57:R5618–R5621, Mar 1998. URL** http://link.aps.org/doi/10.1103/PhysRevB.57.R5618.

[153] **A. W. Kleinsasser and A. Kastalsky. Excess voltage and resistance in superconductor-semiconductor junctions. *Phys. Rev. B*, 47:8361–8364, Apr 1993. URL** http://link.aps.org/doi/10.1103/PhysRevB.47.8361.

[154] **A. Kastalsky, A. W. Kleinsasser, L. H. Greene, R. Bhat, F. P. Milliken, and J. P. Harbison. Observation of pair currents in superconductor-semiconductor contacts. *Phys. Rev. Lett.*, 67: 3026–3029, Nov 1991. URL** http://link.aps.org/doi/10.1103/PhysRevLett.67.3026.

[155] **A. W. Kleinsasser and T. N. Jackson. Critical currents of superconducting metal-oxide-semiconductor field-effect transistors. *Phys. Rev. B*, 42:8716–8719, Nov 1990. URL** http://link.aps.org/doi/10.1103/PhysRevB.42.8716.

[156] **A. W. Kleinsasser andT. N. Jackson, D. McInturff, F. Rammo, G. D. Pettit, and J. M. Woodall. Critical currents of superconducting metal-oxide-semiconductor field-effect transistors. *Appl phys lett*, 55, 1989. URL** http://scitation.aip.org/content/aip/journal/apl/55/18/10.1063/1.102166.

[157] **A. F. Morpurgo, B. J. van Wees, T. M. Klapwijk, and G. Borghs. Energy spectroscopy of andreev levels between two superconductors. *Phys. Rev. Lett.*, 79:4010–4013, 1997. URL** http://link.aps.org/doi/10.1103/PhysRevLett.79.4010.

[158] **B. J. van Wees, P. de Vries, P. Magnée, and T. M. Klapwijk. Excess conductance of superconductor-semiconductor interfaces due to phase conjugation between electrons and holes. *Phys. Rev. Lett.*, 69:510–513, Jul 1992. URL** http://link.aps.org/doi/10.1103/PhysRevLett.69.510.

[159] **Xiaocheng Jiang, Qihua Xiong, Sungwoo Nam, Fang Qian, Yat Li, and Charles M. Lieber. Inas/inp radial nanowire heterostructures as high electron mobility devices. *Nano Letters*, 7(10):3214–3218, 2007. URL** http://dx.doi.org/10.1021/nl072024a.

[160] **Takahiro Nishio, Tatsuya Kozakai, Shinichi Amaha, Marcus Larsson, Henrik A Nilsson, H Q Xu, Guoqiang Zhang, Kouta Tateno, Hideaki Takayanagi, and Koji Ishibashi. Supercurrent through inas nanowires with highly transparent superconducting contacts. *Nanotechnology*, 22(44):445701, 2011. URL** http://stacks.iop.org/0957-4484/22/i=44/a=445701.

[161] **J Mannhart. High-tc transistors. *Superconductor Science and Technology*, 9(2):49, 1996. URL** http://stacks.iop.org/0953-2048/9/i=2/a=001.

[162] **Effects of crystal phase mixing on the electrical properties of inas nanowires (article) author=Claes Thelander and Philippe Caroff and Sbastien Plissard and Anil W. Dey and Kimberly A. Dick, journal=Nano Letters, year=2011, volume=11, number=6, pages=2424-2429, url=http://dx.doi.org/10.1021/nl2008339.**

[163] **Liang Fu and C. L. Kane. Josephson current and noise at a superconductor/quantum-spin-hall-insulator/superconductor junction. *Phys. Rev. B*, 79:161408, Apr 2009. URL** http://link.aps.org/doi/10.1103/PhysRevB.79.161408.

[164] **Yukio Tanaka, Takehito Yokoyama, and Naoto Nagaosa. Manipulation of the majorana fermion, andreev reflection, and josephson current on topological insulators. *Phys. Rev. Lett.*, 103:107002, Sep 2009. URL** http://link.aps.org/doi/10.1103/PhysRevLett.103.107002.

[165] **A. R. Akhmerov, Johan Nilsson, and C. W. J. Beenakker. Electrically detected interferometry of majorana fermions in a topological insulator. *Phys. Rev. Lett.*, 102:216404, May 2009. URL** http://link.aps.org/doi/10.1103/PhysRevLett.102.216404.

[166] **Pablo San-Jose, Elsa Prada, and Ramón Aguado. ac josephson effect in finite-length nanowire junctions with majorana modes. *Phys. Rev. Lett.*, 108:257001, Jun 2012. URL** http://link.aps.org/doi/10.1103/PhysRevLett.108.257001.